



Bio / Medical

• **Technical Review**

Aryloxazole Derivatives as Antimitotic and Vascular Disrupting Agents for Cancer Therapy

Materials / Systems

• **Technical Review**

State-of-the-Art Technology for Improving the Performance and Stability of High Performance Computers

Energy / Environment

• **Technical Review**

Solution-Processed High Band-Gap CuInGaS_2 Thin Film for Solar Cell Applications

Contents

Foreword	03
-----------------------	----

Bio / Medical

Technical Review

Aryloxazole Derivatives as Antimitotic and Vascular Disrupting Agents for Cancer Therapy	04
--	----

Feature Articles

Development of Conjugated Polymer Nanoparticles to Achieve Bright Near-Infrared Fluorescence and On/Off Photoswitching for Contrast-Enhanced Biomedical Imaging	14
Hydroxycinnamic Acids in <i>Crepidiastrum denticulatum</i> Protect Against Oxidative Stress-Induced Retinal Damage	19

Materials / Systems

Technical Review

State-of-the-Art Technology for Improving the Performance and Stability of High Performance Computers	29
---	----

Feature Articles

Non-volatile Control of 2DEG Conductivity at Oxide Interfaces	42
Bright Multicolor Tunable Lanthanide Ion-Doped Inorganic Nanophosphors Less Than 10 nm in Size	48
Using Nanoionics in Artificial Neuron Devices	57

Energy / Environment

Technical Review

Solution-Processed High Band-Gap CuInGaS ₂ Thin Film for Solar Cell Applications	62
---	----

Feature Articles

A Bioaerosol Detection Chip Using Inertial Impaction and Mini-fluorescent Microscopy	69
Removal of Metal from Acid Mine Drainage Using a Hybrid System with a Pipe-Inserted Microalgae Reactor	75
Novel Design of a Molybdenum Back Contact for High-Efficiency CIGS Solar Cells: Decoupling its Surface from the Bulk	80

Research Highlights

Recent Publications	90
New Patents	94

KIST News	98
------------------------	----

A Sign of the Times	102
----------------------------------	-----

Interview	104
------------------------	-----

Foreword



With great pleasure, anticipation, and gratitude to the support of my many fine colleagues, I am deeply honored to have recently been appointed the 23rd president of KIST. A large part of my job will be to build on the proven strengths of our organization in ways that support Korea's new administration in its efforts to usher in a new area of economic development for the nation. It is a challenging prospect, but we are in an excellent position to contribute a great deal to these efforts.

We are in the process of realigning our mission and objectives to aggressively pursue avenues of research deemed most important in this new economy. Along with brain science and the development of next-generation semiconductors, we are expanding the scope of our research to include advanced original technologies for ensuring adequate future resources for the nation and meeting the needs of our rapidly aging population.

It is imperative that small and medium enterprises flourish in a creative economy. For that reason, we are allocating more of our budget to research that will benefit SMEs and will form a task force to assist these enterprises through technology transfer. KIST will work to stimulate their business activities and strengthen their competitive edge.

Another critical aspect of KIST's activities will be to expand research in areas that will help resolve social issues. In fact, just last year, KIST provided tangible outcomes on an early detection diagnostic method for Alzheimer's disease and a method to prevent algal blooms.

An ongoing strategy that continues to be at the top of our list of priorities is to enhance KIST's position as a global leader in science and technology research. We are continuing to build an extended research network with various renowned research institutes around the world. At the same time, we are working with developing countries to expand their own science and technology capabilities by supporting the establishment of research institutes modeled after KIST and offering educational and other opportunities for developing S&T infrastructure.

It is only two years until KIST celebrates its 50th anniversary. We have been on a remarkable journey during that time and I look forward to participating in the ongoing story.

Dr. Byung Gwon Lee
President of KIST

[**Technical Review**]

Aryloxazole Derivatives as Antimitotic and Vascular Disrupting Agents for Cancer Therapy



Min Jeong Choi
Kainos Medicine



Ghil Soo Nam
Center for Neuro-
Medicine
gsnam@kist.re.kr



Ae Nim Pae
Center for Neuro-
Medicine
anpae@kist.re.kr

Mitosis is a series of mechanical events that generate two new nuclei containing identical copies of DNA during cell division. Due to the crucial role of the mitotic spindle in mitosis, the spindle fiber has been a valuable drug target in cancer therapy for decades [1]. The discovery of natural products that interact with the spindle fibers during mitosis in malignant cell growth, such as taxol and *vinca* alkaloids, has led scientists to explore diverse sets of natural compounds and synthetic small molecules as anti-cancer drugs. These mitotic spindle poisons halt cell cycle progression by two distinct mechanisms. One is by preventing tubulins from polymerizing into microtubules, thereby inhibiting cellular division. For example, *vinca* alkaloids and colchicine are known to bind to β -tubulins and block the formation of functional microtubules. The other mechanism uses taxol and its derivatives to bind to microtubules and disrupt their functions, thus halting cells in the mitotic state [2]. By the early 1990s, hundreds of effective mitosis inhibitors had been developed; unfortunately, the majority of spindle poisons failed in clinical trials due to their poor therapeutic index. Many compounds demonstrated inadequate efficacy or high toxicity for clinical use, possibly as a result of chemical instability or unrecognized interactions with multiple protein targets [3,4].

Despite the early clinical failures of first-generation spindle poisons, paclitaxel, a microtubule depolymerization inhibitor, has been highly successful in clinical settings and is known to be the most broadly effective and commercially successful anti-cancer agent to date. This success has

led to extensive efforts to develop other tubulin poisons with improved pharmacokinetic profiles and selectivity. Interestingly, these tubulin binders are also found to interact with tumor endothelial cells, leading to a rapid occlusion of tumor vasculature and resultant necrotic cell death [5,6]. These vascular disrupting agents (VDAs) selectively block established tumor vasculature and prevent tumor progression rapidly, whereas conventional anti-angiogenesis agents inhibit the formation of new blood vessels, thereby preventing tumor growth over the long term. Currently, several notable VDAs, including combretastatin A-4 phosphate (CA4P), DMXAA, ZD6126, and BNC105, are undergoing clinical trials [7, 8, 9, 10].

Considering the unique selectivity and effectiveness of tubulin binding VDAs, our team has been working to develop a new class of anti-cancer drugs having dual effects: tumor vasculature disruption and mitotic arrest. In this paper, we report the design, synthesis and biological evaluation of aryl oxazole derivatives as dual-action anti-cancer agents and present a complete SAR study of the new core to identify essential structural properties required for dual effects. We designed and synthesized a series of heterocyclic small molecules containing oxazoles and isoxazoles based on a previous structure-activity relationship (SAR) study on colchicine binding sites of tubulin [11].

We evaluated biological activity of the newly synthesized compounds *in vitro* and *in vivo*. First, we incubated human leukemia cells (HL-60) with our compounds to evaluate inhibitory effect on tumor cell growth *in vitro*. Second, we measured the vascular disrupting effect of our compounds using human umbilical vein endothelial cells (HUVEC). Finally, we measured the inhibitory effect of our compounds against tubulin polymerization. Combined with a microsomal stability test, we were able to identify two final compounds that are stable against metabolism but also inhibit tubulin polymerization and HUVEC growth at low concentrations. Anti-cancer activities of two selected compounds were evaluated *in vivo* using tumor-bearing mice.

Computational design

Colchicine (**1**), a natural product from plants, is known to bind to β -tubulins and inhibit tubulin polymerization. Despite the high toxicity of colchicine, which is comparable to arsenic poisoning, its excellent binding affinity toward spindle fibers makes it an attractive lead compound as an anti-cancer agent. To date, most of the related studies have focused on developing small molecules targeting colchicine binding sites with low toxicity. One of the most notable examples is ABT-751 (**2**) (Figure 1A) [12]. Compound 2 is a synthetic small molecule selected from random screening of anti-bacterial sulfonamides, and recently demonstrated promising anti-cancer effects in Phase II trials [13]. By taking a similar approach, we tested an in-house library of compounds with N-phenylpyrazole, 4,5-hydropyrazole, and oxazole core for cytotoxicity against various tumor cell lines (details not shown).

Our preliminary results showed that some of these compounds demonstrated potent cytotoxicity against tumor cell lines and also inhibited tubulin polymerization that is required for dual effects. Based on these preliminary data, we hypothesized that these tested compounds might bind to tubulin in the same way that colchicine binds. Therefore, we carried out molecular modeling studies to design a series of analogs that occupy the colchicine binding domain of tubulin. We selected compound **3**, one of the most potent cytotoxic agents in the screening library, docked it in the colchicine binding domain, and superimposed it with colchicine and **2** in the crystal structures as shown in Figures 1B and 1C (PDB codes: 3UT5 and 3HKC, respectively). Compound **3** appeared to fit in the colchicine binding site and partially overlapped with a docked colchicine in the hydrophobic binding pocket as shown in Figure 1B. The estimated binding energy of compound **3** (Gscore = -4.88kcal/mol) was much higher than that of colchicine **1** (Gscore = -6.789kcal/mol). It has been reported that the A-ring with three methoxy groups serves as an anchor to place

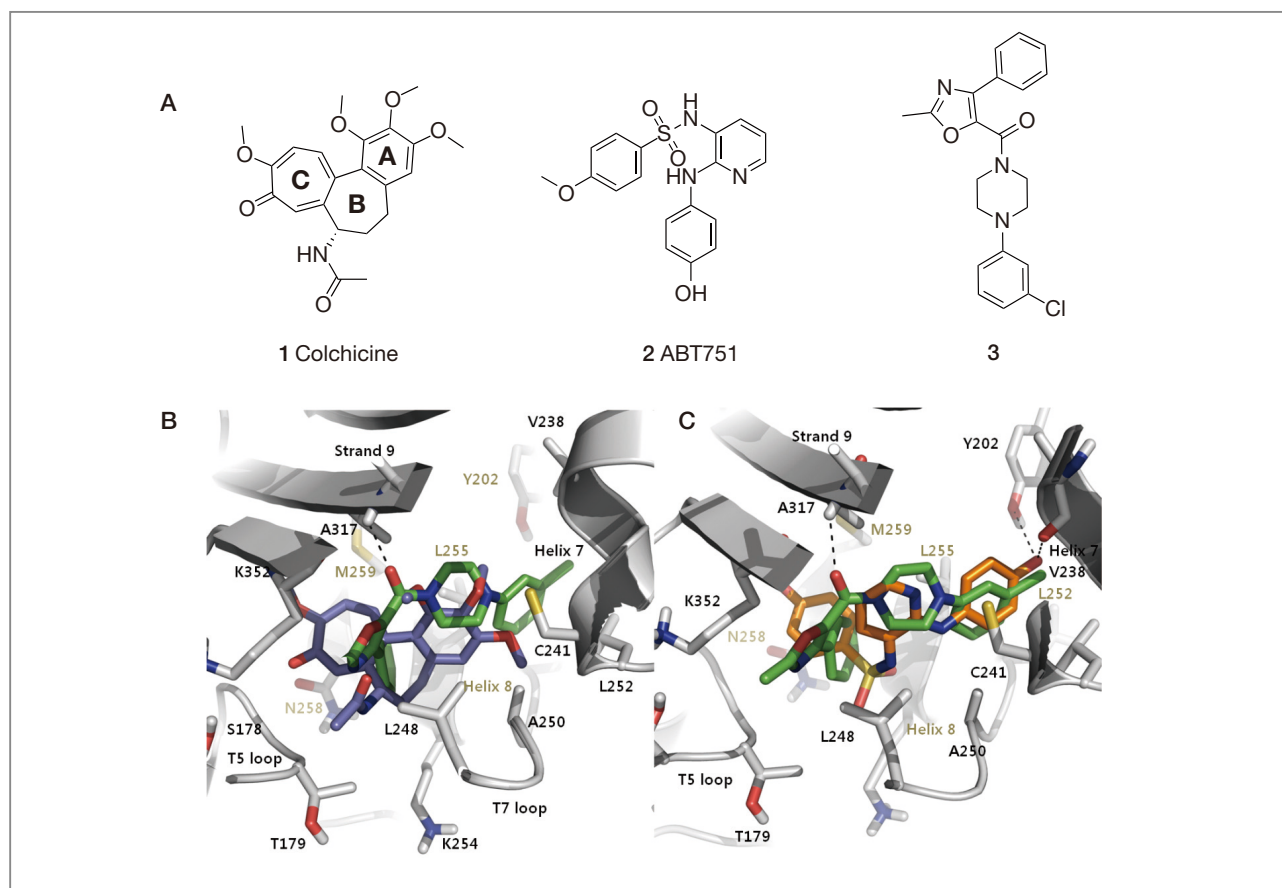


Figure 1. (A) Structures of **1** (colchicine), **2** (ABT751) and **3** (B). The docked pose of compound **3** (green) and **1** (purple) in the colchicine binding pocket (PDB code: 3UT5). (C) The docked pose of compound **3** (green) and **2** (orange) in the colchicine binding pocket (PDB code: 3HKC).

the C ring of colchicine in the proper orientation within the binding site [14,15]. Therefore, the apparent lack of this anchoring effect in **3** may lead to a slight perturbation inside the binding pocket, resulting in higher binding energy. However, it should be noted that compound **3** has an extra carbonyl group, which provides an additional hydrogen bond with the amide nitrogen of Ala317 in the backbone of β -strand 9 compared to colchicine. Interestingly, the methyl group of the oxazole ring in **3** is pointed toward the α -tubulin T5 loop, which also appears to partially overlap with the *N*-acetyl substituent of colchicine. Conformational changes of the T5 loop are known to be involved in the assembly of tubulin $\alpha\beta$ heterodimers, indicating that the methyl group of the oxazole moiety may be critical for its biological activity

[16, 17].

When compound **3** was docked in the colchicine binding domain, **3** appeared to overlap very well with the bound **2** as shown in Figure 1C. However, the estimated binding energy of compound **3** (Gscore = -4.88kcal/mol) was also higher than that of **2** (Gscore = -6.89kcal/mol). One possible explanation is that the hydroxyl group on the aniline moiety of **2** forms hydrogen bonds with Tyr202 and Val238, which is absent in **3**. On the other hand, the 3-chlorophenyl ring of **3** extended deeper into the strand S6 of the *N*-terminal nucleotide binding domain, thus it provided additional interactions with hydrophobic residues, such as Leu252, Leu242, Val238, Leu255, and Tyr202. Based on the binding mode analyses of compound **3**, the oxazole analogs fit in the

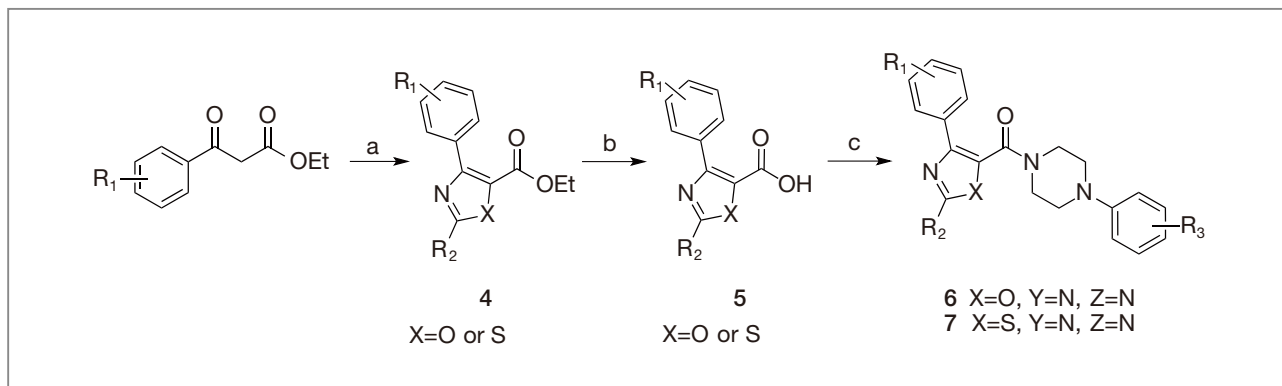
colchicine binding domain and can be further optimized by additional structural modifications. Therefore, a series of analogs containing the various substituted aryl oxazole and thiazole groups was designed and synthesized.

Structure-activity relationship and *in vitro* cytotoxicity

Aryl oxazole derivatives were prepared according to Scheme 1. Cytotoxic effects of all the synthesized derivatives were first evaluated by measuring cell viability of human leukemia cells (HL-60) upon the treatment of each compound at different concentrations. CYT997 a known cytotoxic vascular disrupting agent [18] was also tested as a reference. Among the oxazole derivatives with a phenyl group (Table 1), the 3-substituted aryl piperazine derivatives (**3**, **6-2**, **6-4**, **6-6**) showed good cytotoxic effects having IC_{50} values in the low nanomolar range. Despite having substituents with different electronegativity values, all four compounds have similar IC_{50} values (35~45 nM) suggesting that electronegativity on the 3-position does not affect cytotoxicity significantly; however, when a fluoride was placed on either the 2- or 4-position (**6-5**, **6-7**), IC_{50} values increased markedly. It should also be noted that if the 3-position was substituted with slightly bulkier groups, such as trifluoromethyl (**6-9**) or

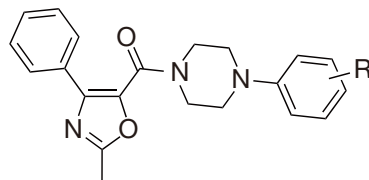
the aminoacetyl group (**6-13**), IC_{50} values increased up to 2~3 fold. Additionally, when these bulkier groups were placed on the 4-position, these compounds completely lost cytotoxicity, indicating that the size and the position of the substituents seem to be more important factors than electronegativity. Some of the derivatives with multiple substituents also showed excellent cytotoxicity; for example, 3,5-dimethoxy substituted compounds (**6-20**) exhibited the lowest IC_{50} value (19.2 nM) among this series. Both 3,5-dimethyl and -dichloro substituted derivatives also demonstrated good cytotoxicity; however, when these substituents were moved to different positions, such as 2,6-, 2,4-, or 2,3-, these compounds became much less potent, again indicating that steric factor is critical for the cytotoxicity of these derivatives.

To investigate the effect of the substituents on the phenyl ring directly linked to the oxazole core, we modified the phenyl ring with methoxy groups (**6-29~6-31**), hydrophilic groups (**6-32~6-37**), and halogen groups (**6-38~6-63**) and tested cytotoxicity as shown in Table 2. All the derivatives with hydrophilic substituents and methoxy groups (**6-29~6-37**) became much less potent compared to their non-substituted counterparts, suggesting that the van der Waals interaction may play an important role in this particular binding region. All fluoro-substituted derivatives with 3,5-dimethoxy on R_2 (**6-51~6-53**) exhibited excellent cytotoxic effect with IC_{50} values



Scheme 1^a

^a Reagents and conditions: (a) (i) HDNIB, CH_3CN , reflux, 1h;(ii) acetamide (or thioacetamide), microwave 80W, 1 min; (b) (i) 1N NaOH;(ii) 1N HCl; (c) arylpiperazine, EDCI, HOBT, NMM, CH_2Cl_2

Table 1. Cytotoxic effects of (2-methyl-4-phenyloxazol-5-yl)(4-phenylpiperazin-1-yl)methanone derivatives against human leukemia cells (HL-60).

	R	IC ₅₀ (nM) ^a		R	IC ₅₀ (nM) ^a
3	3-chloro	39.2	6-15	4-pro-1-en-2-yl	NC
6-1	H	39.1	6-16	4-isopropanoyl	NC
6-2	3-methoxy	34.8	6-17	3-carbamoyl	71
6-3	3-ethoxy	151	6-18	benzo[1,3]dioxol-5-yl	251
6-4	3-cyano	39.6	6-19	2,6-dimethyl	146.1
6-5	4-fluoro	>1000	6-20	3,5-dimethoxy	19.2
6-6	3-fluoro	45	6-21	2,4-dimethyl	100.5
6-7	2-fluoro	146.8	6-22	3,4-dimethyl	43
6-8	4-trifluoromethyl	>1000	6-23	2,3-dimethyl	35
6-9	3-trifluoromethyl	152.9	6-24	2,5-dimethyl	31.3
6-10	2-trifluoromethyl	119.5	6-25	3,4-dichloro	124.3
6-11	2-chloro	124.1	6-26	3,5-dimethyl	34.5
6-12	4-methyl	>1000	6-27	3,5-dichloro	41.8
6-13	3-aminoacetyl	329	6-28	2,3-dichloro	133
6-14	4-acetyl	NC	12 (CYT997)		112.3

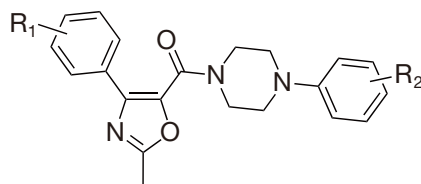
^a IC₅₀ = Compound concentration required to inhibit cell growth by 50% after cells were treated with compounds for 72h. Data are expressed as means from at least three independent experiments.

ranging from 10.3 nM~38.5 nM. When the 3,5-dimethoxy groups were replaced with a 3-chloro substituent (**6-57**~**6-59**), little or no effects were observed, confirming that electronegativity on this position does not affect overall binding. Interestingly, among all the oxazole compounds in this series, only the derivatives with the 3,5-dimethoxy groups on the R₂ position showed slightly improved activity compared to the parent compound without any substituent (**6-1**, R₁ = R₂ = H), suggesting that hydrogen bond interaction may exist in this region.

Vascular disrupting activity (HUVEC assay)

To determine the vascular disrupting effect of the synthesized compounds, we selected 18 compounds

with low IC₅₀ values ranging from 10 nM to 100 nM for further evaluation. We incubated human umbilical vein endothelial cells (HUVEC) with each compound at different concentrations to calculate the effective concentration to inhibit 50% of HUVEC growth (GI₅₀). In addition, GI₅₀ for each compound was measured at the different densities of HUVEC (HUVEC distribution, ng/mL) where inhibition of cell growth was observed. The relative ratio of GI₅₀ versus HUVEC distribution (normalized GI₅₀) was also calculated in Table 3. Representative images of the HUVEC growth assay are shown in Figure 2 in comparison with **12** (CYT997, IC₅₀ = 112.3 nM) as reference. The two most cytotoxic compounds, **6-20** (R₁ = H, R₂ = 3,5-dimethoxy, IC₅₀ = 19.2 nM) and **6-51** (R₁ = 2-F, R₂ = 3,5-dimethoxy, IC₅₀ = 10.3 nM) inhibited growth of HUVEC at the lowest concentration, 30 ng/mL, whereas **6-32** (R₁ = 3-hydroxy, R₂=3-chloro, IC₅₀ = 104.9 nM), which showed the highest

Table 2. Cytotoxic effects of (2-methyl-4-phenyloxazol-5-yl)(4-phenylpiperazin-1-yl)methanone derivatives against human leukemia cells (HL-60).

	R ₁	R ₂	IC ₅₀ (nM) ^a
6-29	4-methoxy	3-chloro	NC
6-30	3,4-dimethoxy	3-chloro	NC
6-31	3-methoxy	3-chloro	NC
6-32	3-hydroxy	3-chloro	104.9
6-33	3-sodium phosphate	3-chloro	>1000
6-34	4-hydroxy-3-methoxy	3-chloro	85.9
6-35	3-methoxy-4-sodium phosphate	3-chloro	303
6-36	3-hydroxy-4-methoxy	3-chloro	NC
6-37	3-aminoacetyl	3-chloro	208
6-38	2-fluoro	4-pro-1-en-2-yl	NC
6-39	4-fluoro	4-chloro	NC
6-40	4-chloro	3-isopropanoyl	NC
6-41	4-fluoro	2,5-dimethyl	358
6-42	2-fluoro	2,5-dimethyl	318.9
6-43	4-fluoro	4-isopropanoyl	NC
6-44	3-fluoro	2,5-dimethyl	204.2
6-45	2-chloro	2,5-dimethyl	>1000
6-46	3-chloro	2,5-dimethyl	345.2
6-47	4-chloro	2,5-dimethyl	NC
6-48	2-fluoro	3,5-dichloro	60.2
6-49	3-fluoro	3,5-dichloro	41.7
6-50	4-fluoro	3,5-dichloro	52.1
6-51	2-fluoro	3,5-dimethoxy	10.3
6-52	3-fluoro	3,5-dimethoxy	28.2
6-53	4-fluoro	3,5-dimethoxy	38.5
6-54	2-fluoro	3,5-difluoro	186.2
6-55	2-fluoro	5-chloro-2-methyl	228.7
6-56	2-fluoro	5-chloro-2-methoxy	152.9
6-57	2-fluoro	3-chloro	39.4
6-58	3-fluoro	3-chloro	33.7
6-59	4-fluoro	3-chloro	40.1
6-60	2-chloro	3-chloro	132.4
6-61	2-fluoro	3-methoxy	56.1
6-62	3-fluoro	3-methoxy	NC
6-63	4-fluoro	3-methoxy	112.3

^a IC₅₀ = Compound concentration required to inhibit cell growth by 50% after cells were treated with compounds for 72h. Data are expressed as means from at least three independent experiments.

Table 3. Effects of selected compounds on capillary formation by human umbilical vein endothelial cells (HUVECs).

	HUVEC distribution ^a (ng/mL)	GI ₅₀ ^b (ng/mL)	b/a
3	100	463	4.6
6-1	300	9,631	32.1
6-4	100	2,520	25.2
6-6	100	1,052	10.5
6-20	30	319	10.6
6-22	300	3,522	11.7
6-23	100	380	3.8
6-24	100	1,732	17.3
6-26	100	356	3.6
6-27	100	191	1.9
6-32	1000	-	-
6-34	300	-	-
6-48	100	177	1.77
6-49	100	134	1.34
6-50	300	-	-
6-51	30	118	3.93
6-52	100	126	1.26
6-53	300	-	-
12	100	2098	20.98

^a Data represents starting concentrations of each compound for the disruption of capillary-like structure formation; ^b GI₅₀: Effective concentration of the tested compounds to inhibit 50% of growth.

IC₅₀ among the selected compounds, inhibited growth of HUVEC only at 1000 ng/mL. All other compounds inhibited growth of HUVEC at 100~300 ng/mL. This result indicates that *in vitro* cytotoxicity of these compounds correlates with vascular disrupting activity.

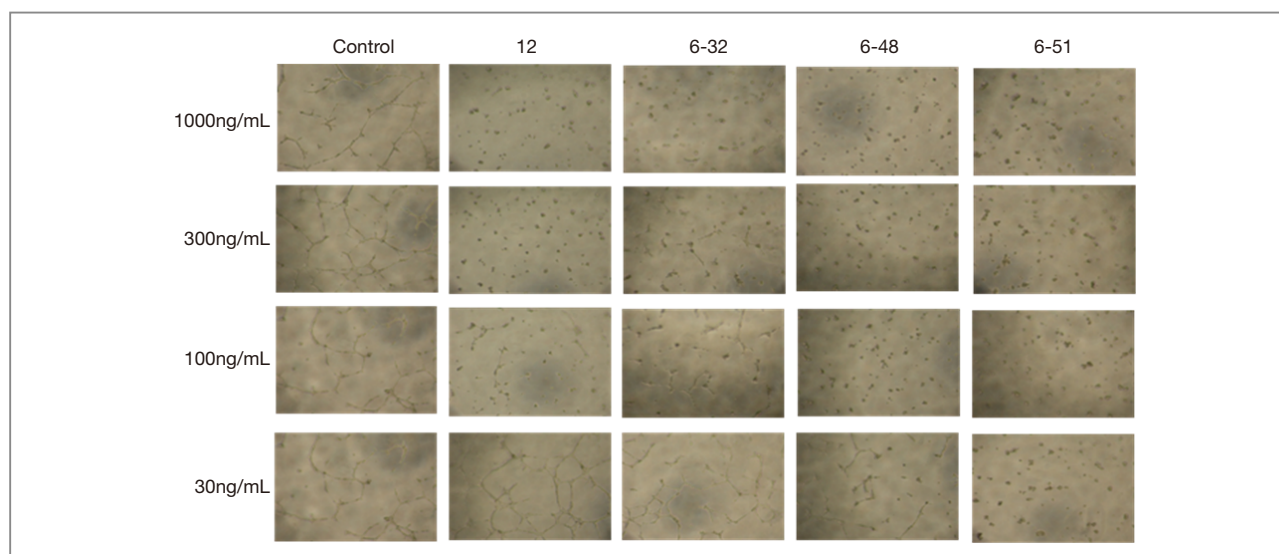
Tubulin polymerization inhibition (TPI test)

In order to examine the ability to block tubulin polymerization of the synthesized compounds, we tested

Table 4. Inhibition of tubulin polymerization of selected compounds.

Compound	IC ₅₀ (μg/mL) ^a
6-1	0.62
6-23	0.53
6-27	0.67
6-48	0.73
6-49	0.77
6-51	0.71
13 (AC7739)	1.01

^a The tubulin concentration was 4mg/ml. Data are expressed as means from at least three independent experiments.

**Figure 2.** Representative images of HUVECs (human umbilical vein endothelial cells) test. HUVECs were placed onto a thick layer of Matrigel in the presence of vehicle (control) or tested compounds at the indicated concentrations.

several compounds with high cytotoxicity as shown in Table 4. Interestingly, all tested compounds inhibited tubulin polymerization at the lower concentrations compared to a known polymerization inhibitor **13** (AC7739) [19], indicating that cytotoxicity and vascular disrupting activity of these compounds are due to the inhibition of tubulin polymerization during mitosis.

Tumor growth inhibition *in vivo*

Considering *in vitro* biological activity and metabolic stability, we selected **6-48** and **6-51** and evaluated anti-tumor activity *in vivo* using a simple tumor xenograft model (HCT-116, human colorectal carcinoma) (Figure 3). Tumor-bearing mice were injected with each compound once a day for 14 days intraperitoneally and tumor volumes were determined by caliper measurements. After five days of the treatment of **6-48**, significant inhibition of tumor growth was observed at 50 and 100 mg/kg. When compared to untreated mice, the treatment of compound **6-48** reduced the size of tumors to 42% at 100 mg/kg and 16.1% at 50 mg/kg, while 19% of body weight was lost at 100 mg/kg and 10.8% at 50 mg/kg.

When we injected 200mg/kg of **6-48**, tumor growth was inhibited markedly; however, two out of six mice died during the experiment, indicating that **6-48** is toxic at high concentrations. Unfortunately, despite having potent activity *in vitro*, the treatment of **6-51** did not affect tumor growth *in vivo* and did not seem to change body weight. Based on the microsomal stability test, we believe that due to poor metabolic stability, **6-51** may have degraded during systemic circulation before the compound reached its therapeutic target.

Conclusion

We developed a series of aryloxazole as anti-mitotic and vascular disrupting agents. *In vitro* cytotoxicity was evaluated using various tumor cell lines and tumor vascular disrupting activity was also tested using HUVEC assay. Several compounds with excellent cytotoxicity and vascular disrupting activity were selected, and metabolic stability and inhibition of tubulin polymerization were examined. As a result, the two most potent compounds, **6-48** and **6-51**, were chosen for further *in vivo* evaluation of anti-tumor activity. Compound **6-51** ($R_1 = 2-F$, $R_2 =$

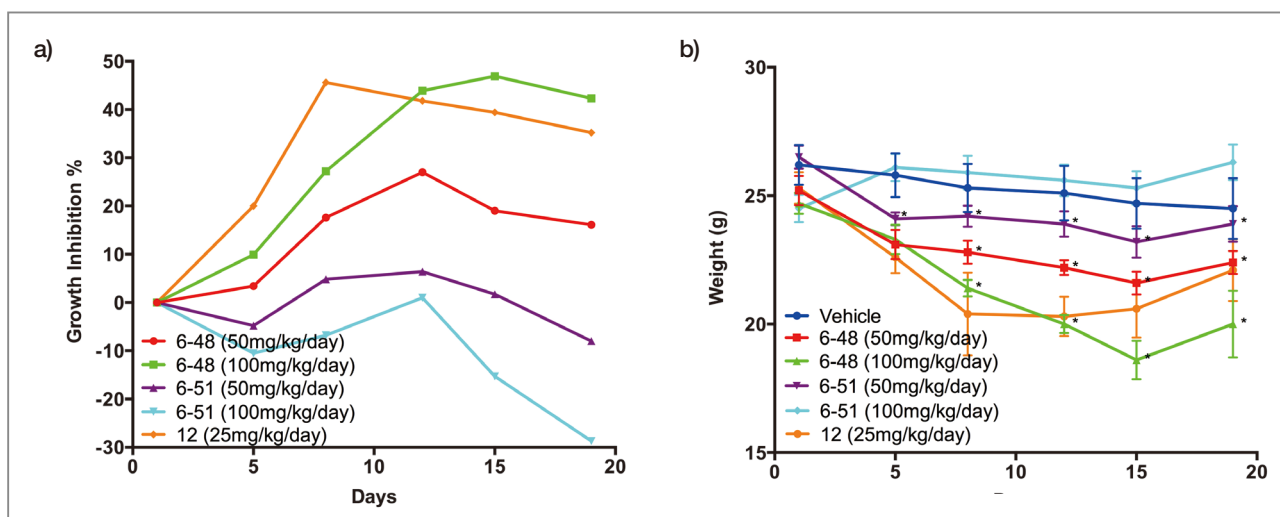


Figure 3. Antitumor effects of daily administration of compounds **6-48** and **6-51**: (a) tumor growth inhibition by **6-48** and **6-51** in HCT-116 colon cancer xenograft model (calculated based on vehicle control); (b) changes in body weight over the course of the treatment.

3,5-OMe) exhibited the highest cytotoxicity, with IC_{50} value of 10.3 nM against HL-60, and excellent vascular disrupting activity. While compound **6-51** seemed only moderately stable in liver microsomes (15% for human, 16.6% for mice), compound **6-48** ($R_1 = 2-F$, $R_2 = 3,5-Cl$) demonstrated an outstanding microsomal stability (82.3% for human, 49% for mice) although it showed relatively lower cytotoxicity ($IC_{50} = 60.5$ nM) and vascular disrupting activity compared to **6-51**. Both of these compounds inhibited tubulin polymerization at low concentrations suggesting that their biological activity comes from tubulin binding. When injected into tumor-bearing mice, compound **6-48** effectively reduced tumor growth (42.3% in size) at 100 mg/kg; however, compound **6-51** did not affect tumor growth, apparently due to its poor metabolic stability.

In summary, we developed a dual-action anti-cancer agent containing aryloxazole moiety. Compound **6-48** showed excellent anti-mitotic effect and vascular-disrupting activity *in vitro*, and demonstrated promising anti-tumor activity *in vivo*, possibly due to its metabolic stability. It is interesting to note that **6-48** showed greater effects in tumor growth *in vivo* despite having much lower *in vitro* potency as compared to **6-51**. Many tubulin binders are highly toxic and have short lives, limiting their capacity to shut down tumor vasculature effectively and possibly leaving an outer rim of viable cancer cells [21]. Nevertheless, we believe that this compound provides excellent results which will lead to the discovery of other potent dual-acting agents.

Note

This article and images are drawn from "Synthesis and biological evaluation of aryloxazole derivatives as antimetabolic and vascular disrupting agents for cancer therapy" in *J. Med. Chem.* 2013, vol. 56, pp. 9008-9018.

References

- [1] Wood KW, Cornwell WD, Jackson JR. *Curr. Opin. Pharmacol.* 2001; 1: 370-377.
- [2] Dumontet C, Jordan MA. *Nat. Rev. Drug. Discov.* 2010; 9: 790-803.
- [3] Goldspiel BR. *Pharmacotherapy* 1997; 17: 110S-125S.
- [4] Budman DR. *Cancer Invest.* 1997; 15: 475-490.
- [5] Lippert JW. *Bioorg. Med. Chem.* 2007; 15: 605-615.
- [6] Patterson DM, Rustin GJ. *Clin. Oncol. (R. Coll. Radiol.)* 2007; 19: 443-456.
- [7] Tron GC, Pirali T, Sorba G, Pagliai F, Busacca S, Genazzani AA. *J. Med. Chem.* 2006; 49: 3033-3044.
- [8] Baguley BC. *Lancet Oncol.* 2003; 4: 141-148.
- [9] Davis PD, Dougherty GJ, Blakey DC, Galbraith SM, Tozer GM, Holder AL, Naylor MA, Nolan J, Stratford MR, Chaplin DJ, Hill SA. *Cancer Res.* 2002; 62: 7247-7253.
- [10] Flynn BL, Gill GS, Grobely DW, Chaplin JH, Paul D, Leske AF, Lavranos TC, Chalmers DK, Charman SA, Kostewicz E, Shackelford DM, Morizzi J, Hamel E, Jung MK, Kremmidiotis G. *J. Med. Chem.* 2011; 54: 6014-6027.
- [11] Nguyen TL, McGrath C, Hermone AR, Burnett JC, Zaharevitz DW, Day BW, Wipf P, Hamel E, Gussio R. *J. Med. Chem.* 2005; 48: 6107-6116.
- [12] Yoshino H, Ueda N, Nijima J, Sugumi H, Kotake Y, Koyanagi N, Yoshimatsu K, Asada M, Watanabe T, Nagasu T, et al. *J. Med. Chem.* 1992; 35: 2496-2497.
- [13] Rudin CM, Mauer A, Smakal M, Juergens R, Spelda S, Wertheim M, Coates A, McKeegan E, Ansell P, Zhou X, Qian J, Pradhan R, Dowell B, Krivoshik A, Gordon G. *J. Clin. Oncol.* 2011; 29: 1075-1082.
- [14] Andreu JM, Perez-Ramirez B, Gorbunoff MJ, Ayala D, Timasheff SN. *Biochemistry* 1998; 37: 8356-8368.
- [15] Sharma S, Poliks B, Chiauzzi C, Ravindra R, Blanden AR, Bane S. *Biochemistry* 2010; 49: 2932-2942.
- [16] Dorleans A, Gigant B, Ravelli RB, Mailliet P, Mikol V, Knosow M. *Proc. Natl. Acad. Sci. U. S. A.* 2009; 106: 13775-13779.
- [17] Ravelli RB, Gigant B, Curmi PA, Jourdain I, Lachkar S, Sobel A, Knosow M. *Nature* 2004; 428: 198-202.

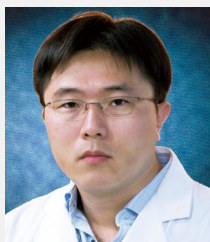
- [18] Burns CJ, Harte MF, Bu X, Fantino E, Joffe M, Sikanyika H, Su S, Tranberg CE, Wilson N, Charman SA, Shackelford DM, Wilks AF. *Bioorg. Med. Chem. Lett.* 2009; 19: 4639-4642.
- [19] Ohsumi K, Nakagawa R, Fukuda Y, Hatanaka T, Morinaga Y, Nihei Y, Ohishi K, Suga Y, Akiyama Y, Tsuji T. *J. Med. Chem.* 1998; 41: 3022-3032.
- [20] Walle T. *Int. J. Mol. Sci.* 2009; 10: 5002-5019.
- [21] Gaya AM, Rustin GJ. *Clin. Oncol. (R. Coll. Radiol.)* 2005; 17: 277-290.



Center for Neuro-Medicine

[Feature Articles]

Development of Conjugated Polymer Nanoparticles to Achieve Bright Near-Infrared Fluorescence and On/Off Photoswitching for Contrast-Enhanced Biomedical Imaging



Sehoon Kim

Center for Theragnosis
sehoonkim@kist.re.kr

In fluorescence bioimaging, switchable signals have been exploited to overcome inherent limitations of the photon-based modality, such as interference with light absorption, scattering and autofluorescence from biological tissues. Fluorescence switching by specific physiological factors, such as pH, enzyme activity or other biologically relevant chemicals, has been widely studied to provide sensing/diagnostic information. Switching by photostimulation is another possible way to improve the detectability as well as spatial resolution of fluorescence imaging. In an autofluorescence-rich *in vivo* environment, probes whose signal modulation is synchronized with remote photoswitching can allow a dynamic signal to be distinguished from a static autofluorescence background to improve the capability of signal identification. The *in vivo* utilization of such probes, however, is still in its infancy due to their low switching contrast and stability, limited emission brightness with greater tissue interference in the visible window, and complexity in probe synthesis and delivery formulation. To date, some conceptual examples have been demonstrated in small transparent animals such as *caenorhabditis elegans* or zebrafish.

In an effort to provide high-performance photoswitchable probes that can fulfill stringent requirements for *in vivo* imaging, we devised a molecular integration approach toward composite nanococktails (NCs) possessing (1) bright fluorescence in the near-infrared (NIR) region with less tissue interference, (2) reversible and repeatable photoswitching

with high on/off contrast, (3) excellent on/off memory bistability for nondestructive fluorescence readout under physiological conditions, and (4) tiny colloidal size with water dispersibility for *in vivo* delivery. Specifically, we prepared closely integrated binary NCs that are constituted of a photochromic bisthiénylene derivative and a π -conjugated polymer showing bright solid-state fluorescence. Here, the fluorescence can be turned on and off by alternate photochromic switching between colorless- and colored-nonfluorescent states, where the

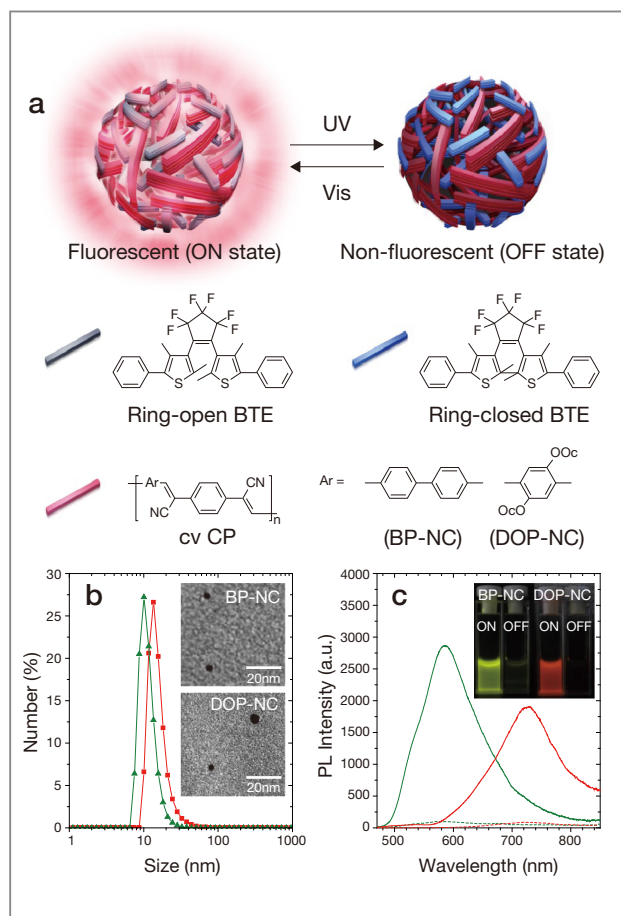


Figure 1. a) Schematic representation of the cvCP/BTE-integrated binary NCs and their photoswitching reaction by UV/visible light illumination. b) Number-averaged hydrodynamic size distributions and representative TEM images (inset) of BP-NC (green) and DOP-NC (red). c) Photoluminescence spectra (PL, excited at 450 nm) of BP-NC (green) and DOP-NC (red) in the switched "ON" (solid) and "OFF" (dashed) states and their fluorescence photographs taken under a 365-nm handheld UV lamp (inset).

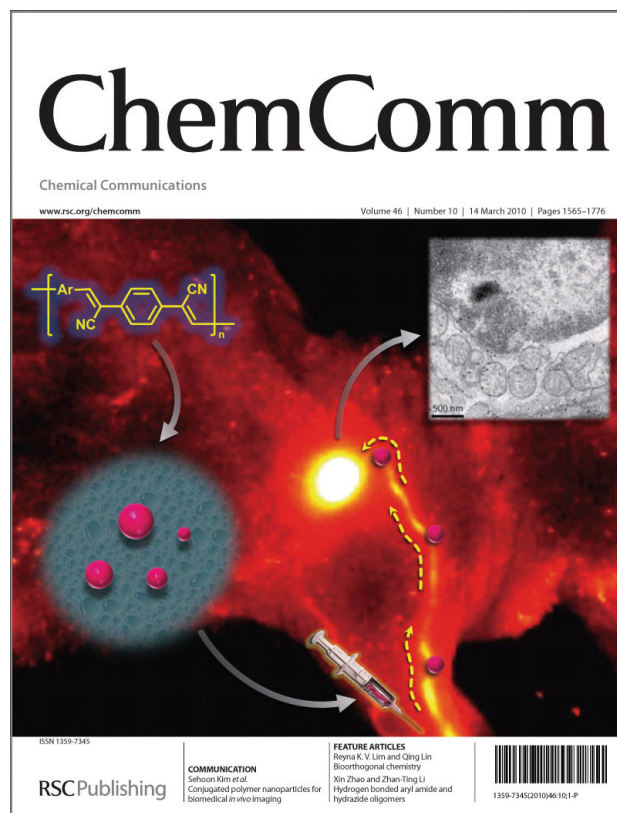


Figure 2. Cover article in *Chemical Communications* highlighting the work of our KIST research group [1].

latter can quench the emission through fluorescence resonance energy transfer (FRET) (Figure 1). This dense physical assembly allows for facile integration and optimization between dual functions (solid-state NIR fluorescence and photochromism) in the form of tiny nanoparticles to successfully accomplish *in vivo/ex vivo* photoswitching and biomedical imaging in murine models.

In the construction of photoswitchable binary NCs, we employed cyanovinylene-backboned conjugated polymers (cvCP) as a nanoscopically-concentrated fluorescence emitter and a bisthiénylene derivative, 1,2-bis(2,4-dimethyl-5-phenyl-3-thienyl)-3,3,4,4,5,5-hexafluoro-1-cyclopentene (BTE) as a photoswitching modulator. Recently, we reported that the cvCP-aggregated nanoparticles show bright solid-state fluorescence in the visible-to-NIR region, useful for *in vivo* imaging (Figure 2), where the solid-state fluorescence is opposed to

the “self-quenching” of fluorescence typical of common dyes or red/NIR-emissive conjugated polymers at high concentration or in the aggregated state [1]. This unique phenomenon of solid-state (or aggregation-enhanced) fluorescence can afford intense fluorescence output that is proportional to the number density of nanoscopic emitters, which would be useful for biomedical *in vivo* imaging. As for the switching constituent, BTE derivatives are known to have highly efficient and reversible photochromism with thermal bistability between the UV-absorbing colorless ring-open form and the colored ring-closed isomer with broad absorption up to the NIR (Figure 1a). These attributes of BTE are considered appropriate for the stable photoswitching of NIR fluorescence at body temperature ($\sim 37^\circ\text{C}$).

Taking these advantages into consideration, we attempted nanoscopic high-density integration between solid-state emitters and photochromic molecules, which would combine intense fluorescence and high-contrast on/off photoswitching by allowing for inter-species close proximity that is a prerequisite for efficient FRET interaction. As a proof of concept, cvCP/BTE-integrated binary NCs were prepared via Knoevenagel polymerization of cvCP in the presence of BTE within the hydrophobic interior of water-dispersed surfactant micelles. This *in situ*

colloidal polymerization produced very fine composite nanoparticles that were stably dispersed in an aqueous milieu (Figure 1b) and showed high-contrast on/off photoswitching of bright fluorescence in the NIR (Figure 1c).

To validate the *in vivo* utility of our photoswitchable NCs, imaging experiments were conducted with NIR-emissive DOP-NC. First, the capability to improve signal identification was demonstrated by photoswitching DOP-NC on/off and observing the modulating signal through a thick biological specimen with huge autofluorescence (Figure 3a). In this *in vivo*-mimicking condition, the emission intensity from the switched-on DOP-NC was shown to be indistinguishable from nonspecific background signals under excitation at 430 nm. Such a low-contrast imaging result is a typical situation often experienced when using non-switchable fluorescent probes. However, the alternate irradiation of switching lights turned only the photoswitchable DOP-NC signal on and off without autofluorescence alteration, rendering it distinguishable from the static background. As a result, high-contrast signal identification was apparent in the image reflecting the difference between the switched on and off states (Figure 3b), clearly demonstrating the potential advantage of fluorescence photoswitching for background-rich *in vivo* imaging.

In a subsequent experiment, we assessed the potential of the photoswitchable NCs for biomedical imaging by performing sentinel lymph node (SLN) mapping that is of clinical importance for cancer staging and surgery (Figure 4). When the switched-off DOP-NC was injected intradermally into the forepaw pad of a mouse at a dose of 0.08 mg/kg bodyweight, no fluorescence signal could be observed by the naked eye nor even with a high-sensitivity imaging system. To turn the DOP-NC fluorescence on, an intense red laser (655 nm) was shone on a spot (ca. 2 mm in diameter) around the axilla at 5 min post-injection. Through this photoswitching operation, a fluorescing spot appeared near the laser-irradiated position, clearly locating a subcutaneous SLN

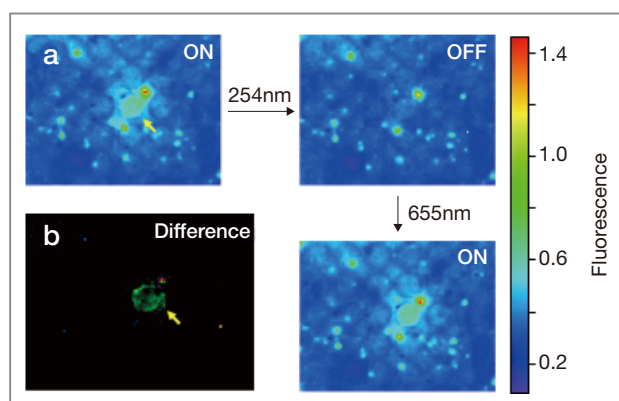


Figure 3. a) Fluorescence images of a biological tissue (2.3 mm thick chicken ham; $\lambda_{\text{ex}} = 430 \text{ nm}$, $\lambda_{\text{em}} = 720 \text{ nm}$) with the photoswitching modulation of DOP-NC underneath. b) Image of difference between the switched “ON” and “OFF” states. The DOP-NC signal is indicated with yellow arrow.

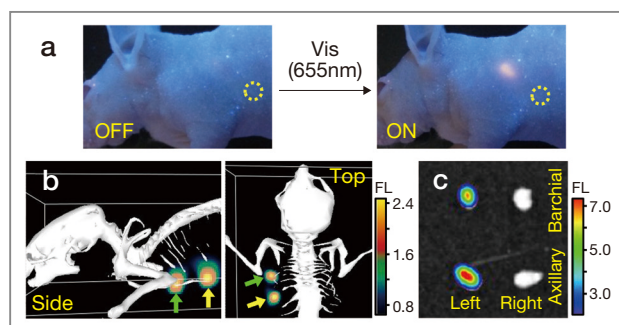


Figure 4. a) True color images of a mouse injected intradermally with switched-off DOP-NC into the left forepaw. The images were taken at 5 min post-injection under UV excitation by a 365-nm handheld lamp before (left) and after (right) red laser irradiation. Circles indicate the laser-illuminated position. b) 3D reconstructed images registered on a mouse atlas, taken after selectively turning the DOP-NC fluorescence on at the lymph nodes. Green and yellow arrows indicate axillary and brachial nodes, respectively. c) Lymph nodes resected from the switched-on mouse body.

with a bright signal that could be noninvasively recognized even by the naked eye (Figure 4a). It should be noted that the laser-irradiated and fluorescence-activated locations were not the same, but were far apart, suggesting the occurrence of a photoswitching reaction by the diffused laser light through the tissue. After photoswitching-on with the high on/off contrast (~ 16), it is clear from the image in the 3D-reconstructed representation that the administered NCs had accumulated at two node-like regions as early as 5 minutes post-injection (Figure 4b). The *ex vivo* imaging verified that the two fluorescing organs resected from the NC-injected side were axillary and brachial nodes (Figure 4c).

Conclusion

We have developed a new type of photoswitchable nanoprobe based on binary composite nanococktails (NCs) that are well suited for *in vivo* applications. Nanoscopically close integration between cvCP and BTE via *in situ* colloidal polymerization offered physically assembled nanoconstructs showing bright fluorescence in the NIR, high-contrast photoswitching through the

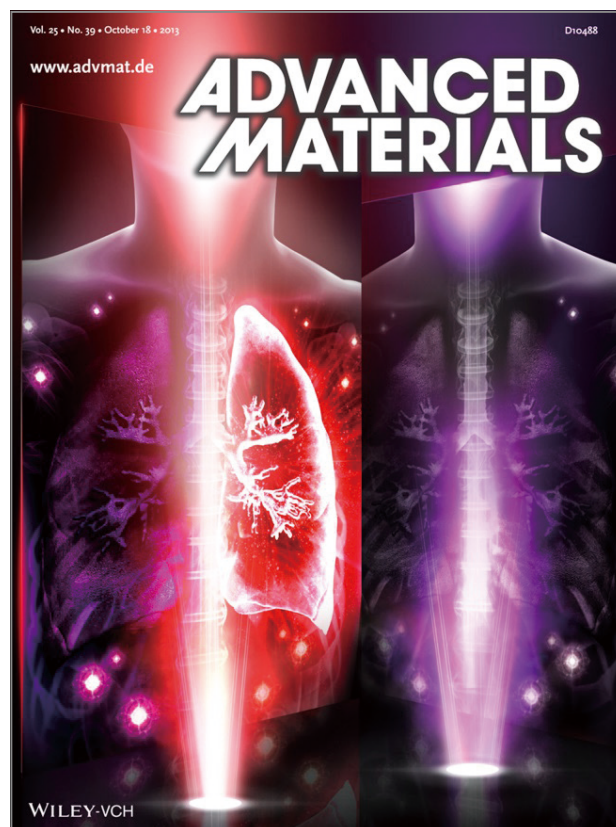


Figure 5. Cover of *Adv. Mater.* refers to feature article of our KIST research group.

efficient intraparticle FRET, a nondestructive fluorescence readout with on/off bistability and reversibility, and tiny colloidal size with high structural integrity for *in vivo* delivery. All these combined merits enabled high-precision inscription and identification of imaging signals in the background-rich media, including a mouse model, thereby validating our dense nanointegration strategy of exploring photoswitchable NIR fluorescence for biomedical *in vivo* imaging.

Note

This article and images are drawn from “Conjugated Polymer/Photochromophore Binary Nanococktails: Bistable Photoswitching of Near-Infrared Fluorescence for

In Vivo Imaging” in *Adv. Mater.*, Vol.25, pp. 5574~5580.
The article was featured on the front cover of the journal
(Figure 5).

References

- [1] Kim S, Lim C-K, Na J, Lee Y-D, Kim K, Choi K, Leary JF, Kwon IC. *Chem Commun.* 2010; 46: 1617-1619.



Molecular Photonics and Biophotonics Laboratory/Center for Theragnosis

[Feature Articles]

Hydroxycinnamic Acids in *Crepidiastrum denticulatum* Protect Against Oxidative Stress- Induced Retinal Damage



**Sang Hoon
Jung**

Functional Food
Center
shjung@kist.re.kr



Chu Won Nho

Functional Food
Center
cwnho@kist.re.kr



Hong Ryul Ahn

Functional Food
Center
hrah@kist.re.kr

Introduction

As life expectancy increases, the challenge of maintaining a good quality of life also grows in importance. Among age-related diseases, diseases of the eye can present some of the most difficult challenges to the desires of the aging to maintain an active lifestyle and independence. These include glaucoma, age-related macular degeneration, cataracts, diabetic retinopathy and dry eye.

Worldwide, glaucoma is the second leading cause of blindness. It is a term used to describe a group of optic neuropathies characterized by functional and structural impairment of retinal ganglion cells resulting in progressive, irreversible vision loss, initially marked by loss of side vision with progression to total blindness [1]. This is most commonly associated with elevated intraocular pressure (IOP) and ischemia.

Age is the main risk factor for glaucoma. Not many people under the age of 40 will develop the condition, but about 2% of people over the age of 40 and 50% of those over 65 will develop the disease.

Since IOP is seen as the primary cause of glaucoma, the major clinical therapies for glaucoma are focused on reducing IOP by increasing uveoscleral outflow of aqueous humor and by inhibiting the production of aqueous humor [2]. However, these therapeutic approaches are often ineffective because significant numbers of glaucoma patients do not have raised IOP. Moreover, not all high IOP patients develop glaucoma.

According to epidemiological studies conducted in Korea, the prevalence of glaucoma among the population of rural Sangju in South Korea was 3.4%. Notably, open-angle glaucoma with low IOP was found to be the most common form, accounting for 94.4% of the total number of cases [3].

Thus, alternative treatment approaches are needed for glaucoma. One such alternative that has received increased attention among researchers is neuroprotection, which focuses on protecting retinal neurons (retinal ganglion cells - RGCs), specifically against apoptosis, without producing significant side effects.

There is a significant amount of evidence implicating the role of oxidative stress in glaucoma [4]. Antioxidant defenses neutralize oxidative stress, so it would be desirable that neuroprotective substances should also possess antioxidant properties. Numerous natural products with anti-oxidative properties have long been shown to have beneficial effects in humans and can be tolerated when taken regularly. Thus, certain natural products may be beneficial in the treatment of a chronic disease such as glaucoma.

Wild vegetables have been shown to have health benefits due to their higher levels of minerals and vitamins as compared to cultivated vegetables. This may be because wild vegetables grow under the constant stress of harsh conditions, including competition with other plants and insects. Some of these wild vegetables have been traditionally used in fermented form in Korea, specifically as kimchi.

Our research group in the Functional Food Center at KIST has collected edible wild vegetables in the vicinity of Pyeongchang, Korea, and tested whether the extracts have neuroprotective effects in transformed RGCs (RGC-5). Among the vegetables investigated, *Crepidiastrum denticulatum* (Asteraceae) showed the highest protective effect, and additional experiments were carried out to further clarify this effect.

Neuroprotective effects of *C. denticulatum* in vitro

C. denticulatum is widely cultivated in Korea, and extensively used in herbal medicines in East Asia, especially in those used for treating conditions such as inflammation, blood circulation disorders, and eye-related diseases [5].

In our study, *C. denticulatum* showed protective effects against oxidative stress (glutamate/BSO)-induced RGC-5 cell death in a concentration-dependent manner, a finding confirmed by microscopic analysis using a Hoechst 33342/PI double staining method for DNA (Figure 1).

In a previous report, we have shown that glutamate/BSO can induce apoptosis in RGC-5 cells and up-regulate cleaved caspase-3 and cleaved PARP proteins [6]. We confirmed these observations in this study and also found that pre-treatment with *C. denticulatum* inhibited this up-regulation of apoptotic proteins and mRNA level in a concentration-dependent manner (Figure 2). This suggests that *C. denticulatum*, by inhibiting the

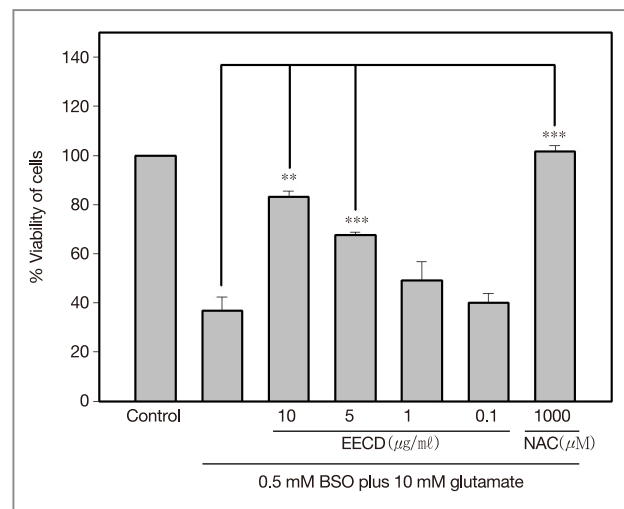


Figure 1A. Effect of EECD on the viability of RGC-5 cells exposed to 10 mM glutamate plus 0.5 mM BSO for 24 h as measured by the MTT assay. 1 mM *N*-acetyl-L-cysteine (NAC) was used as a positive control. The results are mean values with error bars indicating \pm SEM where $n = 6$ independent experiments (** $p < 0.01$, *** $p < 0.001$).

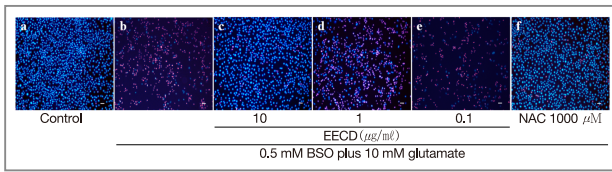


Figure 1B. Representative fluorescence microscopy of PI (red) and Hoechst 33342 (blue) staining. (a) Control RGC-5 cells in culture. (b) 10 mM glutamate plus 0.5 mM BSO treated RGC-5 cells in culture. (c–e) Pre-treatment with EECD (0.1 to 10 $\mu\text{g}/\text{mL}$ concentration) followed by 10 mM glutamate plus 0.5 mM BSO. (f) Pre-treatment with NAC (1 mM concentration) followed by 10 mM glutamate plus 0.5 mM BSO. Scale bar = 50 μm .

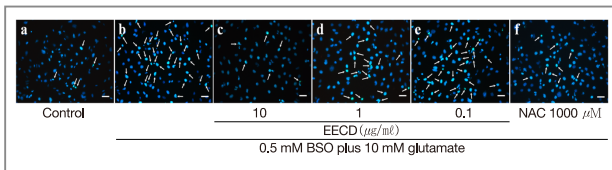


Figure 1C. Representative fluorescence microscopy of Hoechst 33342 stained RGC-5 cells. (a) Control RGC-5 cells in culture. (b) 10 mM glutamate plus 0.5 mM BSO treated RGC-5 cells in culture. (c–e) Pre-treatment with EECD (0.1 to 10 $\mu\text{g}/\text{mL}$ concentration) followed by 10 mM glutamate plus 0.5 mM BSO. (f) Pre-treatment with NAC (1 mM concentration) followed by 10 mM glutamate plus 0.5 mM BSO. Scale bar = 50 μm .

activation of apoptotic proteins, has anti-apoptotic effects that protect against retinal degeneration.

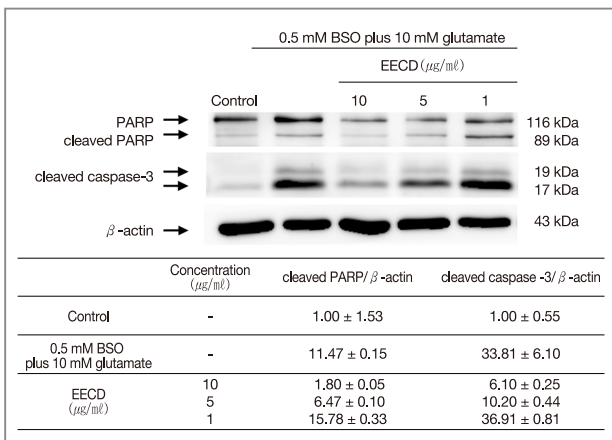


Figure 2A. Expression of apoptotic protein levels (PARP, cleaved caspase-3) in RGC-5 cells subjected to 10 mM glutamate plus 0.5 mM BSO with or without EECD treatment. Protein level values are expressed as mean \pm SEM from three independent experiments.

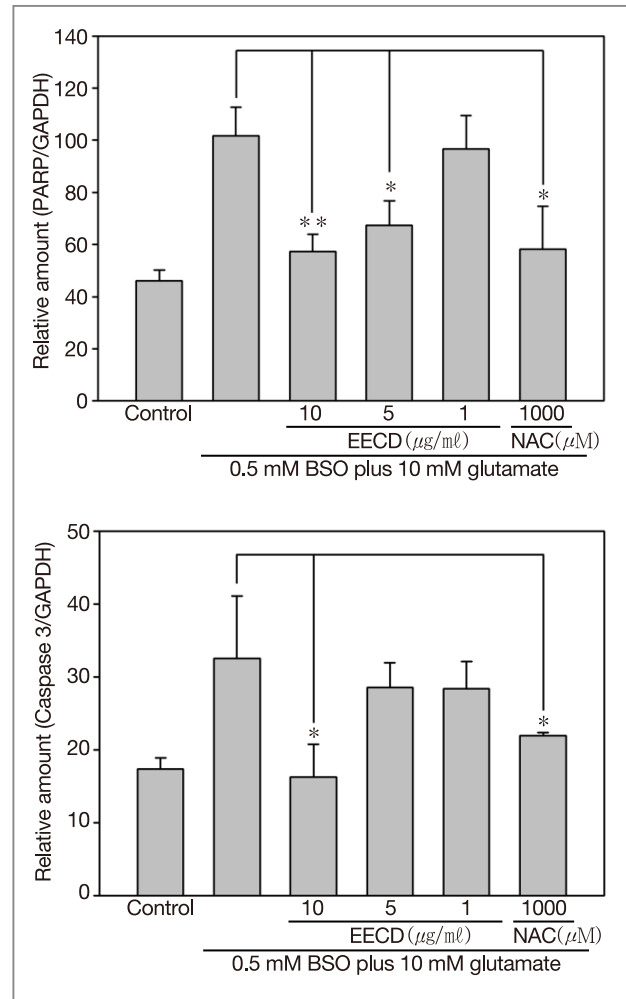


Figure 2B. Expression of mRNA level (PARP and caspase-3) in RGC-5 cells subjected to 10 mM glutamate plus 0.5 mM BSO with or without EECD treatment. Values are expressed as mean \pm SEM from three independent experiments.

Anti-oxidative effects of *C. denticulatum* and its influence in RGCs

Retinal degeneration may occur by various mechanisms including neurotrophic factor deprivation, ischemia, glial cell activation, glutamate excitotoxicity, and abnormal immune response. Moreover, these mechanisms can induce oxidative stress, and this has

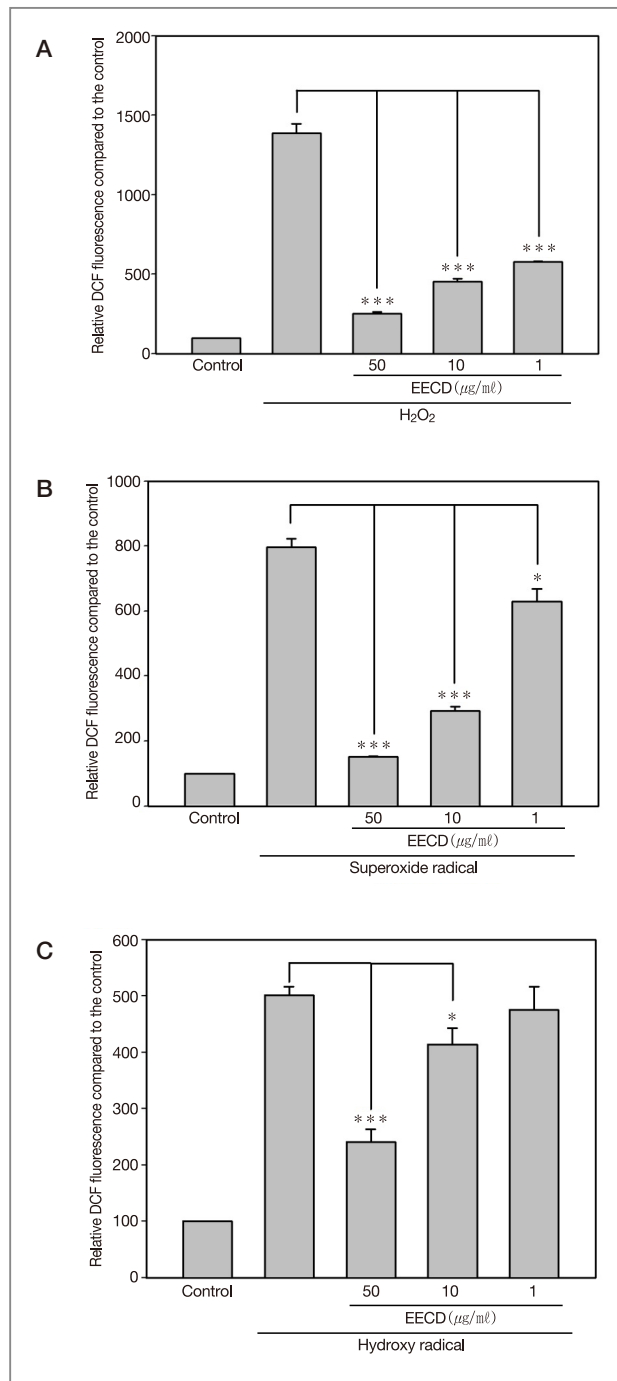


Figure 3. Radical scavenging capacities of EECD against the production of three radical species (H₂O₂, O₂^{•-} and •OH) in RGC-5. ROS production was stimulated with H₂O₂ at 1 mM, or with KO₂ at 1 mM, or with H₂O₂ at 1 mM plus ferrous perchlorate (II) at 100 μM. (A) H₂O₂-induced oxidation of DCFH in RGC-5, (B) O₂^{•-}-induced oxidation of DCFH in RGC-5, and (C) •OH-induced oxidation of DCFH in RGC-5. Results are mean values with error bars indicating ± SEM where n = 3 (* p < 0.05, *** p < 0.001)

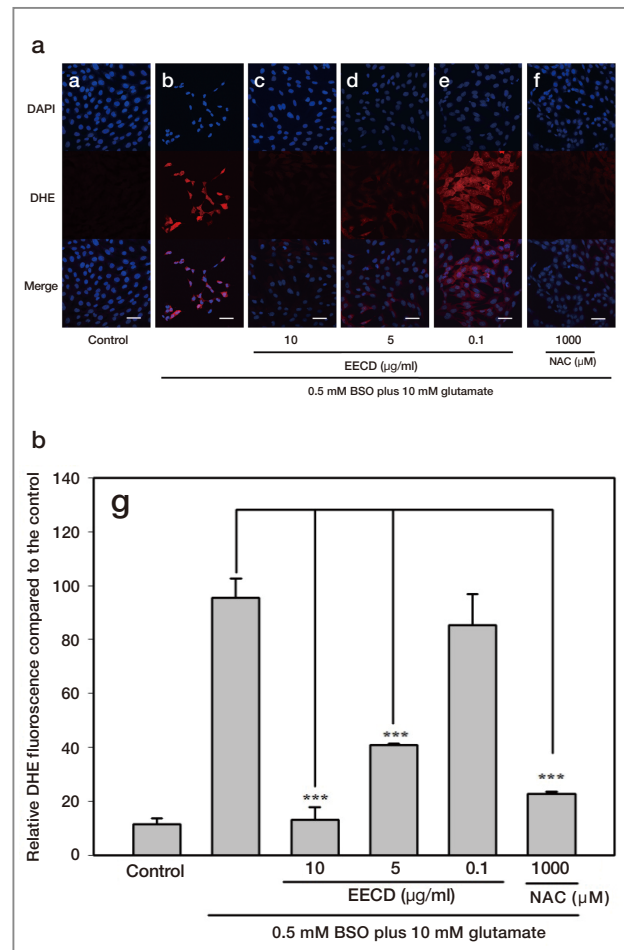


Figure 4. Effect of EECD on ROS levels in RGC-5 cells subjected to oxidative stress induced by 10 mM glutamate plus 500 μM BSO for 24 h. DHE assay was used to demonstrate the intensity of intracellular ROS generated by oxidative stress. Images were obtained by confocal microscopy (400 ×). DAPI was used to demonstrate live cells. (a) Control RGC-5 cells in culture. (b) 10 mM glutamate plus 0.5 mM BSO treated RGC-5 cells in culture. (c-e) Pre-treatment of EECD (0.1 to 10 μg/mL concentration) with 10 mM glutamate plus 0.5 mM BSO. (f) Pre-treatment of NAC (1 mM concentration) with 10 mM glutamate plus 0.5 mM BSO. (g) Quantification of DHE fluorescence was analyzed with Leica Application Suite 2.02 software (Leica, Germany) using four representative fields from each well, and images of four wells were sampled per group (n = 16 in each group). Scale bar = 50 μm. The results are mean values with error bars indicating ± SEM (***) p < 0.001.

been recognized as a critical mediator in RGC death and glaucoma [7].

In view of the role of oxidative stress in retinal degeneration, we have shown that *C. denticulatum* ameliorates the effects of the production of reactive

Table 1. The Effect of EECD on Inhibition of Lipid Peroxidation Induced by Sodium Nitropruside (SNP) in Rat Forebrain Homogenates.

sample	Lipid peroxidation		
	Concentration (µg/ml)	Inhibition (%)	IC ₅₀ (µg/ml)
EECD	2.5	57.78±16.41	1.72
	1.25	42.93±13.84	
	0.625	33.19±10.59	
	0.3125	27.22±11.20	
EGCG	0.23	63.06±7.48	0.12
	0.115	48.72±7.66	
	0.0575	38.16±12.40	
	0.02875	27.53±12.67	

oxygen species (ROS) induced by H₂O₂, O₂^{•-}, or •OH (Figure 3). Moreover, the inhibitory effects of *C. denticulatum* on ROS were clearly confirmed by using dihydroethidium (DHE) staining, which directly measures intracellular O₂^{•-} (Figure 4).

Lipid peroxidation is the oxidative degeneration of lipids, and it has been shown that lipid peroxidation is implicated in glaucoma [8]. In our study, we have shown that treatment with *C. denticulatum* clearly inhibited lipid peroxidation in a concentration-dependent manner (Table 1). Thus, taken together, our results suggest that the neuroprotective effects of *C. denticulatum* *in vitro* occur through anti-apoptotic and anti-oxidative mechanisms.

SNP at a concentration of 20 µM caused a sub-maximum stimulation of TBARS in a previous study; therefore, this SNP concentration was used to determine the inhibitory effects in the samples. Different concentrations of EECD were pre-incubated with brain homogenates at 37°C for 5 min. SNP was then added at the concentrations indicated and the homogenates were incubated for a further 10 min. Results are means values ± SEM of three independent experiments.

Neuroprotective effects of *C. denticulatum* *in vivo*

To show whether *C. denticulatum* had neuroprotective

effects *in vivo*, we determined the changes in ganglion cell numbers and inner plexiform layer (IPL) thickness caused by the intravitreal injection of *N*-methyl-d-aspartate (NMDA) into rat retinas.

It was previously reported that NMDA administered in the eye of a rat caused cell death in the ganglion cell layer (GCL) and a reduction of IPL thickness, and that the blockade of excessive glutamate could be a possible strategy for the development of neuroprotective agents [9]. The present study showed that *C. denticulatum* attenuated the detrimental effects caused by NMDA (Figures 5 and 6).

Optic nerve crush (ONC) is a common experimental model of chronic glaucoma in which the optic nerve is surgically exposed and clamped for several seconds. There are several possible mechanisms for the degeneration of RGCs by ONC, including blockade of axonal transport resulting in inadequate supply of neurotrophic factors, disturbances of intracellular calcium homeostasis, activation of cell death genes, and local excitotoxicity due to uncontrolled activation of NMDA receptors [10]. Another mechanism of degeneration may be through ROS production, which causes the slow, chronic, and synchronous death of RGCs [11]. *C. denticulatum* significantly reduced the loss of RGCs caused by ONC (Figure 7).

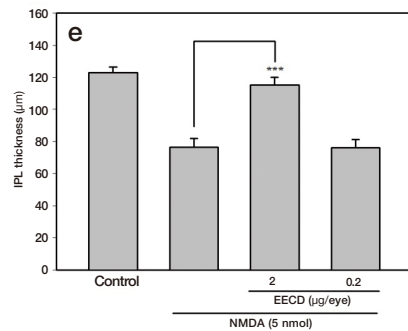
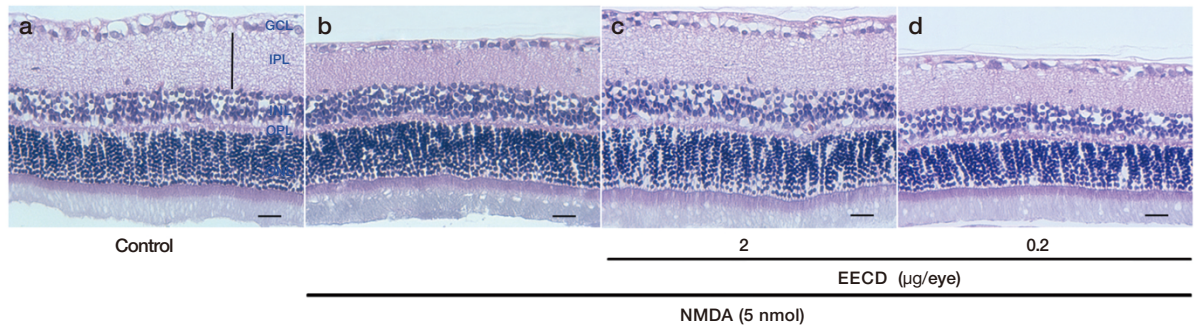


Figure 5. Effect of EECD on retinal damage induced by intravitreal injection of *N*-methyl-d-aspartate (NMDA) in rats. Representative photomicrographs showing the histologic appearance of retinal cross sections with hematoxylin and eosin staining at 7 days after treatment with or without NMDA. (a) Non-treated, (b) NMDA (5 nmol), (c) NMDA (5 nmol) plus EECD (2 µg/mL), (d) NMDA (5 nmol) plus EECD (0.2 µg/mL). Quantification of the thickness of the IPL is shown in (e). The scale bar represents 50 µm. Results are the mean values with error bars indicating ± SEM from six independent experiments (***p* < 0.001).

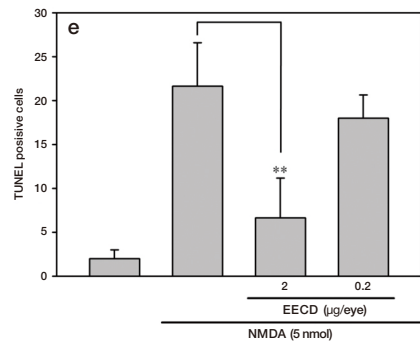
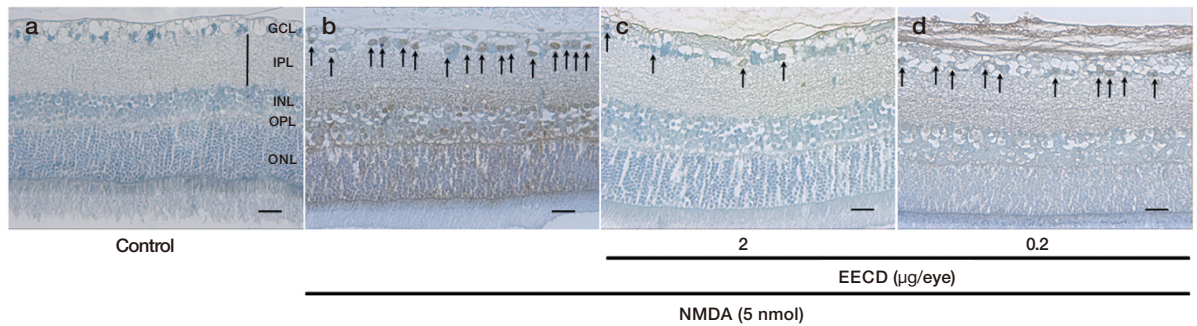


Figure 6. The anti-apoptotic effect of EECD demonstrated by a TUNEL assay. Representative photomicrographs showing the histologic appearance of retinal cross sections with TUNEL stain after 18 h with or without NMDA. Retinal damage was induced by an intravitreal injection of NMDA. (a) Non-treated, (b) NMDA (5 nmol), (c) NMDA (5 nmol) plus EECD (2 µg/mL), (d) NMDA (5 nmol) plus EECD (0.2 µg/mL). The arrows indicate TUNEL-positive cells (brown stain). Quantification of the TUNEL positive cells is shown in (e). The scale bar represents 50 µm.

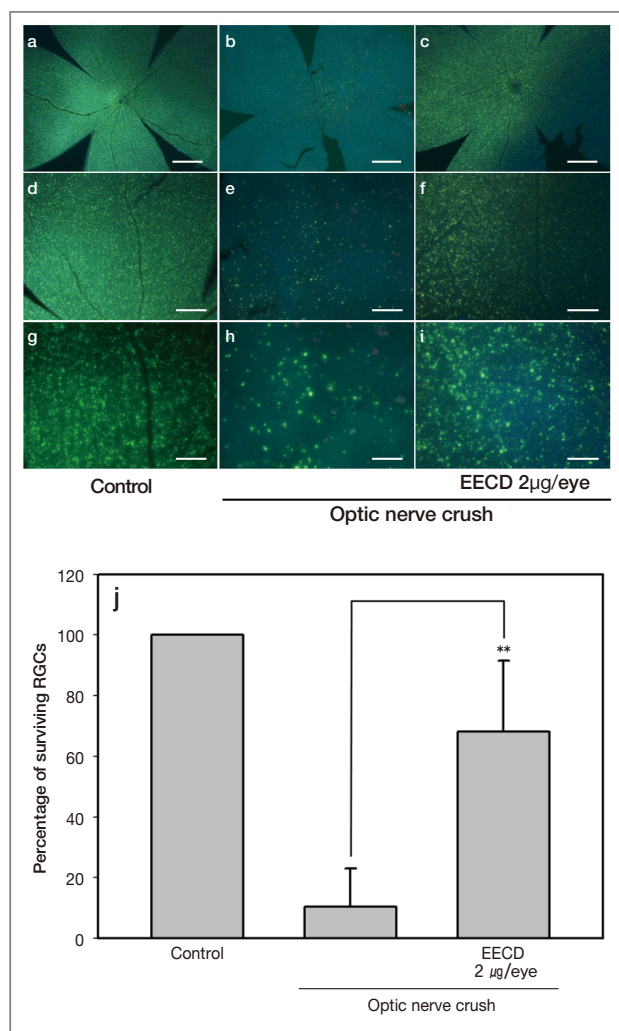


Figure 7. Fluorogold labeled RGCs in the mouse 1 week after optic nerve crush (ONC). Retrogradely labeled RGCs of mice with uninjured and injured optic nerves. RGCs were labeled by injecting 3% Fluorogold into the superior colliculi of the brain. The figure shows representative micrographs of normal retina (a) and damaged retina 1 week after ONC with (c) or without EECD (b). Scale bars in (a), (b), and (c) represent 500 μm. Low-magnification ($\times 100$) images of labeled RGCs in (a), (b), and (c) are shown in (d), (e), and (f). Scale bars in (d), (e), and (f) represent 100 μm. High magnification ($\times 200$) images of (a), (b), and (c) are shown in (g), (h), and (i). Scale bars in (g), (h), and (i) represent 50 μm. The results showed a significant increase in RGC survival after EECD treatment compared with vehicle treatment (j). Experimental values are expressed as percentage of surviving RGCs with error bars indicating \pm SEM from three independent experiments (** $p < 0.01$).

Major compound in *C. denticulatum* and its neuroprotective effects

Several compounds have been isolated from *Crepidiastrum* plants, including the sesquiterpene glucosides youngiaside A, youngiaside B and youngiaside C, and the hydroxycinnamic acids chlorogenic acid, 2,3-dicaffeoyltartaric acid (chicoric acid) and 3,5-dicaffeoylquinic acid (3,5-DCQA). Our HPLC results

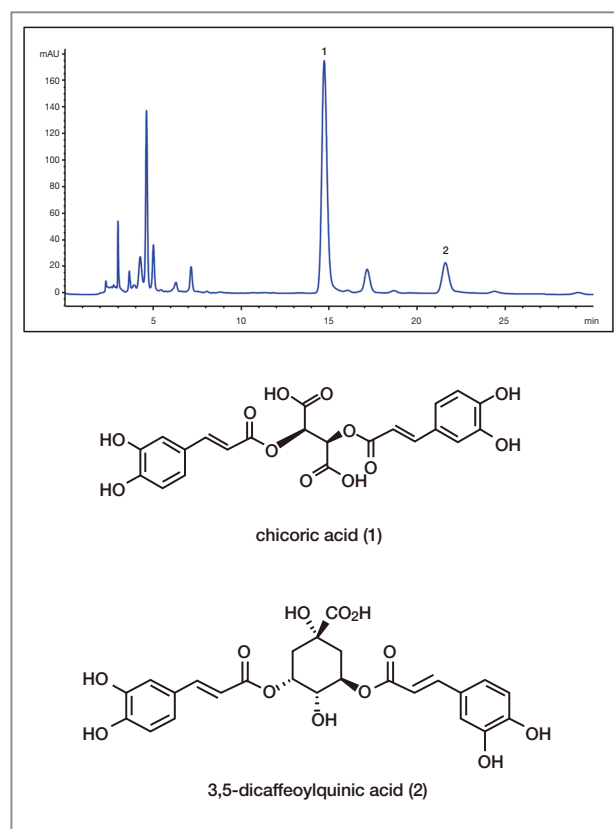


Figure 8. Chromatogram of the HPLC profile for EECD at 330 nm. Peaks: (1) chicoric acid, (2) 3,5-dicaffeoylquinic acid.

identified the major components in *C. denticulatum* as chicoric acid and 3,5-DCQA (Figure 8).

In our study, we proved that chicoric acid, the major phenolic compound of *C. denticulatum*, has protective effects both *in vitro* and *in vivo* (Figure 9), which suggests that chicoric acid may be the active compound in *C. denticulatum* providing protective effects for RGCs.

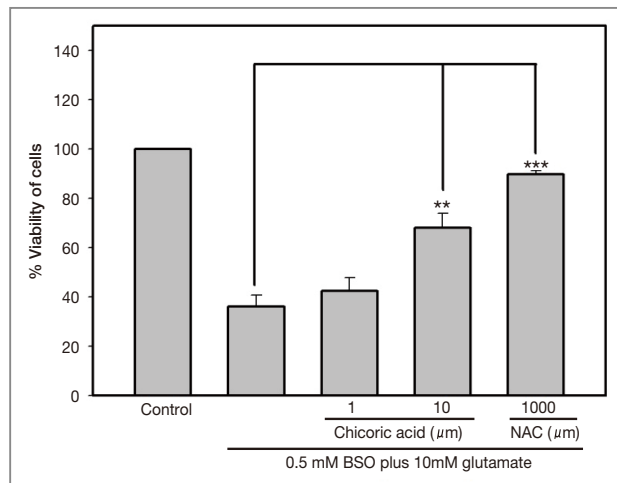


Figure 9A. Effect of chicoric acid on the viability of RGC-5 cells exposed to 10 mM glutamate plus 0.5 mM BSO for 24 h as measured by the MTT assay. 1 mM *N*-acetyl-L-cysteine (NAC) was used as a positive control. The results are mean values with error bars indicating \pm SEM where $n = 5$ independent experiments (** $p < 0.01$, *** $p < 0.001$).

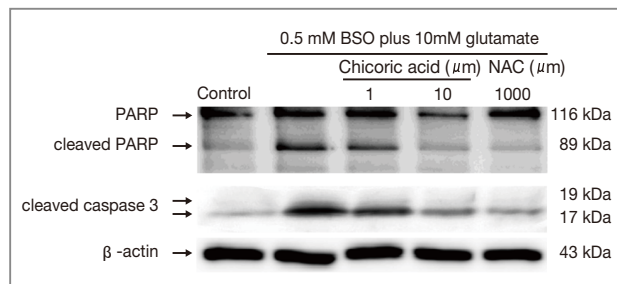


Figure 9B. Expression of apoptotic protein levels (PARP, cleaved caspase-3) in RGC-5 cells subjected to 10 mM glutamate plus 0.5 mM BSO with or without chicoric acid treatment. Protein level values are expressed as mean \pm SEM from three independent experiments.

This is the first report of the presence of chicoric acid in *C. denticulatum* and of its potential value in preventing retinal degeneration.

Closing remarks

Variations in food matrices and/or phenolic composition can have a major influence on intestinal bioavailability. Divergent results have been observed regarding the bioavailability of hydroxycinnamic acids

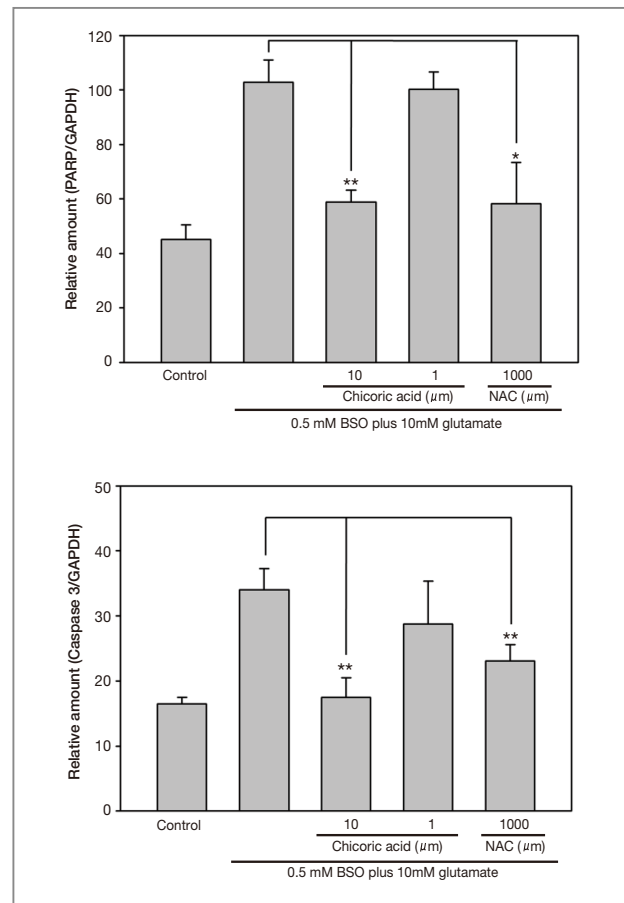


Figure 9C. Expression of mRNA level (PARP and caspase-3) in RGC-5 cells subjected to 10 mM glutamate plus 0.5 mM BSO with or without chicoric acid treatment. Values are expressed as mean \pm SEM from three independent experiments.

taken orally. Thus, further study will be needed regarding the bioavailability of chicoric acid with *C. denticulatum* as the food matrix. Our KIST intramural study is now focused on the bioavailability of food and ways to improve it.

Taken together, these findings support *C. denticulatum* as a potential bioactive wild vegetable that could be used as functional food for the prevention of neurodegenerative diseases such as glaucoma and age-related macular degeneration. Moreover, further research may show that chicoric acid isolated from *C. denticulatum* could be a candidate to serve as a marker compound for standardization in the development of functional food.

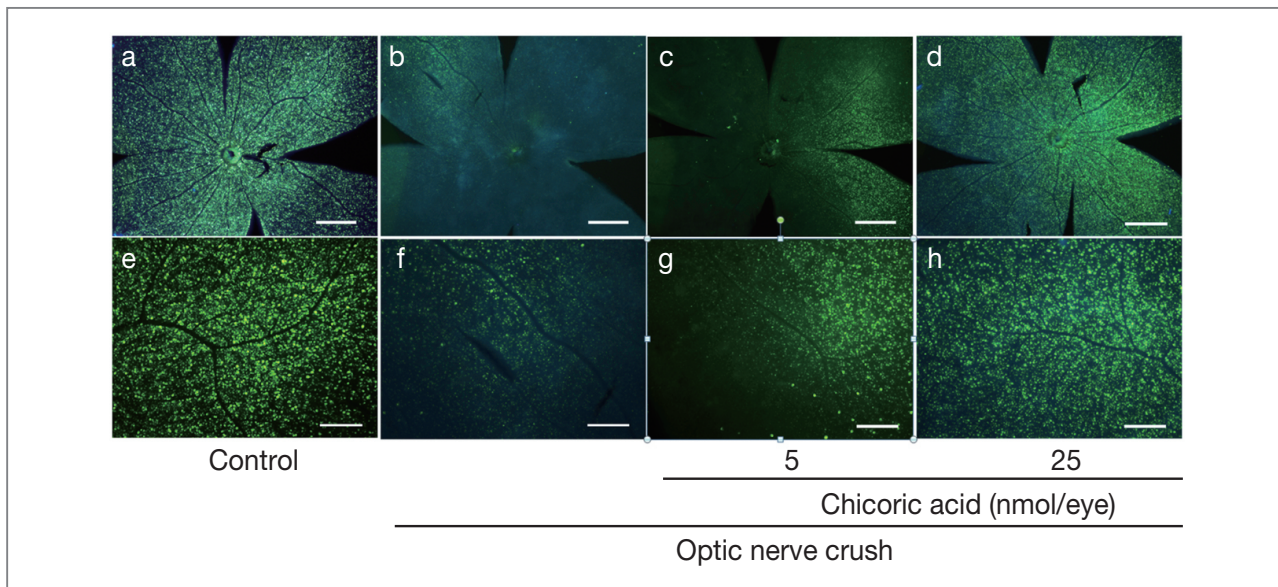


Figure 9D. Fluorogold labeled RGCs in the mouse 1 week after optic nerve crush (ONC). Retrogradely labeled RGCs of mice with uninjured and injured optic nerves. RGCs were labeled by injecting 3% Fluorogold into the superior colliculi of the brain. The figure shows representative micrographs of normal retina (a) and damaged retina 1 week after ONC with 5 nmol (c) and 25 nmol chicoric acid (d), or without chicoric acid (b). Scale bars in (a), (b), (c) and (d) represent 500 μ m. High magnification ($\times 100$) images of (a), (b), (c) and (d) are shown in (e), (f), (g) and (h). Scale bars in (e), (f), (g) and (h) represent 100 μ m.

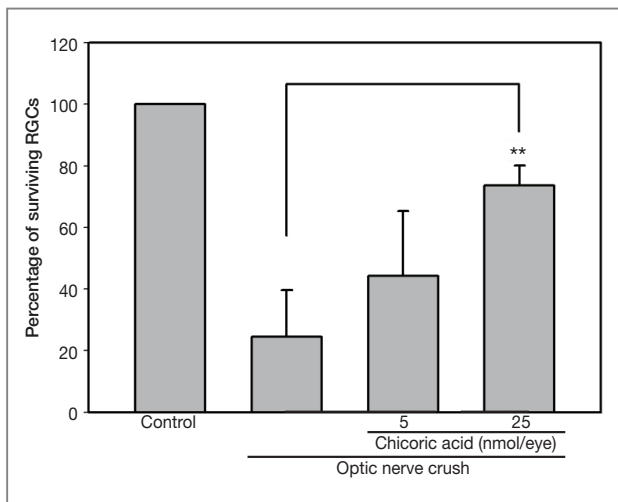


Figure 9E. The results showed a significant increase in RGC survival after chicoric acid treatment compared with vehicle treatment. Experimental values are expressed as percentage of surviving RGCs with error bars indicating \pm SEM from three independent experiments (** $p < 0.01$).

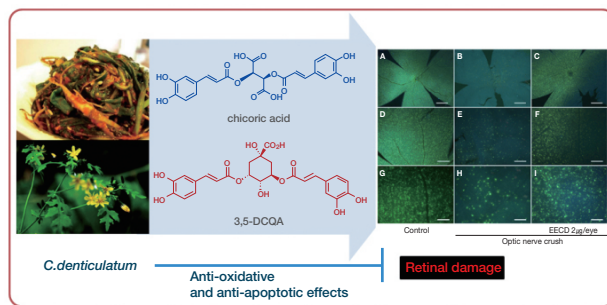


TABLE OF CONTENTS (TOC) GRAPHIC

Note

This article and images are drawn from “Hydroxycinnamic acids in *Crepidiastrum denticulatum* protect oxidative stress-induced retinal damage” in *J. Agric. Food Chem.*, Vol. 62 (6), pp. 1310~23.

References

- [1] Quigley HA. *Brit J Ophthalmol*. 1996; 80: 389-393.
- [2] Levin LA, Peeples P. *Am J Manag Care* 2008; 14: S11-14.
- [3] Kim JH, Kang SY, Kim NR, Lee ES, Hong S, Seong GJ, Hong YJ, Kim CY. *Korean J Ophthalmol*. 2011; 25: 110-115.
- [4] Levkovitch-Verbin H, Martin KR, Quigley HA, Baumrind LA, Pease ME, Valenta D. *J Glaucoma* 2002; 11: 396-405.
- [5] Akihisa T, Franzblau SG, Ukiya M, Okuda H, Zhang F, Yasukawa K, Suzuki T, Kimura Y. *Biol Pharm Bull*. 2005; 28: 158-160.
- [6] Kim KA, Shim SH, Ahn HR, Jung SH. *Toxicol Appl Pharmacol*. 2013; 269: 109-120.
- [7] Galaris D, Pantopoulos K. *Crit Rev Clin Lab Sci*. 2008; 45: 1-23.
- [8] Aslan M, Cort A, Yucel I. *Free Rad Biol Med*. 2008; 45: 367-376.
- [9] (a) Joo CK, Choi JS, Ko HW, Park KY, Sohn S, Chun MH, Oh YJ, Gwag BJ. *Invest Ophthalmol Vis Sci*. 1999; 40: 713-720. (b) Brandstatter JH, Hartveit E, Sassoe-Pognetto M, Wassle H. *Eur J Neurosci*. 1994; 6: 1100-1112. (c) Mizuno K, Koide T, Yoshimura M, Araie M. *Invest Ophthalmol Vis Sci*. 2001; 42: 688-694.
- [10] (a) Kreutz MR, Seidenbecher CI, Sabel BA. *Restor Neurol Neuros*. 1999; 14: 127-134. (b) Schuettauf F, Rejdak R, Thaler S, Bolz S, Lehaci C, Mankowska A, Zarnowski T, Junemann A, Zagorski Z, Zrenner E, Grieb P. *Exp Eye Res*. 2006; 83: 1128-1134.
- [11] Steinsapir KD, Goldberg RA. *Surv Ophthalmol*. 1994; 38: 487-518.



Eye Research Laboratory/Functional Food Center

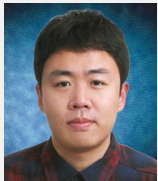
[Technical Review]

State-of-the-Art Technology for Improving the Performance and Stability of High Performance Computers



Samuel Boateng

Computational
Science Center
boatengsamuel@
gmail.com



Haneol Cho

Computational
Science Center
h12004@kist.re.kr



Kyu Hwan Lee

Computational
Science Center
biometal@kist.re.kr

Introduction

It is undeniable that computers are indispensable to the modern world. But just a few decades ago predictions about the future development and possible impact of computer systems technology were often laughably wide of the mark. Here are two examples:

- “Computers in the future may weigh no more than 1.5 tons.” *Popular Mechanics*, forecasting the relentless march of science, 1949.
- “There is no reason anyone would want a computer in their home.” Ken Olson, president, chairman and founder of Digital Equipment Corp., 1977 [1].

Over time, the contributions of computing power to scientific research, discovery and innovation continued to grow. With an eye toward these developments, KIST’s Computational Science Center (CSC) has been focusing on two main avenues of research. One is to improve computing power and utility for science research. The other is to develop a management solution for increasing the stability of high performance computers (HPCs, commonly referred to as supercomputers). In this article, we review the cutting edge of HPC technology in two aspects, performance and stability.

International partnerships

The HPC Infrastructure Lab within the CSC has acted primarily as a computational resource manager and provider for various users in the computational science field. In order to be up-to-date on cutting-edge software and hardware technology, we are relying not only on our own research but also on international cooperation. For example, we participated as a computing resource provider in the MMM@HPC (Multiscale Materials Modelling on High Performance Computer Architectures) project under the European Union's 7th Framework Programme (FP7). Project goals of the MMM@HPC project were to:

- develop e-infrastructure for multiscale materials modelling,
- integrate software modules into customizable, high-performance protocols and workflows,
- unite expert groups with computational resource providers,
- address emerging computing needs with very efficient, evolving research tools,

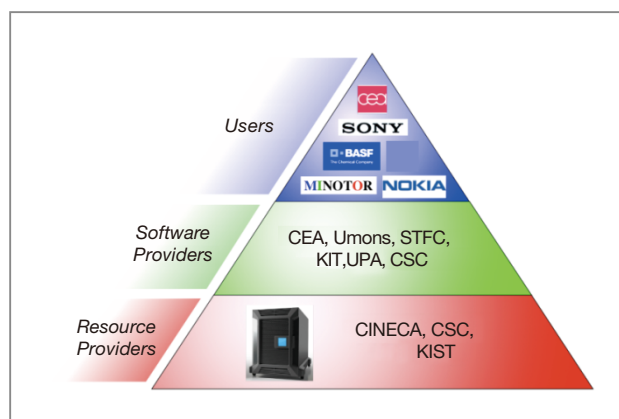


Figure 1. For the MMM@HPC project, KIST partnered with Italy's CINECA supercomputing center and Finland's CSC – IT Center for Science as computing resource providers. Software providers included, in addition to CSC, Germany's Karlsruhe Institute of Technology (KIT), France's Commissariat à l'énergie atomique (CEA), the United Kingdom's Science and Technology Facilities Council (STFC), the University of Mons (Umons) in Belgium, and the University of Patras (UPA) in Greece.

Source: <https://www.multiscale-modelling.eu/cms/upload/content/overview/grafik2.png> [2].

- provide the European research community a leading-edge software infrastructure,
- strengthen Europe's international role as a software provider, and
- demonstrate a direct impact towards solving visible European R&D challenges.

In addition, we are undertaking joint research with Peruvian scientists on a Hadoop (Big Data)-based Plant Information Retrieval System using hybrid HPC technology to support Peru's Amazon region biodiversity conservation project. The main goals of the project are to:

- develop a structure for a data server (a small Big Data server),
- explore and develop Pattern Recognition Algorithms, and
- create an information retrieval System.

Development of high performance computing

Computer software is typically written for serial computation. To solve a single problem, an algorithm is developed and executed in sequence as a stream of instructions. These instructions or commands are carried out on a single Central Processing Unit (CPU). Only one instruction may be executed at a time—after the CPU completes one instruction, the following one is executed.

The situation where multiple processing elements are used simultaneously to solve a single problem is known as parallel computing. The algorithm of parallel computing is developed such that it breaks down the problem into smaller independent parts; each of the processing elements is then assigned a part of the problem and executes it simultaneously with the others. The processing elements could be a single computer with multiple processors (multi-core processors), several networked computers, specialized hardware or any feasible combination of the above [3].

Parallelism (the high end of computing) has been employed for many years, mainly in high performance

computing, due to the many limitations of serial computing (large physical size of transistors, limited memory size and speed, limited instruction-level parallelism, high power usage and excessive heat), the unending pursuit of realism in computational sciences, and environmental sustainability. The many advantages of parallelism include the time saved, solution of larger and more complex problems, access to more memory, better memory performance (when programmed correctly), concurrency, high stability and cost savings.

The rapid growth in computationally-intensive tasks exemplified by increasingly sophisticated mathematical models, with their longer computation times, larger memory requirements and need to analyze large volumes of data, has increased the reliance on and continuous interest in parallel computing in various fields, including quantum mechanics, bioinformatics, medical imaging, computational finance, weather forecasting, climate research, oil and gas exploration, molecular modeling and physical simulations.

Parallelism has caused the computational capabilities

and performance of computer systems to increase exponentially in the last two decades, from a few hundred FLOPS (**F**loating-point **O**perations **P**er **S**econd) to several quadrillion FLOPS (petaFLOPS or 1^{15} FLOPS). Currently a single processor board is able to achieve 1 teraFLOPS (1 trillion or 1^{12} FLOPS) of computations. **Figure 2** below shows the rapid advancement in processor technology and architecture in the last few years.

Figure 3 presents a comparison of three different kinds of processors being used for high performance computing. The Intel Xeon Phi 7120X has a memory of up to 16GB GDDR5 (Graphics Double Data Rate, version 5) per coprocessor, which is bigger than the 6GB GDDR5 of both the TESLA K20 and FirePro S9000. The Xeon Phi 7120X also has a bigger memory bandwidth of 320GB/s per coprocessor, as compared to 200GB/s for the TESLA K20 and 264GB/s for the FirePro S9000. For double-precision performance per coprocessor, the Xeon Phi 7120X has 1.20TFLOPS, which is better than the 1.17TFLOPS of the TESLA K20 and 0.86TFLOPS of the FirePro S9000.

	1996 ASCI RED	2014 Intel Xeon Phi
		
Performance	1.3TFLOPS	1.20TFLOPS
CPU	10,000 cpus	61 cores
Power consumption	850kW	0.3kW
Price	\$55,000,000	\$4129

Figure 2. Comparison of the ASCI RED supercomputer and the Intel Xeon Phi, demonstrating the advancement in processor technology and architecture. Sources:

<http://www.adaptivecomputing.com/wp-content/uploads/2013/09/ASCI-red.jpg> [4]

<http://i.pcworld.fr/1255075-intel-xeon-phi-carte-calcul-gpgpu-x86-en-action.jpg> [5]

Functionality	TESLA K20	FirePro S9000	XEON Phi 7120X
GPU-Processor count	1	1	1
Cores	2496	1792	61
Architecture	Kepler GK110	Graphics Core Next	X87 Knights Corner
Memory per GPU-processor	6GB GDDR5 (5 GB w/ ECC)	6GB GdDDR5 (5 GB w/ ECC)	up to 16 GB GDDR5. ECC
Memory bandwidth per GPU-processor	200 GB/s	264 GB/s	320 GB/s
Performance (single precision, per GPU-proc.)	3.52 TFLOPS	3.230 TFLOPS	2.40 TFLOPS
Performance (double precision, per GPU-proc.)	1.17 TFLOPS	0.806 TFLOPS	1.20 TFLOPS
Max power usage per GPU-processor	225 Watt	225 Watt	300 Watt
Greenness (SP)	15.6 GFLOPS/Watt	14.35 GFLOPS/Watt	8 GFLOPS/Watt
Bus Interface	PCIe 3.0x16	PCIe 3.0x16	PCIe 3.0x16
Price (per GPU-processor)	\$3199	\$2500	\$4129
Price per GFLOPS (SP)	\$0.77	\$0.77	\$0.58
Price per GFLOPS (DP)	@2.73	\$3.10	\$0.29
Cooling	Passive	Passive	Passive (P,A=Active)

Figure 3. Comparison of three kinds of multiprocessors for high performance computing. Sources: <http://streamcomputing.eu/blog/2012-11-12/intel-answer-to-amd-and-nvidia-the-xeon-phi-5110p/>; http://ark.intel.com/ko/products/75800/Intel-Xeon-Phi-Coprocessor-7120X-16GB-1_238-GHz-61-core [6, 7].

The increase in computing power is caused not only by improving processors, but also by innovation in computer architecture. Processor architecture has

evolved from the scalar processor, advancing to the vector processor, cluster structure, and more recently to state-of-the-art hybrid architecture. With this success in

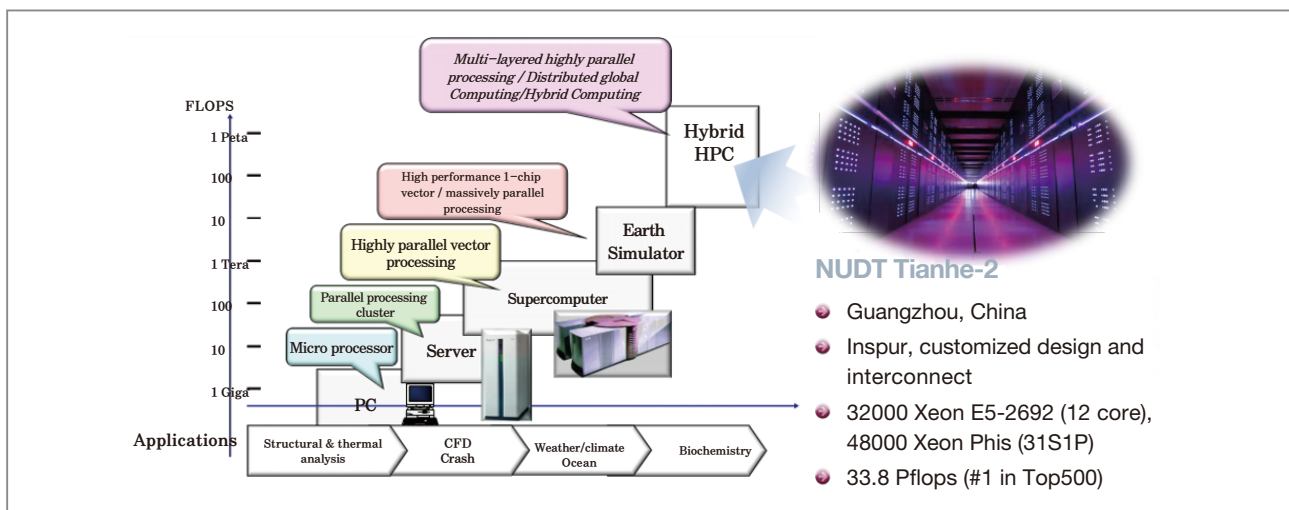


Figure 4. Advancement in HPC technology.

Sources: <http://www.thenewstrack.com/wp-content/uploads/2013/11/Tianhe-2.jpg>; <http://www.netlib.org/utk/people/JackDongarra/PAPERS/tianhe-2-dongarra-report.pdf> [8, 9].

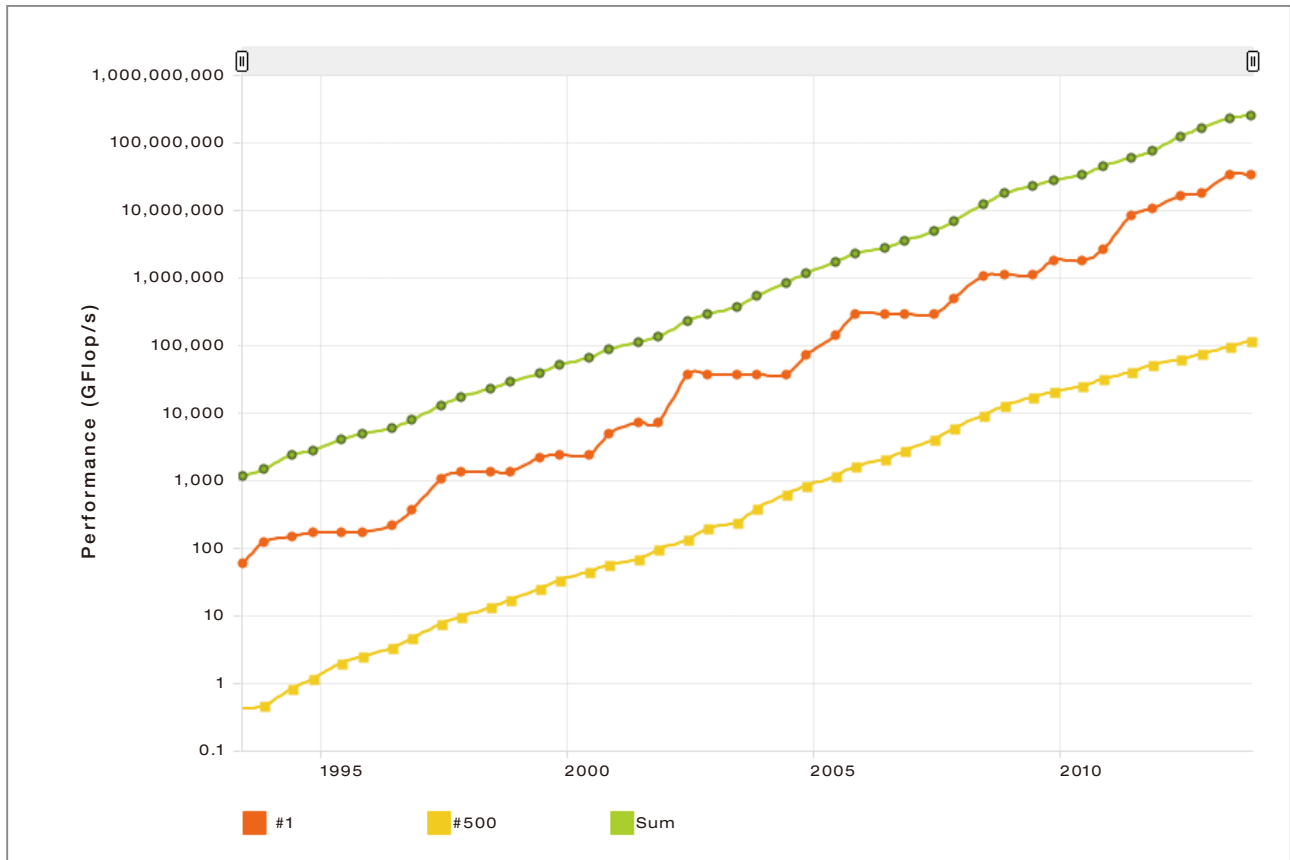


Figure 5. Performance of top 500 computers from 1993 to 2013.

Source: <http://www.top500.org/statistics/perfdevel/> [10].

computer architecture innovation, scientists and engineers can now build high performance computers that meet their requirements. Desktop computers can be turned into high performing computers when they are equipped with multi-core or many-core processor boards.

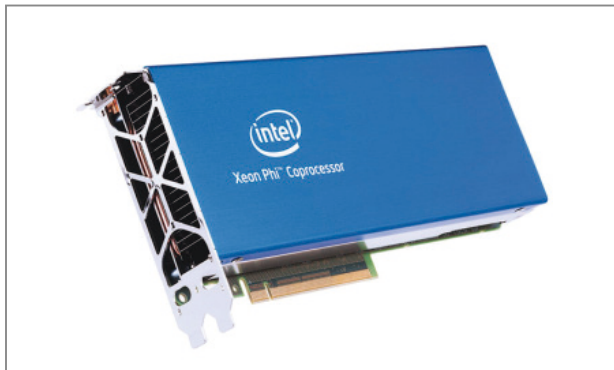


Figure 6a. MIC (Xeon Phi coprocessor).

The TOP500 project (top500.org) ranks, details and publishes the 500 most powerful computer systems in the world every June and November. The graph below shows the performance of the 1st and the 500th most powerful computer systems between 1993 and 2013.



Figure 6b. Tesla (GPU Processor).

The red line represents the 1st or most powerful computer in a particular year, the yellow line is for the 500th most powerful computer and the green line represents the sum of the FLOPS of all of the top 500 computers.

MIC hardware review

Two main architectures--the NVidia GPU (Graphics Processing Unit) and the Intel MIC (Many Integrated Core)--have been in the lead in driving innovation and extreme performance in processors that are used in revolutionizing HPCs.

Both the GPU and MIC are parallel coprocessors. A developer uses the same three methods to program



Figure 7. The KIST Grand HPC with MIC and the GPU Tesla Cluster.

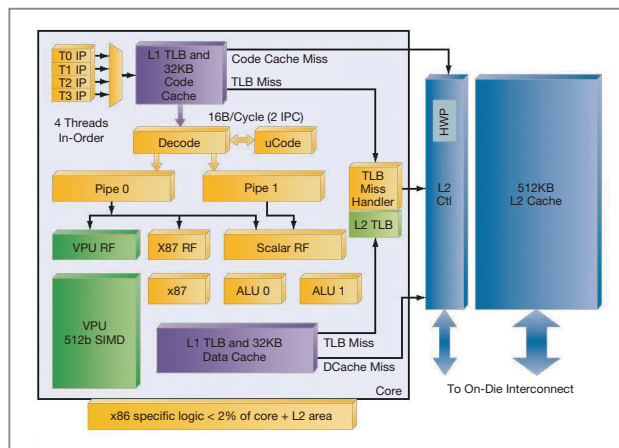


Figure 8. Architecture of the CPU in the Xeon Phi coprocessor (each CPU can carry out 4 threads and has one 512KB cache per node). Source: http://pc.watch.impress.co.jp/docs/column/kaigai/20120911_558738.html [13].

Specifications of the GPU Tesla Hybrid Cluster

PCI Express Gen 2. X 16 slot (X 8)

16 lane slots (each direction):

v1.x: 4 GB/s (32 Gbit/s)

v2.x: 8 GB/s (64 Gbit/s)

v3.0: 16 GB/s (128 Gbit/s)

CPU: Intel Xeon E5620 4Core 2.4GHz (X 2)

RAM: DDR3 4G (X 8)

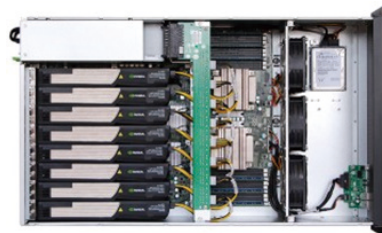
Storage: SATA2 1TB (X 2)

Total Cores: 4 Cores x 2 CPU = 8 Cores

GPU: 8 Tesla Fermi C2050 Graphic Processors available

In the test-bed, a 6 x C2050 Processor is used for power-stability

6x448 CUDA Cores=2688 cores



The 8 GPU boards of the GPU Cluster

Specifications for the MIC Hybrid cluster

32 Node sets (MIC)

- 2 CPUs (Xeon E5-2665 ; 8 cores per CPU) ,
- 16 x 32 nodes = 512 (HT 1024) cores
- MIC Card 60 x 32 nodes = 1920 (HT7680) cores
- 128GB memory per node

Mellanox InfiniBand 40G 1 port & 10G 2 ports

Storage node 1 set (90TB / Raid 6)

Server Backup Battery Pack for Substituting UPS

InfiniBand Switch 1 set

Gigabit/10G Switch 1 set

accelerators and optimize for performance – libraries, directives and native programming models like CUDA C for GPU or vector intrinsic on Xeon Phi.

KIST has both a GPU Tesla Hybrid Cluster, which was built for the Multiscale Materials Modelling on High Performance Computer Architectures (MMM@HPC) project, and a Grand HPC, which is also a hybrid HPC built with Intel Xeon Phi (MIC) coprocessors. The fundamental differences between the MIC (Xeon Phi) and

Table 1. The three methods used to program both the GPU and the MIC (Xeon Phi).
Source: <http://www.nvidia.com/object/justthefacts.html#sthash.uM6Yzkjz.dpuf> [11].

Method	GPU	Phi
Libraries	√ CUDA Libraries+others	√ Intel MKL+others
Directives	√ OpenACC	√ OpenMP+Phi Directives
Native Programming Models	√ CUDA	√ Vector Intrinsics

Table 2. Fundamental differences between GPU and MIC (Xeon Phi).
Source: <http://indico.cern.ch/event/184092/contribution/5/material/slides/0.pdf> [12].

	GPU	MIC / KNC
Architecture	Proprietary	x86
Language	Limited to vendor API Derived	Standard C, C++, Fortran
Programmability	Limited to vendor API	Mainstream techs
Xeon optimization payoff	No	Yes
Direct access	No	Yes
IEEE 754 compliance	Evolving	Standard
SSE compatibility	No	Yes
Binary FP compat. w/ Xeon	No	?



Figure 9a. The Tianhe-2.
Source: <http://www.d1net.com/server/news/249304.html> [14]

GPU are shown in Table 2.

The MIC, launched in the second half of 2013, is already being used in the most powerful computer in the world, the Tianhe-2 (天河2, Figure 9a). Its performance is up to 33.86 petaFLOPS and it has 2~5 MIC boards in each node.

Performance of the MIC can be up to 1.2TFLOPS. A



Figure 9b. The Xeon Phi coprocessors.
Source: <http://victorna.blogspot.kr/2013/07/tianhe-2milky-way-2.html> [15]

MIC board has 16GB GDDR5 memory, which has a much better access speed (352GB/s) than DDR3 memory. Although 16GB is smaller than the memory of the host computer, the size is reasonable because it has much better access latency and is for acceleration only. For

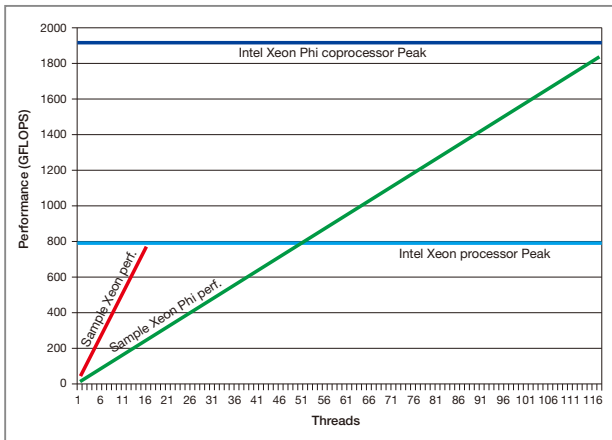


Figure 10. The performance of Xeon Phi coprocessor. (This coprocessor has inferior performance per CPU but greater peak performance because of lower network overhead.)

Source: <http://www.greymatter.com/corporate/showcase/intel/xeon-phi/> [16].

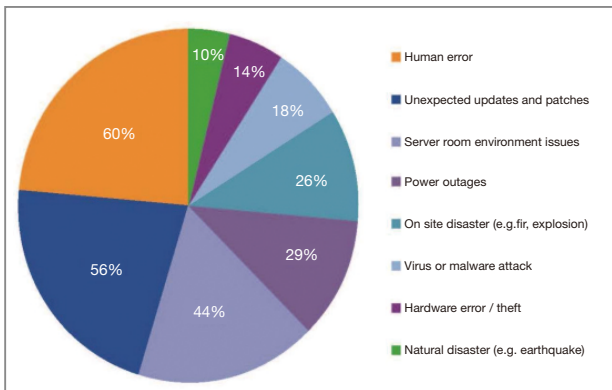


Figure 11. Cause ratios of system down-time.

Source: http://eu.acronisinfo.com/files/2012/01/DR_Index_2012_EU_EN_120127.pdf [18].

this reason, algorithms or codes for MIC have to be well arranged in the memory stack so the stack does not go beyond 16GB.

Business continuity and disaster recovery

All computer systems are at risk from various kinds of disasters, both natural and man-made. Even though

nature poses the highest risk of dramatic disasters that can befall an organization, human error is still the number one cause of system failure and business down-time. Other causes of system failure are low-profile factors such as hardware failures, data loss, power and network outages, security breaches and application failures. These factors must be addressed by having a comprehensive Disaster Recovery (DR) plan because failure or inability to recover immediately from system failure can damage an organization's long-term performance and reputation as much as a natural disaster or malicious attack [17].

The KIST HPC management solution

There are several commercial disaster recovery solutions currently available, ranging from tape backups, disk mirroring, and disk backup, to highly available automated DR, data replication, virtualization and cloud applications that meet the needs of both small and large businesses.

A highly available system has the ability to remain accessible and functional in the event of a component failure. High availability (HA) is realized by building in multiple levels of fault tolerance and/or load balancing capabilities into a system [20].

HA systems can be set up to immediately take over another machine in case of a problem with little downtime and no loss of data. In most cases, the takeover is automated. Because of the high cost involved in providing HA systems, few organizations (only 21%) are able to implement them.

Tape and disk backup are the more traditional, widely-used and affordable methods of data protection (included in about 79% of existing DR solutions). Contents of operational disks are periodically copied onto tape or disk media and stored at a remote site. The entire content of the disk, or a designated amount (usually referred to as incremental backup), can be transferred. Both tape and

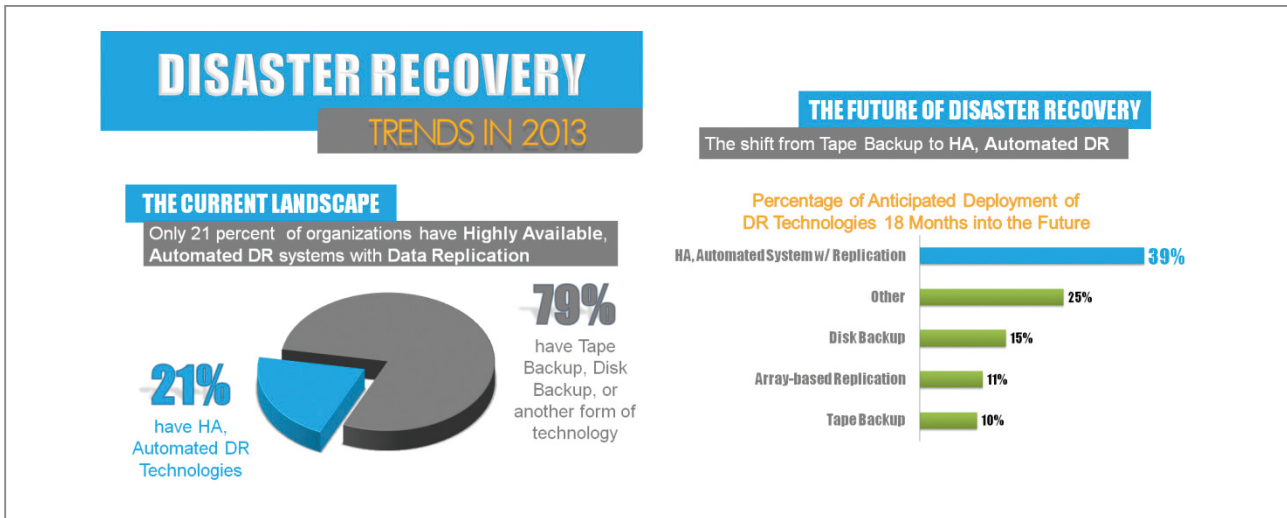


Figure 12. Trends in disaster recovery solutions.
Source: <http://www.falconstor.com/infographics/2013-disaster-recovery-trends-infographic> [19].

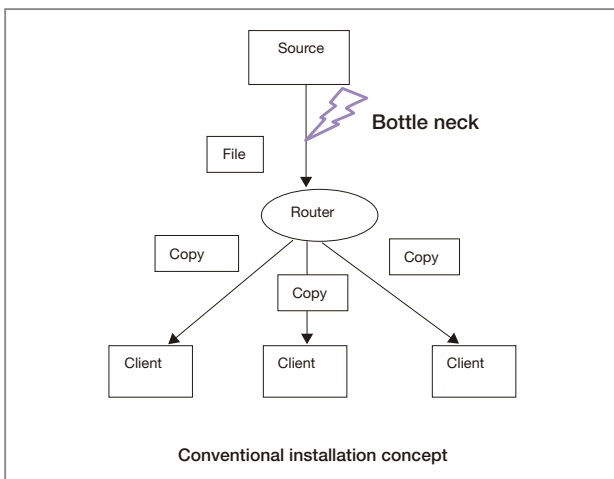


Figure 13. Multicast network.

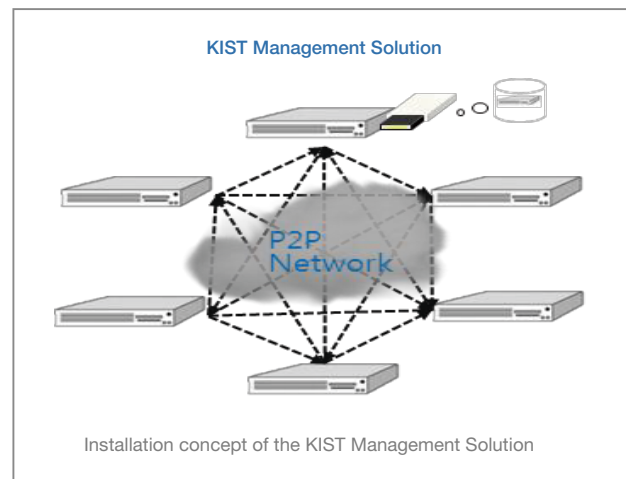


Figure 14. Peer-to-peer network.

disk backup can be automated to ensure reliability and less human intervention.

The KIST HPC management solution is the first DR solution that is based completely on open-source software, has up-to-date kernel support and is designed for disaster recovery and for quick OS and application deployment. Unlike conventional rsync and multicast methods of installation (Figure 13), the KIST solution uses the peer-to-peer (P2P) mechanism for ultrafast OS deployment and recovery (Figure 14). P2P is a

decentralized and distributed network design in which individual nodes in the network (called “peers”) act as both providers and users of resources [21]. In rsync and multicast only a fraction of the bandwidth is available to the nodes, but in the P2P mechanism employed by KIST all nodes use the full bandwidth as a peer for deployment.

Rsync, multicast, and BitTorrent are the three main protocols that are used for OS deployment in SystemImager (software that automates Linux installs, software distribution, and production deployment) [22].

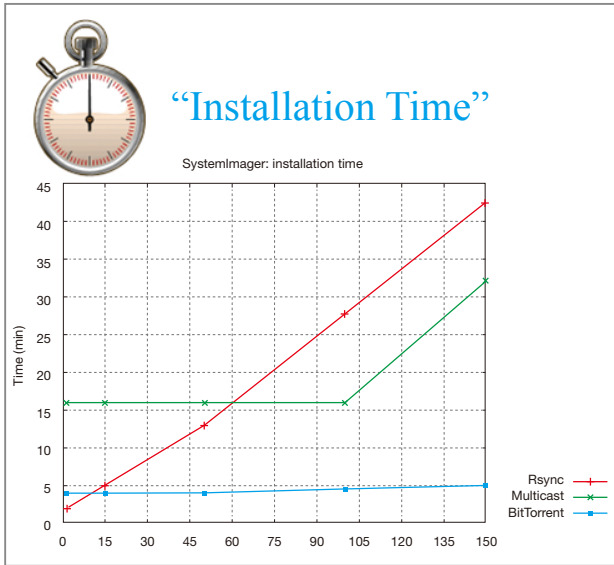


Figure 15. Installation time for rsync, multicast and BitTorrent.
Source: <http://download.systemimager.org/pub/docs/SystemImager-LinuxTag-2007-paper.pdf> [23].

Figure 15 shows a comparison of the installation time of the three protocols of SystemImager.

The main features of the KIST HPC management solution, as compared to open-source SystemImager, are shown in Table 3 below.

The management solution includes a hardware component consisting of a USB disk, a solid state drive (SSD) or an external hard disk with a pre-configured, ready-to-install operating system.

The speed of OS and application deployment of the KIST solution depends largely on the hardware and

network speed. For example, on a 10Gbps network it takes only four minutes to finish the OS and application deployment, while it takes up to 16 minutes to finish on a 100 Mbps network.

The KIST HPC management solution offers five advantages.

- It can be used for workstation/desktop and cluster operating systems (Linux and Windows) recovery only. This is particularly useful if the disaster affected only the operating system.
- It can be used for workstation/desktop and cluster operating systems and critical applications recovery. Critical business applications can be pre-installed on the management solution to speed up recovery where the applications are affected.



Figure 16. The KIST HPC management solution, USB flash drive type (64GB) and USB SSD type (128/256GB).

Table 3. Comparison between SystemImager and the KIST management solution.

	Open source SystemImager (Argonne National Lab)	KIST HPC Management Solution
Method	OS deployment with P2P	OS deployment and restore with P2P
Developing Status	Stopped in 2007	Ongoing
Hardware Support	Does not support UUID	Supports UDEV
File System	Only for old Linux file system. Does not support recent file systems (ext4, xfs) or raid.	Recent Linux file systems (ext4, xfs), raid file systems and various other OS file systems available with virtualization.
Target	Redhat family (Up to Centos 5.x) Does not support Debian family	Not only for Linux family; most OS available.
Virtualization	Not Supported	Server and Desktop Level, VDI (Virtual Desktop Infrastructure)

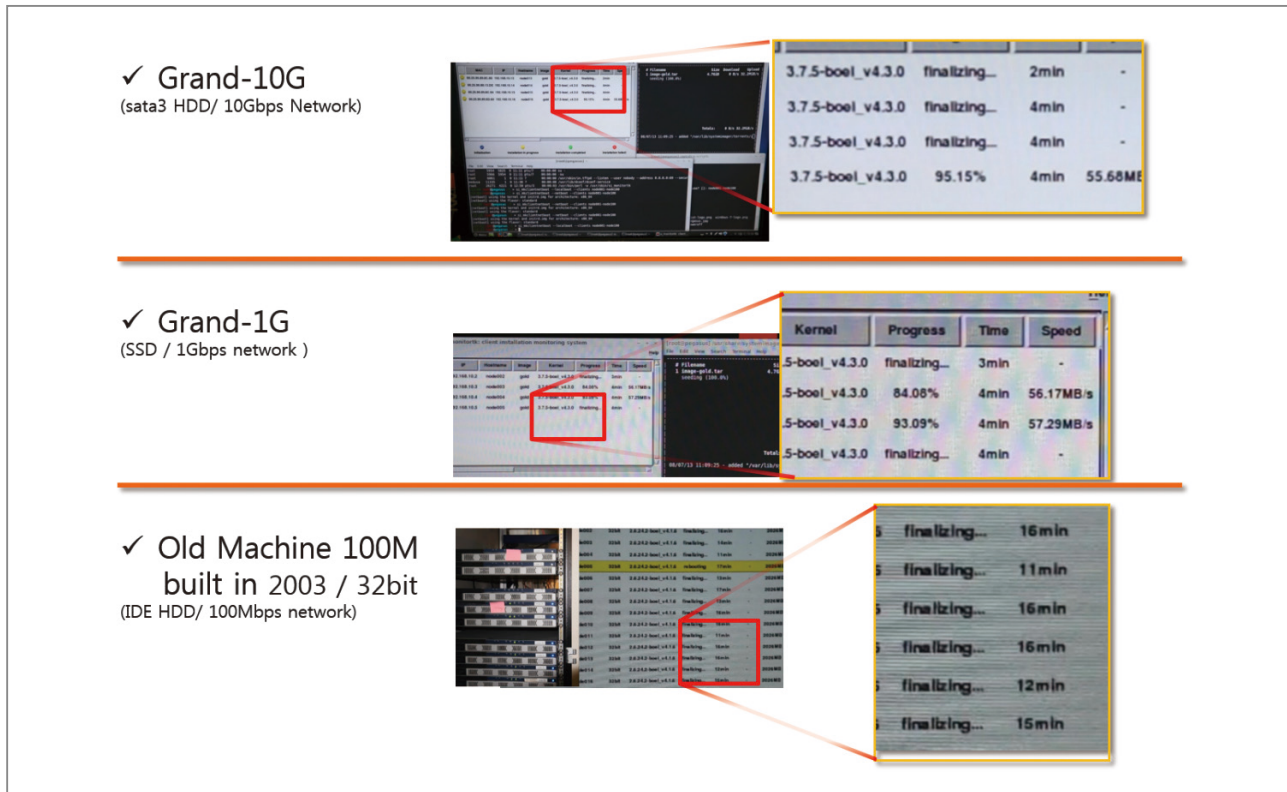


Figure 17. Time required to deploy depends on H/W and network speed.

- It can easily be integrated into an existing DR solution/ system or as part of a new DR plan to handle the critical operating system and applications recovery stage. This will significantly reduce the recovery time because of its ultra-fast speed.
- One very important stage of disaster recovery is the restoration of system data. If critical business applications are pre-installed on the KIST management solution, it can be set up as a backup system at a remote site so that critical data for the various applications can be backed up at regular intervals and stored. This will in turn significantly reduce the recovery time in a situation where data, applications and the operating system have to be restored.
- It can separate computer networks into two (for example, Internet and Intranet) without diminishing computational resources. This is called “logical networks separation.”

Conclusion

Above, we reviewed cutting-edge technologies that affect two important aspects of HPC, performance and reliability. Hybrid HPC architecture and computational science capabilities have been made more versatile, wider and richer by the innovation and introduction of MIC and GPUs. The sustained performance and reliability of HPCs is very important and must be ensured at all times by the use of cutting-edge technologies because their role and impact on industry and academia is growing every day.

KIST has offered its supercomputing platform to both KIST researchers and international academia for the enhancement of research and development. Several organizations are also using the KIST Grand HPC for various purposes.

The HPC Infrastructure Lab will build a working virtual simulation fab (fabrication facility) for nano- and bio-

materials modelling that will run on the Grand HPC. This virtual simulation fab will be made available to both local and international academia and related organizations for research and instruction. The virtual fab will provide scientists with a realistic experience of the fabrication process through a virtual interface.

We are currently improving on the technology and knowhow that we used to develop the HPC management system. When that process is complete, we will have an advanced DR technology ready for transfer to Korean industry players who might be interested.

References

- [1] Eric A. and Kathryn S. Meyer. Vision and Perseverance! Retrieved from: <http://meyerweb.com/other/humor/vision.html>
- [2] MMM@HPC. Project partners of the EU Framework MMM@HPC project <https://www.multiscale-modelling.eu/cms/upload/content/overview/grafik2.png>
- [3] Wikipedia. Background, parallel computing. Retrieved from: http://en.wikipedia.org/wiki/Parallel_computing
- [4] Adaptive Computing. Picture of ASCII. Retrieved from: <http://www.adaptivecomputing.com/wp-content/uploads/2013/09/ASCII-red.jpg>
- [5] PCWorld.fr. Picture of Intel Xeon Phi Retrieved from: <http://i.pcworld.fr/1255075-intel-xeon-phi-carte-calcul-gpgpu-x86-en-action.jpg>
- [6] Mr. Vincent Hindriksen M.Sc. Performance comparison of Tesla K20, FirePro S9000 and Intel Xeon Phi. Retrieved from: <http://streamcomputing.eu/blog/2012-11-12/intels-answer-to-amd-and-nvidia-the-xeon-phi-5110p/>
- [7] ©Intel Corporation. SPECIFICATIONS of Intel® Xeon Phi™ Coprocessor 7120X (16GB, 1.238 GHz, 61 core). Retrieved from: http://ark.intel.com/ko/products/75800/Intel-Xeon-Phi-Coprocessor-7120X-16GB-1_238-GHz-61-core
- [8] The New Strack™. Chinese Supercomputer Tianhe 2 Twice As Fast American Titan. Retrieved from: <http://www.thenewstrack.com/wp-content/uploads/2013/11/Tianhe-2.jpg>
- [9] Jack Dongarra, University of Tennessee Oak Ridge National Laboratory. Summary of the Tianhe-2 (TH-2) Milkyway-2, in Visit to the National University for Defense Technology Changsha, China. June 3, 2013. Retrieved from: <http://www.netlib.org/utk/people/JackDongarra/PAPERS/tianhe-2-dongarra-report.pdf>
- [10] Top500. Performance Development [Graph illustration the Performance Development form 1993 to 2013]. Retrieved from: <http://www.top500.org/statistics/perfdevel/>
- [11] ©2014 NVIDIA Corporation. Developers use libraries, directives, or native programming models to program accelerators and optimize for performance (Data from August 2013). Retrieved from: <http://www.nvidia.com/object/justthefacts.html#sthash.uM6Yzkjz.dpuf>
- [12] Andrzej Nowak, CERN openlab. An overview of Intel MIC - technology, hardware and software (April 25th 2012). Retrieved from: <http://indico.cern.ch/event/184092/contribution/5/material/slides/0.pdf>
- [13] PC Watch. Internal block of core. [Block diagram of Internal Block of Core] Retrieved from: http://pc.watch.impress.co.jp/docs/column/kaigai/20120911_558738.html
- [14] D1net. 喜忧参半 2013服务器市场热点分析(Mixed hot market analysis server 2013), 国产编译器厂商跃入主流行列(Picture of Milky Way II). Retrieved from: <http://www.d1net.com/server/news/249304.html>
- [15] Blog, 빅터의 IT 이야기. 계산 블레이드에 장착된 제온 파이 코프로세서, Tianhe-2(Milky Way-2) 슈퍼컴 시스템 분석 - 계산노드 March 3rd 2013) Retrieved from: <http://victorna.blogspot.kr/2013/07/tianhe-2milky-way-2.html>
- [16] ©Grey Matter Ltd. Programming the Xeon Phi, Intel Software Showcase [Graph illustration the parallel performance of Xeon & Xeon Phi]. Retrieved from: <http://www.greymatter.com/corporate/showcase/intel/xeon-phi/>
- [17] Cindy LaChapelle, Principal Consultant. SAFETY FIRST, Emerging Trends in IT Disaster Recovery. Retrieved from: http://www.isg-one.com/knowledgecenter/whitepapers/private/papers/White_Paper_DR_Trends.pdf
- [18] Copyright © Acronis, Inc. The Acronis Global Disaster Recovery Index: 2012. Retrieved from: http://eu.acronisinfo.com/files/2012/01/DR_Index_2012_EU_EN_120127.pdf

- [19] IDG Research Services. Quick Poll: Disaster Recovery Trends and Metrics Survey. Retrieved from: <http://www.falconstor.com/infographics/2013-disaster-recovery-trends-infographic>
- [20] Microsoft SQL Server, App Fabric, Technical Reference Guide. High Availability and Disaster Recovery (Middleware) - a Technical Reference Guide for Designing Mission-Critical Middleware Solutions. Retrieved from: <http://technet.microsoft.com/en-us/library/hh393522.aspx>
- [21] Wikipedia. Peer-to-peer. Retrieved from: <http://en.wikipedia.org/wiki/Peer-to-peer>
- [22] Andrea Righi, Ari Jort, Austin Gonyou, Ben Spade, Brian Elliott Finley, Curtis Zinzilieta, Dann Frazier, Denise Walters, Greg Pratt, Jason R. Mastaler, Josh Aas. SystemImager@v4.1.6 Manual. Retrieved from: <http://www.systemimager.org/documentation/systemimager-manual-4.1.6.pdf>
- [23] Brian Elliott Finley, Erich Focht, Bernard Li, Andrea Righi. Installation time comparison (Fig1), SystemImager and BitTorrent: a peer-to-peer approach for Large-Scale OS Deployment. Retrieved from: <http://download.systemimager.org/pub/docs/SystemImager-LinuxTag-2007-paper.pdf>



Super-computational Materials Simulation Laboratory /
Computational Science Center

[Feature Articles]

Non-volatile Control of 2DEG Conductivity at Oxide Interfaces

**Shin Ik Kim**Electronic Materials
Research Center
shinik@kist.re.kr**Jin Sang Kim**Electronic Materials
Research Center
jskim@kist.re.kr**Seung Hyub
Baek**Electronic Materials
Research Center
shbaek77@
kist.re.kr

Abstract

Epitaxial complex oxide thin film heterostructures have attracted much attention for their multifunctional properties, such as piezoelectricity, ferroelectricity, superconductivity and ferromagnetism. In addition to these bulk properties, the interface between two different oxides provides a promising platform to explore novel properties where symmetry breaking is easily controlled. Two-dimensional electron gas (2DEG) confined at the interface between two insulating perovskite oxides, such as lanthanum aluminate (LaAlO_3) and strontium titanate (SrTiO_3), provides expanded opportunities to develop various electronic and memory devices on a nano-scale. In order for 2DEG to be used in electronic devices, it is desirable to reproducibly control the conductance of 2DEG within a large range. Recently, it was reported that the conductivity of 2DEG could be controlled by an external electric field. However, the switched conductivity of 2DEG was not stable over time, resulting in relaxation because of the reaction between the charged surface of the LaAlO_3 layer and atmospheric conditions. In this report, we demonstrate a way to control the conductivity of 2DEG in a non-volatile way by integrating ferroelectric materials into a LAO/STO heterostructure. We fabricated epitaxial $\text{Pb}(\text{Zr}_{0.2}\text{Ti}_{0.8})\text{O}_3$ films on a $\text{LaAlO}_3/\text{SrTiO}_3$ heterostructure by pulsed laser deposition. The conductivity of 2DEG was reproducibly controlled with 3-order magnitude by switching the spontaneous polarization of the $\text{Pb}(\text{Zr}_{0.2}\text{Ti}_{0.8})\text{O}_3$ layer.

The controlled conductivity was time stable without relaxation over 60 hours. This was also consistent with the robust polarization state of the $\text{Pb}(\text{Zr}_{0.2}\text{Ti}_{0.8})\text{O}_3$ layer, as confirmed by piezoresponse force microscopy. This work demonstrates a model system to combine ferroelectric material and 2DEG, which could facilitate development of novel multifunctional electronic devices.

Introduction

Two-dimensional electron gas (2DEG) is an accumulation of electrons free to move in x - and y -directions, but tightly confined in the z -direction. In 2004, a similar 2DEG was observed at the oxide interfaces between two band insulators, LaAlO_3 (LAO) and SrTiO_3 (STO) [1-4]. Intensive experimental and theoretical efforts have since revealed that 2DEG at oxide interfaces exhibits a wider spectrum of novel physical properties compared to 2DEG at semiconductor interfaces. Moreover, oxide 2DEG has a much narrower distribution of electrons within a few nanometers compared to semiconductor 2DEG. This enables the fabrication of nanoscale electronic circuits with a ~ 2 nm-wide conducting path equivalent to the size of carbon nanotubes. Thus, 2DEG at complex oxide interfaces has enormous potential in the development of future oxide nanoelectronic devices.

In order to develop useful devices using oxide 2DEGs, it is imperative to functionalize the physical properties of 2DEG in a controllable way. One possible way is to integrate 2DEG with additional functional layers, such as the multifunctional oxide/LAO/STO heterostructure shown in Figure 1. Juxtaposition of 2DEG and a multifunctional oxide overlayer can create novel couplings, which can provide a control knob to modulate 2DEG conductivity. Moreover, a multifunctional oxide layer can act as a selective channel to amplify a particular external-signal-modulating 2DEG. In this scheme, the structure can be used as a highly sensitive multifunctional sensor. In this

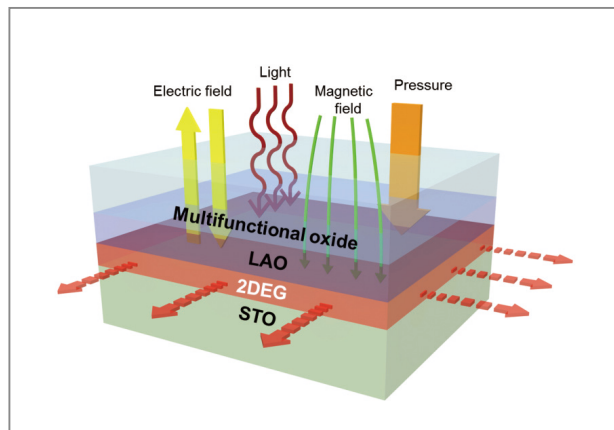


Figure 1. Schematic illustration of functionalizing 2DEG by epitaxial heterostructuring. This schematic shows that the physical properties of 2DEG can be modulated by various external signals which are selectively amplified depending on the functionality of the overlayers.

article, we demonstrate a functionalized oxide 2DEG system integrating epitaxial ferroelectric $\text{Pb}(\text{Zr}_{0.2}\text{Ti}_{0.8})\text{O}_3$ (PZT) thin films on LAO/STO as a model system. Our work presents how the functionalization of oxide 2DEG using an epitaxial heterostructuring approach leads to a solution for the technologically important retention issue of 2DEG control.

It has been reported that the electrical conductivity of oxide 2DEG remains unchanged even when the applied field is removed, indicating that oxide 2DEG has a pseudo-memory effect [5]. However, it is readily relaxed into its original ground state in a few hours under ambient conditions [5, 6]. Moreover, the dynamics of the back-switching process are dependent on environmental conditions such as humidity and oxygen [5]. This implies that the as-grown oxide 2DEG is sensitive to external stimuli. Unfortunately, it is difficult in practice to realize such systems due to the disparate growth conditions for 2DEG and ferroelectricity; the formation of 2DEG is generally more successful when there is low oxygen pressure (<0.1 mTorr) during deposition while ferroelectricity flourishes under high oxygen pressure (>100 mTorr) which suppresses the creation of oxygen vacancies and subsequent degradation of the ferroelectricity.

Results

Here we demonstrate the non-volatile switching of 2DEG conductivity incorporating epitaxial ferroelectric PZT thin film on LAO/STO. The polarization direction of the PZT overlayer, switchable by an electric field, electrostatically modulates the 2DEG electrical conductance by over three orders of magnitude. The bi-stable nature of ferroelectric polarization stabilizes the switched conducting state of 2DEG over 50 hours without relaxation. A key aspect of the present study was to synthesize high-quality epitaxial PZT/LAO/STO heterostructures possessing both 2DEG and ferroelectric characteristics at the LAO/STO interface and PZT overlayer. We synthesized an (001)-oriented PZT (100 nm)/LAO (4 nm)/STO heterostructure where a modulation of charges is maximized by 180° polarization switching in the *c*-oriented tetragonal PZT film.

Figures 2a and b show atomic force microscope (AFM) images of LAO and PZT surfaces in the PZT/LAO/STO heterostructure, respectively. LAO film on STO shows an atomically smooth surface with flat terraces and single-unitcell-high (~ 4 Å) steps. This indicates that the LAO/STO can serve as a good substrate on which to grow epitaxial PZT films. 100 nm-thick PZT film on LAO/STO also exhibits a smooth surface with a two-unitcell-height roughness at its maximum.

The crystalline quality of the PZT/LAO/STO heterostructure was analyzed by four-circle high resolution X-ray diffraction (HRXRD). Figure 2c shows the out-of-plane θ - 2θ scan of the PZT/LAO/STO heterostructure. The XRD pattern shows that the PZT films grown on LAO/STO are purely *c*-oriented without *a* or *b* domains. The out-of-plane lattice parameter is 4.132 Å, which is longer than bulk PZT ($a = b = 3.930$ Å, $c = 4.120$ Å), indicating that the PZT layer is biaxially compressively strained due to the lattice mismatch with the STO substrate ($a = 3.905$ Å). Note that the diffraction peaks from the LAO layer are not seen due to the narrow thickness. Azimuthal ϕ scans of PZT film show in-plane epitaxy with a cube-on-cube epitaxial relation (Figure 2d). Therefore, we can conclude

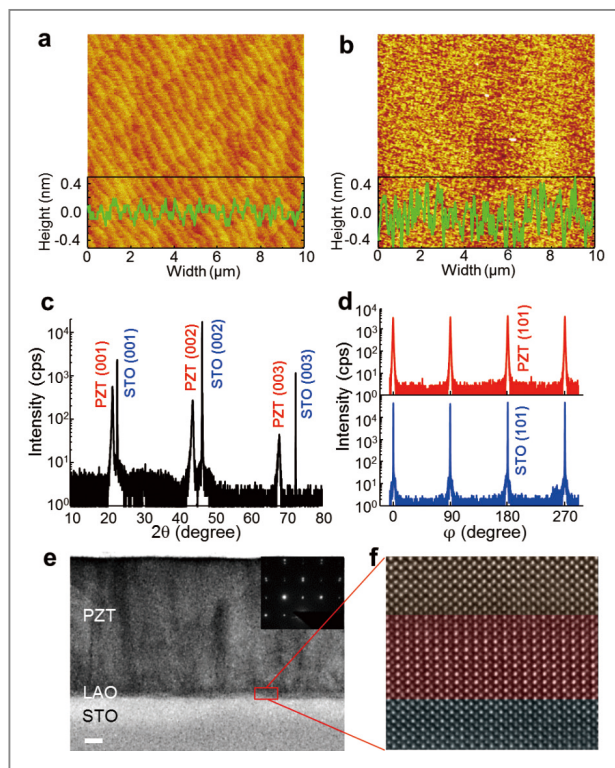


Figure 2. Structural characterization of the PZT/LAO/STO structure. Surface morphology of the (001) epitaxially grown (a) LAO (4 nm)/STO and (b) PZT (100 nm)/LAO (4 nm)/STO measured by AFM. (c) XRD out-of-plane θ - 2θ scan for the PZT/LAO/STO heterostructure. (d) -scan of the 101 PZT and 101 STO diffraction peaks. (e) Cross-sectional TEM image. The inset shows the selected area electron diffraction (SAED) pattern for all three layers. The zone axis is [100]. The scale bar is 10 nm. (f) A high-resolution TEM (HRTEM) image at the PZT/LAO/STO interface.

that both PZT and LAO thin films were epitaxially grown on STO substrate.

Transmission electron microscopy (TEM) analysis also confirmed epitaxial growth of PZT and LAO layers on the STO substrate. Figure 2e is a bright-field TEM image with low magnification. The inset shows the selected-area electron diffraction (SAED) pattern taken from the PZT/LAO/STO layer along the [100] zone axis. The SAED pattern also indicates that the PZT and LAO layers were epitaxially grown on the STO substrate. The high-resolution TEM image (Figure 2f) exhibits an atomically sharp interface between the PZT, LAO, and STO.

In order to characterize the interaction between

ferroelectric switching and 2DEG conductivity, we fabricated a four-point measurement pattern with a conducting channel of $50\ \mu\text{m} \times 70\ \mu\text{m}$, as shown in [Figure 3a](#). A Pt top electrode with a diameter of $50\ \mu\text{m}$ was lithographically patterned on top of the 2DEG channel. Gate voltage (V_G) was applied for ~ 10 seconds between the top Pt electrode and the bottom 2DEG layer to switch the polarization orientation of the PZT overlayer. Then electrical conductance of 2DEG was measured by a four-point probe method. Note that this is a prototypical geometry of a 3-terminal transistor. The possible photocurrent effect in the LAO/STO interface was excluded by limiting the exposure of the sample to light during electrical measurements.

[Figure 3b](#) shows the electrical conductance measurement of the 2DEG channel as a function of the applied gate voltage. The result shows two important aspects: (1) hysteretic behavior with a square-like shape and (2) a large on/off ratio. The 2DEG conductance versus gate voltage measurement exhibits a hysteresis loop with a coercive voltage of $\sim 8.5\ \text{V}$. The 2DEG conductance is saturated at a high conductance state over $+10\ \text{V}$ and is saturated at a low conductance state over $-15\ \text{V}$. This hysteretic behavior is direct evidence of the ferroelectric control of 2DEG conductivity. Note that the hysteresis loop shifted to a negative bias by $\sim 3.5\ \text{V}$. We attribute this to the imprint phenomenon where the built-in bias in a ferroelectric material laterally shifts the hysteresis loop in the polarization-versus-electric-field (P - E) measurement.

The 2DEG conductance is an *on* state with electron accumulation when the polarization of the PZT overlayer is pointing down, while it is an *off* state with electron depletion when the polarization is pointing up. The *on/off* ratio is over three orders of magnitude in our PZT/LAO/STO heterostructure. The remanent polarization of the $100\ \text{nm}$ thick PZT film was found to be $\sim 60\ \mu\text{C cm}^{-2}$. This polarization value corresponds to the surface charge density of $\sim 3.7 \times 10^{14}\ \text{cm}^{-2}$ at the PZT surfaces. Since the carrier density of 2DEG at the as-grown condition is $\sim 10^{13}\ \text{cm}^{-2}$, the charge density by the remanent polarization of

the PZT layer is more than enough to induce a metal-insulator transition at the 2DEG interface by polarization switching. Nonetheless, it is noteworthy that the *on/off* ratio is much higher than previously reported values by surface adsorption [6], oxygen vacancy migration, and AFM-based direct writing. We suggest that the *on/off* ratio could be further enhanced by replacing the PZT overlayer with other ferroelectrics of larger remanent polarizations, such as BiFeO_3 , and replacing the LAO with a ferroelectric material which could still generate 2DEG.

Another important feature of our ferroelectric control is the retention of controlled 2DEG conductivity. In order to evaluate the retention property, we monitored the switched 2DEG conductance as a function of time, as shown in [Figure 3c](#). Both low and high conducting states were stable with time over more than 50 hours of observation. This is consistent with the robust ferroelectricity observed in the PFM images shown in the [Figure 3c](#) insets. Moreover, the switched state survived even after exposing samples for an hour to various environmental conditions such as water, alcohol, and acetone. Note that previously reported surface-charge-mediated oxide 2DEG control methods showed that the *on* and *off* states are unstable [5,6], so they can be back-switched into their original states in a few hours [5]. Our method of ferroelectric control of oxide 2DEG is reversible, as highlighted in [Figure 3d](#).

Considerable research has been done to achieve the integration of 2DEG with ferroelectrics using metal/ferroelectric/semiconductor (MFS) structures, such as Pt/PZT/AlGaIn/GaN, where 2DEG is formed at the AlGaIn/GaN interface. The key difference of our work is the large *on/off* ratio; in prior research, 2DEG in the semiconductor interface had a small *on/off* ratio (< 5) while our sample shows a much larger value (> 1000) [7]. This may be due to the different spatial confinement of 2DEGs; oxide 2DEG is confined only within a few unit cells thickness while semiconductor 2DEG is distributed to the tens of nanometers [3]. Thus, the polarization switching on oxide 2DEG would be more effective. Also, a dead layer may

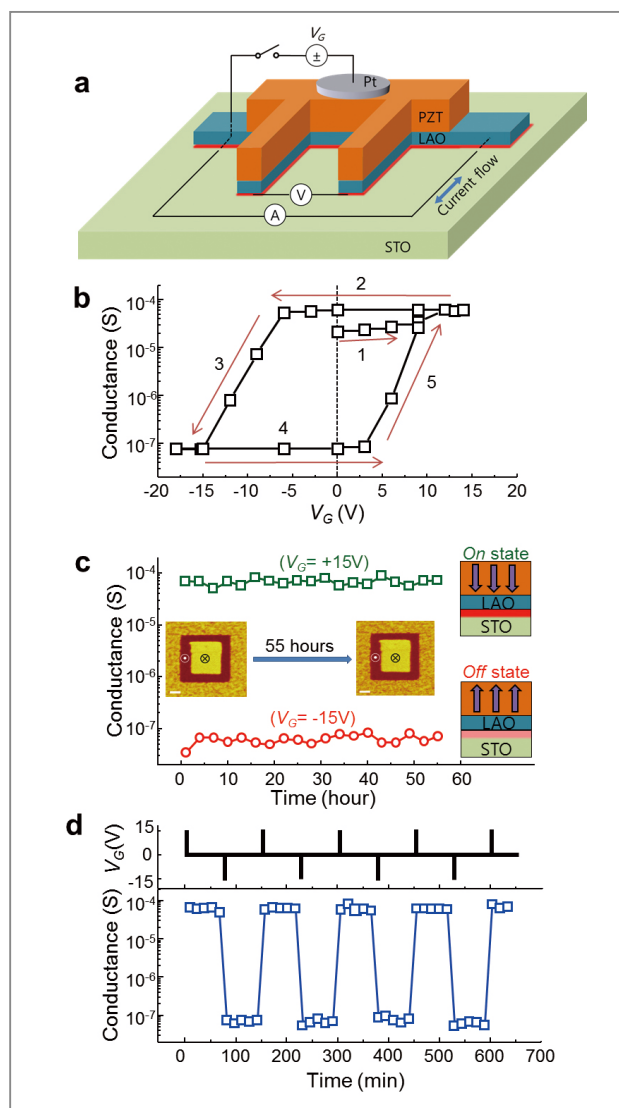


Figure 3. Non-volatile switching of 2DEG conductivity with a high on/off ratio (>1000). (a) A schematic of the four-point probe measurement of 2DEG conductance. A Pt top electrode with a $50\ \mu\text{m}$ diameter was lithographically patterned on PZT/LAO/STO bridge with $50\ \mu\text{m} \times 70\ \mu\text{m}$. (b) 2DEG conductance measurement versus applied gate voltage. 2DEG conductance was measured after applying gate voltage pulses of duration of 10 seconds. The arrows and numbers represent the gate voltage sweeping sequence. (c) The bi-stability of 2DEG conductance states over time. The insets in the right side show the polarization direction of the PZT overlayer for *on* (top) and *off* (bottom) states. The red layer between LAO and STO represents 2DEG; the brighter it is, the denser the electron density. The insets in the center show the out-of-plane PFM phase image after writing with $-15\ \text{V}_{\text{dc}}$ (dark) and $+6\ \text{V}_{\text{dc}}$ (bright). Over 55 hours, the ferroelectric domains remain stable. The scale bar is $1\ \mu\text{m}$. (d) Reversible switching of 2DEG conductance. The top graph shows the applied gate voltage pulses, and the bottom graph exhibits the concomitant 2DEG conducting states.

have formed at the ferroelectric/semiconductor interface. Due to the high growth temperature and high partial pressure of oxygen required for ferroelectric thin film growth, defects might have occurred in the ferroelectric/semiconductor interface arising from the diffusion of oxide-layer cations into the semiconductor and subsequent oxidation of the surface of the semiconductor. Such poorly-defined interfaces would reduce the effective magnitude of the electric field by polarization on 2DEG. By contrast, all the oxide layers forming our PZT/LAO/STO heterostructure have the same perovskite structure. This enables the synthesizing of epitaxial heterostructures with atomically sharp interfaces (Figure 2), thereby suppressing the formation of any dead layers at each interface.

In addition to the non-volatile control of 2DEG, our PZT/LAO/STO heterostructure can respond to external mechanical stress as a sensor. PZT is an excellent piezoelectric material, especially when the composition of Zr and Ti is near the morphotropic phase boundary. External mechanical signals, such as pressure and bending, will induce charges at the PZT/LAO interface due to high longitudinal and transverse piezoelectric coefficients, leading to the modulation of 2DEG conductivity. High-quality PZT/LAO/STO heterostructures can be integrated into Si substrate using state-of-the-art film deposition techniques. Using well-developed microfabrication processes on this platform, multifunctional oxide electronics combining 2D and 3D physical phenomena may be developed which can store information without external power, process signals as high speed transistors, and act as active sensors and actuators.

Conclusion

In summary, we have demonstrated the non-volatile control of 2DEG conductivity at a LAO/STO interface using ferroelectric polarization switching of an epitaxial PZT overlayer. Our work shows that 2DEG can be

reversibly turned on and off with a large on/off ratio (>1000) in a non-volatile manner. Our approach offers new opportunities to develop multifunctional nanoelectronics operating with other parameters such as magnetism, light, and spin. Moreover, our work provides a platform from which to expand our fundamental understanding of novel physics associated with multi-dimensional interacting phenomena.

Note

This article and images are drawn from "Non-Volatile Control of 2DEG Conductivity at Oxide Interfaces," in *Adv. mat.* Vol 25; 33, pp. 4612-4617.

References

- [1] Ohtomo A, Hwang HY. *Nature*. 2004; 427: 423.
- [2] Mannhart J, Blank DHA, Hwang HY, Millis AJ, Triscone JM. *MRS Bull.* 2008; 33: 1027.
- [3] Mannhart J, Schlom DG. *Science* 2010; 327: 1607.
- [4] Hwang H.Y, Iwasa Y, Kawasaki M, Keimer B, Nagaosa N, Tokura Y. *Nature Mater.* 2012; 11: 103.
- [5] Bi F, Bogorin DF, Cen C, Bark CW, Park JW, Eom CB, Levy J. *Appl. Phys. Lett.* 2010; 97: 173110.
- [6] Xie Y, Bell C, Hikita Y, Hwang HY. *Adv. Mat.* 2011; 23: 1744.
- [7] Igor S, Lisa M, Paul M, Nava S, *Appl. Phys. Lett.* 2006; 88: 043512.



Smart Electronic Materials / Electronic Materials Research Center

[Feature Articles]

Bright Multicolor Tunable Lanthanide Ion-Doped Inorganic Nanophosphors Less Than 10 nm in Size

**Ho Seong Jang**

Molecular Recognition Research Center
msekorea@kist.re.kr

**Su Yeon Kim**

Molecular Recognition Research Center
090612@kist.re.kr

Introduction

Lanthanide ion-doped inorganic crystals, i.e., phosphors, have been widely studied for application in display and illumination devices, such as cathode ray tubes (CRTs), plasma display panels (PDPs), electroluminescent devices (ELDs), field emission displays (FEDs), liquid crystalline displays (LCDs), fluorescent lamps (FLs), and light-emitting diodes (LEDs) [1]. In these devices, bulk powder phosphors in a micrometer-size range have been used. However, micrometer-sized phosphors are not small enough to be utilized in optoelectronic devices which require high transparency and flexibility. Recent research has looked at nanometer-sized phosphors and found them to be promising materials for applications in next-generation display devices, such as transparent and flexible display devices with ultrahigh definition. Moreover, nanophosphors can be useful in non-conventional applications, such as bio-imaging [2] and energy harvesting [3].

In contrast to conventional nanoscale luminophores such as organic dyes and quantum dots (QDs), nanophosphors show unique optical properties. The nanophosphors have high photostability, long life time ranging from $\sim\mu\text{s}$ to $\sim\text{ms}$, and sharp absorption and emission features compared with organic fluorophores [4]. In addition, the nanophosphors do not show photoblinking, unlike the QDs, and they are environmentally benign (containing no Cd or Pb) [4-5]. Due to the quantum confinement effect, the luminescent color of QDs can be easily tailored by adjusting their size, while nanophosphors exhibit

unique emission color depending on the doped lanthanide ion [6-7]. Because the nanophosphors emit visible light via f-f transition in lanthanide ions (Ln^{3+} ions) except a Ce^{3+} ion, the luminescent color of the phosphors does not change when their size is varied [7]. Although this size-independent luminescence of the nanophosphors can be an advantage for labeling applications, the embodiment of tunable multicolor emission from the nanophosphors under single wavelength excitation is beneficial for multiplexed biological detection as well as display device applications [5, 8].

The multicolor tuning of nanophosphors can be achieved via co-doping the host materials with two or more Ln^{3+} ions. Recently, Tb^{3+} and Eu^{3+} co-doped nanophosphors were reported [9-10]. Podhorodecki et al. showed that $\beta\text{-NaYF}_4:\text{Eu}(5\%),\text{Tb}(5\%)$ nanophosphors emit various colors from green to red under various excitation wavelengths which correspond to the wavelength at which the light is absorbed by the phosphors via f-f transitions of Tb^{3+} and Eu^{3+} [9]. In another study, Bettinelli's group reported on $\text{Tb}^{3+}/\text{Eu}^{3+}$ and $\text{Ce}^{3+}/\text{Tb}^{3+}/\text{Eu}^{3+}$ co-doped zinc phosphate glasses. However, those glass phosphors exhibited yellowish green emissions [10]. Although color tuning is possible in Tb^{3+} and Eu^{3+} co-doped phosphor systems, various excitation wavelengths are necessary to create multicolor emission, and brightness of the emitted light is not high because absorptions via f-f transition of Tb^{3+} or Eu^{3+} are not strong [7]. Thus, realization of tunable multicolor emission under single wavelength excitation is still challenging. In this article, we report on Ce, Tb, Eu co-doped $\beta\text{-Na(Y,Gd)F}_4$ nanophosphors. Since Ce^{3+} ions have strong absorption strength and a broad absorption band, excited energy is efficiently absorbed by Ce^{3+} ions. The absorbed energy is transferred to Tb^{3+} and Eu^{3+} ions, which results in a bright, tunable multicolor emission. The size of $\beta\text{-Na(Y,Gd)F}_4:\text{Ce,Tb,Eu}$ was also controlled to be smaller than 10 nm. Ultra-small sub-6 nm $\beta\text{-Na(Y,Gd)F}_4:\text{Ce,Tb,Eu}$ core and sub-10 nm $\beta\text{-Na(Y,Gd)F}_4:\text{Ce,Tb,Eu}/\beta\text{-NaYF}_4$ core/shell nanophosphors were synthesized and their luminescent properties were investigated. In addition,

core/shell nanophosphor-polymer composites were prepared to investigate the feasibility of application of the nanophosphors to transparent display devices.

Synthesis and characterization of multicolor tunable nanophosphors

Hexagonal $\beta\text{-Na(Y,Gd)F}_4:\text{Ce,Tb,Eu}$ nanophosphors were synthesized via a solution chemical route and reaction temperature was 320°C . The ultra-small sub-6nm $\beta\text{-Na(Y,Gd)F}_4:\text{Ce,Tb,Eu}$ core nanophosphors and $\beta\text{-Na(Y,Gd)F}_4:\text{Ce,Tb,Eu}/\beta\text{-NaYF}_4$ core/shell nanophosphors were synthesized at 300°C . To prepare the nanophosphor-polydimethylsiloxane (PDMS) composites, 0.4 ml of the $\beta\text{-Na(Y,Gd)F}_4:\text{Ce,Tb,Eu}/\beta\text{-NaYF}_4$ core/shell nanophosphor solution was mixed with 4 ml of SYLGARD 184 silicone elastomer followed by mixing with 0.4 ml of a curing agent (Dow Corning Corp.) Finally, the nanophosphor-PDMS composites were heat-treated at 80°C after overnight aging. The sizes of the synthesized nanophosphors were characterized by using a Tecnai F20 G² transmission electron microscope at an accelerating voltage of 200 kV. The photoluminescence spectra and decay profiles of the nanophosphors were obtained with a Hitachi F-7000 spectrophotometer.

Synthesis of bright green-emitting nanophosphors

Color tuning via energy transfer from Tb^{3+} to Eu^{3+} causes the emission from Tb^{3+} ions to weaken. Thus, strong green-emitting Tb^{3+} -doped nanophosphors should be synthesized before the synthesis of color-tunable Tb^{3+} and Eu^{3+} co-doped nanophosphors. As shown in Figure 1, $\beta\text{-NaYF}_4:\text{Ce}(10\%),\text{Tb}(15\%)$ ($\beta\text{-NaYF}_4:\text{Ce,Tb}$) nanophosphors with uniform shapes and size distributions showed bright green light under the excitation of ultraviolet (UV) light (254 nm). Highly monodisperse

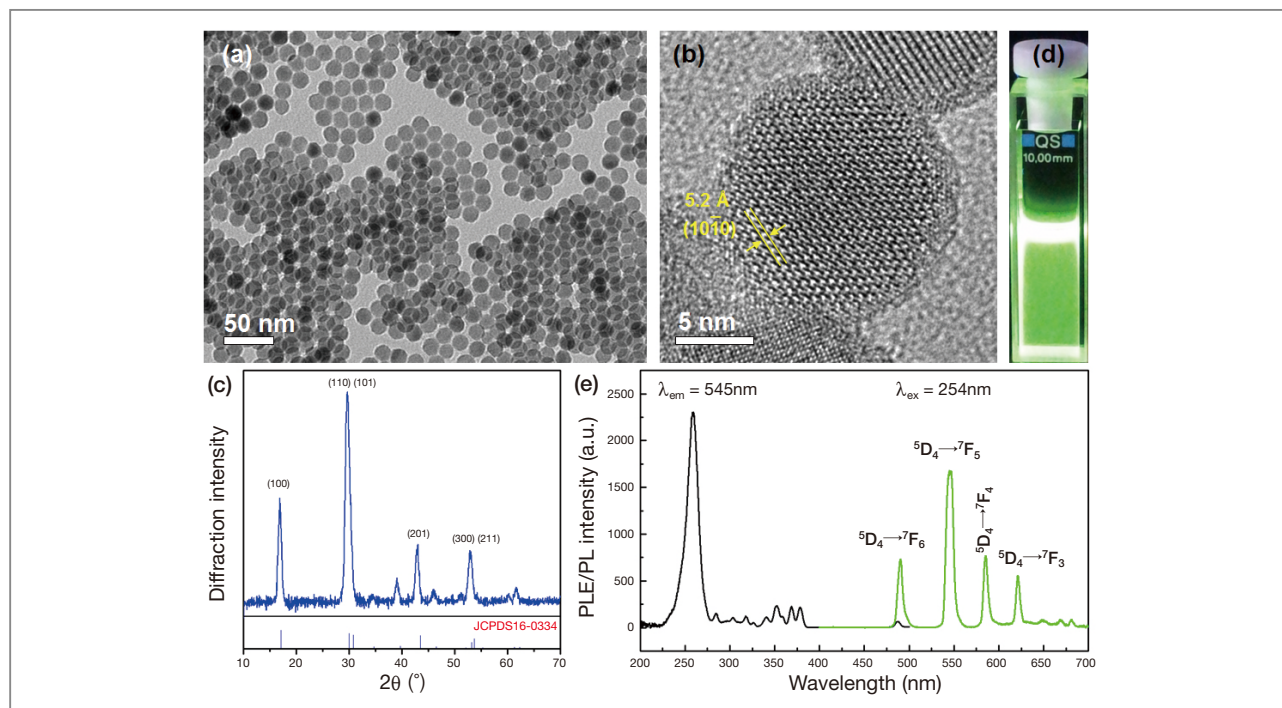


Figure 1. (a) TEM and (b) HR-TEM images, (c) x-ray diffraction (XRD) pattern, (d) digital camera image, and (e) PLE and PL spectra of β -NaYF₄:Ce,Tb nanophosphors synthesized at 320°C. The luminescent image was taken under a hand-held UV lamp.

β -NaYF₄:Ce,Tb exhibited an average particle size of ca. 16.7 nm and a single crystalline nature, as observed through transmission electron microscopy (TEM) and high resolution TEM (HR-TEM) images (Figures 1a and b). The distance between two resolved lattice fringes was 5.2 Å which corresponds to d spacing between 100 planes of β -NaYF₄. In addition, the synthesized nanophosphors had a single hexagonal phase without impurity phases (Figure 1c). Broad diffraction peaks indicate that the size of the nanophosphors lies in the nanometer regime. The bright green light emitted from β -NaYF₄:Ce,Tb is attributed to the energy transfer from Ce³⁺ to Tb³⁺ followed by f-f transition in Tb³⁺ ions. A strong and broad photoluminescence excitation (PLE) band is observed at about 255 nm due to Ce³⁺ absorption of UV light at this wavelength. Total luminescence color was green because of the strong emission intensity of the $^5D_4 \rightarrow ^7F_5$ transition of Tb³⁺ ions (Figures 3d and e).

To further increase of the PL intensity of

β -NaYF₄:Ce,Tb, Gd³⁺ ions were co-doped. As depicted in the energy level diagram shown in Figure 2a, excitation energy can be efficiently transferred from Ce³⁺ to Tb³⁺ via Gd³⁺ ions. After Gd³⁺ co-doping, a weak emission peak at 312 nm was generated, while the weak Ce³⁺ emission band nearly vanished. These results indicate the energy transfer from Ce³⁺ to Gd³⁺. When 15 mol% of Gd³⁺ was doped into β -NaYF₄:Ce,Tb, Tb³⁺, emission intensity decreased. This result can be explained as follows. Excited energy was not fully transferred from Ce³⁺ to Tb³⁺ via Gd³⁺ and some of the excited energy was consumed to generate Gd³⁺ emission when the doping concentration of Gd³⁺ was low. However, even in the case of low Gd³⁺ concentration, some of the excited energy was transferred from Gd³⁺ to Tb³⁺. As shown in Figure 2c, photoluminescence (PL) intensity from Gd³⁺ ions was much higher in β -NaYF₄:Gd(15%),Ce(10%) than in β -NaYF₄:Gd(15%),Ce(10%),Tb(15%). As a result of the energy transfer from Gd³⁺ to Tb³⁺, decay time for the Gd³⁺

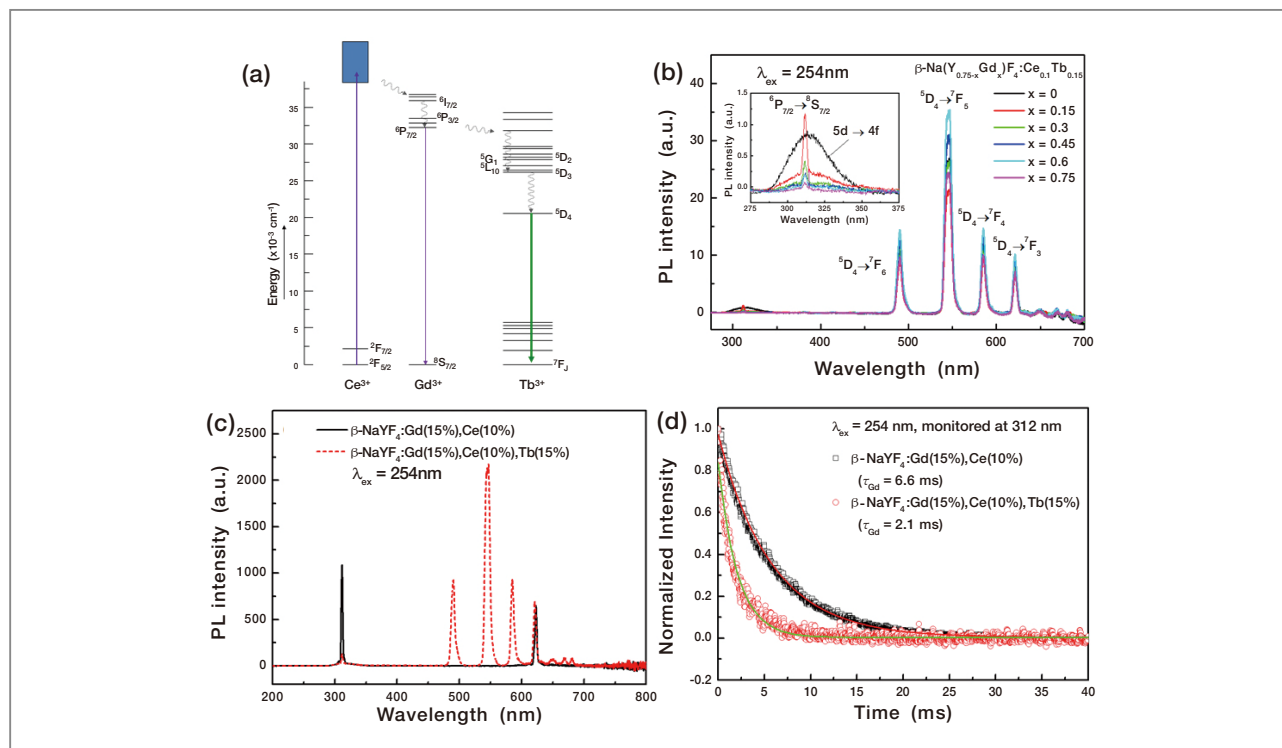


Figure 2. (a) Schematic energy level diagram showing energy transfer. (b) PL spectra of Gd³⁺ co-doped β-NaY₄:Ce,Tb nanophosphors. (c, d) PL spectra and decay profiles of β-NaY₄:Gd(15%),Ce(10%) and β-NaY₄:Gd(15%),Ce(10%),Tb(15%) under excitation of 254 nm.

emission was shortened from 6.6 ms to 2.1 ms (Figure 2d). However, as Gd³⁺ concentration increased in the host lattice, the PL intensity of Tb³⁺ also increased and the optimized Gd³⁺ concentration was 60 mol%.

Multicolor emission from β-Na(Y,Gd)F₄:Ce,Tb,Eu nanophosphors

Figure 3a shows the PL spectra of Gd³⁺ (60 mol%) co-doped β-NaY₄:Ce,Tb,Eu (β-Na(Y,Gd)F₄:Ce,Tb,Eu) with varying Eu³⁺ concentrations. As we expected, Eu³⁺ emission peaks in the red spectral region were observed with Tb³⁺ emission peaks. Additional Eu³⁺ emission peaks that appeared are ascribed to the electronic transitions of ⁵D₀ → ⁷F_J (J = 1, 2, 3, 4). PL intensity due to the ⁵D₀

→ ⁷F₂ transition is higher than that due to the ⁵D₀ → ⁷F₁ transition which indicates that Eu³⁺ ions are located at the non-inversion symmetric sites [11]. In the PLE spectrum of β-Na(Y,Gd)F₄:Ce,Tb,Eu monitored at 616 nm shown in Figure 3b, excitation bands are observed at 254, 273, and 488 nm, which are due to the absorptions by 4f → 5d transition of Ce³⁺ ions, ⁸S_{7/2} → ⁶I_{7/2} transition of Gd³⁺ ions, and ⁷F₆ → ⁵D₄ transition of Tb³⁺ ions, respectively. This result supports the idea that the Eu³⁺ emission is attributed to the energy transfer from Ce³⁺ to Eu³⁺ through Gd³⁺ and Tb³⁺. In addition, the PLE spectrum of β-Na(Y,Gd)F₄:Ce,Eu (i.e., no Tb³⁺) monitored at 616 nm displayed a sharp peak at 273 nm, indicating that excited energy was also transferred from Ce³⁺ to Eu³⁺ through Gd³⁺. As a consequence, Eu³⁺ emission is attributed to the energy transfer of Ce³⁺ → Gd³⁺ → Tb³⁺ → Eu³⁺ and Ce³⁺ → Gd³⁺ → Eu³⁺. As the Eu³⁺ concentration

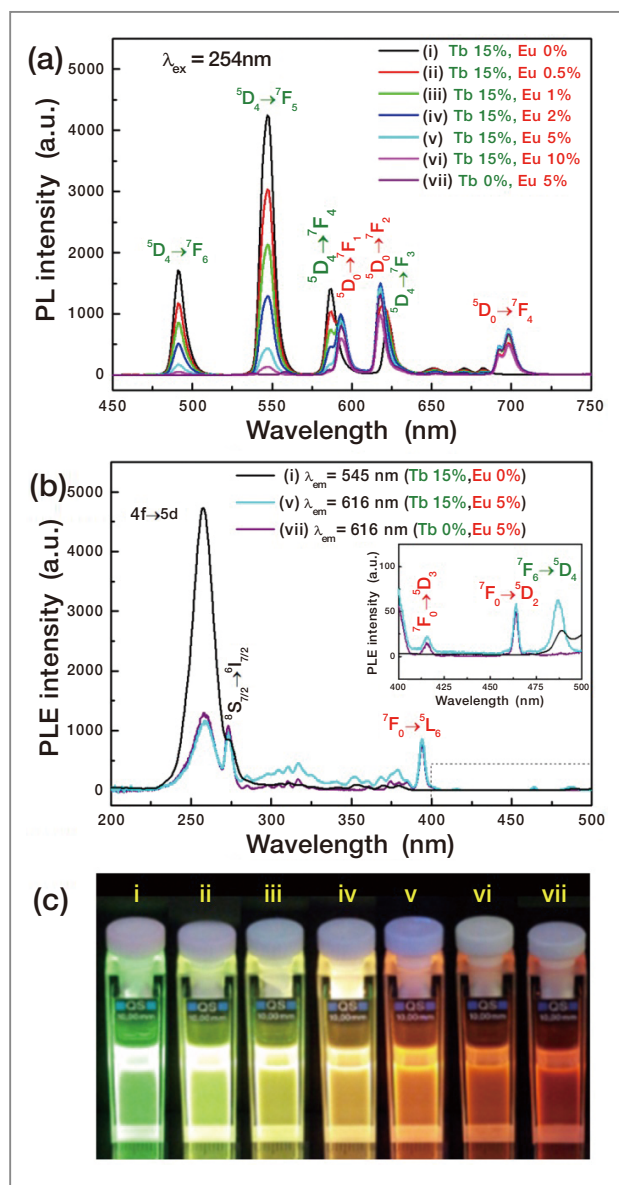


Figure 3. (a) PL spectra of β -Na(Y,Gd) F_4 :Ce,Tb,Eu nanophosphors with varying Tb^{3+} and Eu^{3+} concentrations under 254 nm excitation, (b) PLE spectra of β -Na(Y,Gd) F_4 :Ce,Tb,Eu nanophosphors monitored at 545 and 616 nm. (c) Digital camera image of β -Na(Y,Gd) F_4 :Ce,Tb,Eu nanophosphors under a hand-held UV lamp. [(Tb, Eu) = i: (15%, 0%), ii: (15%, 0.5%), iii: (15%, 1%), iv: (15%, 2%), v: (15%, 5%), vi: (15%, 10%), vii: (0%, 5%)]

increased in the host lattice, the ratio of PL intensity of the Tb^{3+} emission to that of the Eu^{3+} emission decreased due to the energy transfer of Tb^{3+} to Eu^{3+} . As a result, the β -Na(Y,Gd) F_4 :Ce,Tb,Eu nanophosphors emitted various

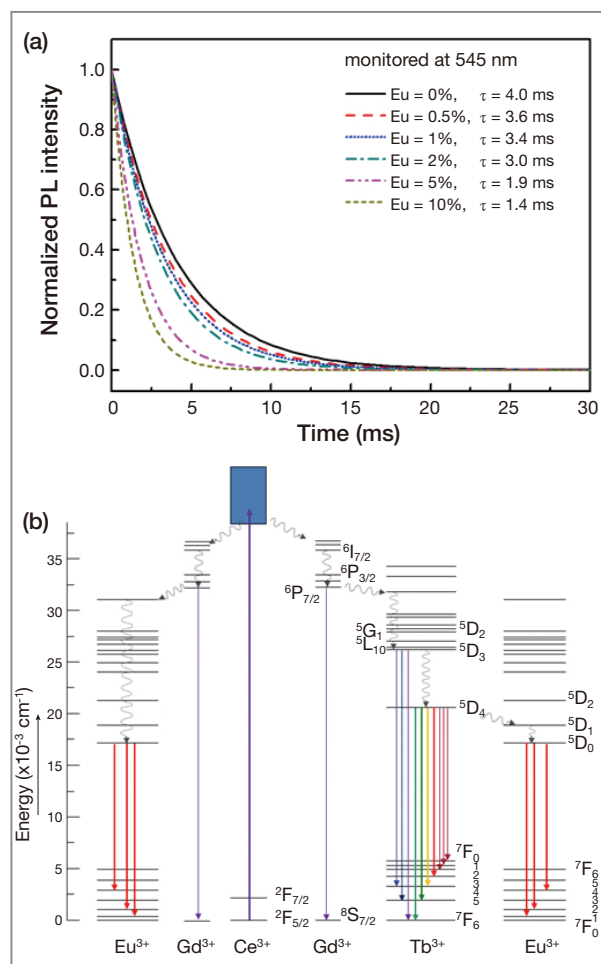


Figure 4. (a) Decay profiles of β -Na(Y,Gd) F_4 :Ce(10%),Tb(15%),Eu(x%) with various Eu^{3+} concentrations ($x = 0, 0.5, 1, 2, 5, 10$). (b) Schematic energy level diagram showing energy transfer in the β -Na(Y,Gd) F_4 :Ce,Tb,Eu nanophosphors.

visible lights of green, yellowish green, yellow, orange, scarlet, and red as shown in the photograph taken under single wavelength excitation of a hand-held UV lamp (Figure 3c).

The energy transfer from Tb^{3+} to Eu^{3+} can be verified by measuring decay times for Tb^{3+} emission as a function of Eu^{3+} concentrations. Because the energy transfer of $Tb^{3+} \rightarrow Eu^{3+}$ is attributed to multipolar interaction between Tb^{3+} and Eu^{3+} , according to Dexter's theory [12], energy transfer probability ($P(R)$) can be expressed as follows,

$$P(R) \propto \frac{Q_A}{R^b \tau_D} \int \frac{f_D(E) F_A(E)}{E^c} dE \quad (1)$$

Where, Q_A is the total absorption cross-section of the acceptor, R is the distance between the donor and the acceptor, τ_D is the decay time for the donor emission, b and c are the parameters depending on the type of energy transfer, and is $\int \frac{f_D(E) F_A(E)}{E^c} dE$ spectral overlap between emission of the donor and absorption of the acceptor. Based on eq. (1), the probability of energy transfer $P(R)$ is inversely proportional to the decay time. As Eu^{3+} concentration increased, decay time for the Tb^{3+} emission shortened. This result confirms the energy transfer from Tb^{3+} to Eu^{3+} in the $\beta\text{-Na(Y,Gd)F}_4\text{:Ce,Tb,Eu}$ nanophosphors. Based on these decay time results and PLE spectra, the energy transfer mechanism is illustrated in Figure 4b. External energy is absorbed by Ce^{3+} ions and the excited energy is transferred to Gd^{3+} ions and then transferred to Eu^{3+} ions directly and/or via Tb^{3+} ions from Gd^{3+} ions. As a result, a very weak Gd^{3+} emission peak and Tb^{3+} and Eu^{3+} emission peaks are generated at UV, green, and red spectral regions, respectively.

Ultra-small multicolor tunable nanophosphors

Although $\beta\text{-Na(Y,Gd)F}_4\text{:Ce,Tb,Eu}$ nanophosphors exhibited tunable multicolor emission by adjusting dopant amounts, their size hardly changed and remained in the range of 15 – 18 nm. We could synthesize ultra-small nanophosphors below 10 nm in size by simply reducing reaction temperature to 300°C from 320°C. When the reaction temperature was 300°C, $\beta\text{-Na(Y,Gd)F}_4\text{:Ce,Tb,Eu}$ nanophosphors sowed small sizes of 4.8 – 5.9 nm as shown in Figure 5. Despite their ultra-small sizes, they showed high crystallinity, judging from the clear lattice fringes in their HR-TEM images (Figure 5b). The ultra-small size is supported by broader XRD peak width. Although reaction temperature was lowered to 300°C, no impurity phases were observed in their XRD patterns and all

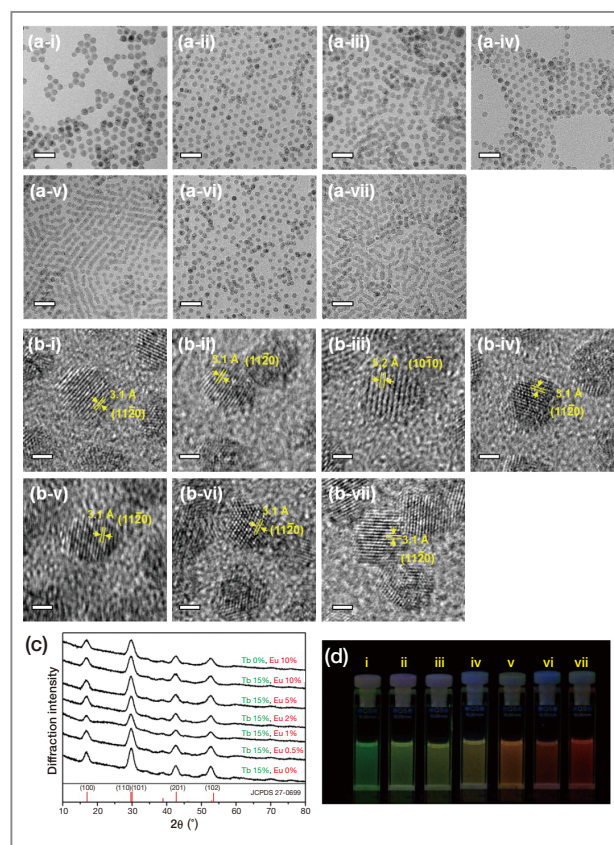


Figure 5. (a) TEM, (b) HR-TEM images, and (c) XRD patterns of the sub-6 nm $\beta\text{-Na(Y,Gd)F}_4\text{:Ce,Tb,Eu}$ nanophosphors with various Tb^{3+} and Eu^{3+} concentrations, and (d) digital camera image of the sub-6 nm $\beta\text{-Na(Y,Gd)F}_4\text{:Ce,Tb,Eu}$ nanophosphors under the illumination of a hand-held UV lamp. Scale bars in (a) indicate 20 nm and those in (b) represent 5 nm. [(Tb, Eu) = i: (15%, 0%), ii: (15%, 0.5%), iii: (15%, 1%), iv: (15%, 2%), v: (15%, 5%), vi: (15%, 10%), and vii: (0%, 5%)]

synthesized ultra-small nanophosphors exhibited a single hexagonal phase (Figure 5c). However, luminescence from the nanophosphors weakened considerably due to significantly increased surface area to volume ratio, as shown in the photograph in Figure 5d.

By forming inorganic shells on the core nanophosphors, luminescence from the ultra-small $\beta\text{-Na(Y,Gd)F}_4\text{:Ce,Tb,Eu}$ was dramatically enhanced. After $\beta\text{-NaYF}_4$ shell formation, particle sizes of the nanophosphors increased slightly. However, the sizes of $\beta\text{-Na(Y,Gd)F}_4\text{:Ce,Tb,Eu}/\beta\text{-NaYF}_4$ core/shell nanophosphors were still smaller than 10 nm. Although the core/shell

nanophosphors lay in an ultra-small size range, activator ions were protected by surface quenchers, such as surface defects, solvent ligand, and others. Therefore, PL intensities of the ultra-small β -Na(Y,Gd)F₄:Ce,Tb,Eu substantially increased and bright multicolor emission was realized from the ultra-small nanophosphors, as shown in Figure 6. PL quantum yield (QY) of the ultra-small nanophosphors was determined by comparing the integrated PL intensities of the nanophosphors with that of a reference organic dye whose absolute QY is well known. Rhodamine 6G was used as a reference sample and its QY is 95% in ethanol solution. According to Han et al. [13], the PL QY of the nanophosphors can be calculated by using the following equation,

$$QY_s = QY_{ref} \left(\frac{PL_s}{PL_{ref}} \right) \left(\frac{Abs_{ref}}{Abs_s} \right) \left(\frac{n_s}{n_{ref}} \right)^2 \quad (2)$$

Where *QY*, *PL*, *Abs*, and *n* represent the quantum yield, integrated PL intensity, absorbance at excited wavelength, and refractive index of the solvent,

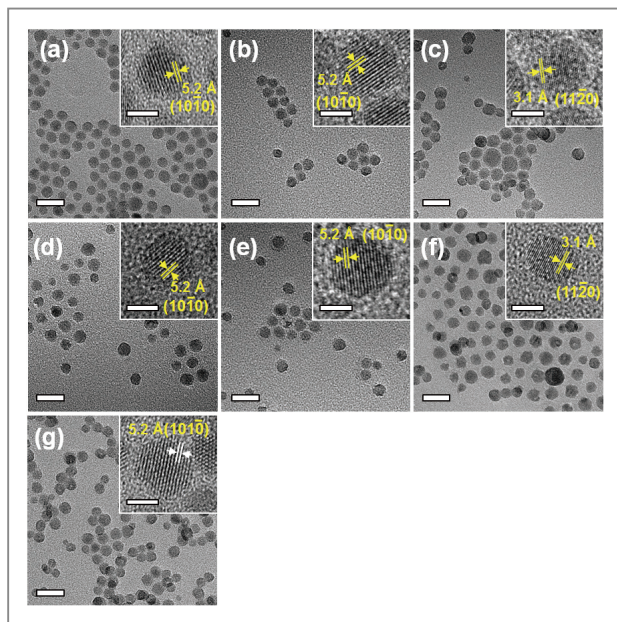


Figure 6. TEM images of sub-10 nm β -Na(Y,Gd)F₄:Ce,Tb,Eu/ β -NaYF₄ nanophosphors with various Tb³⁺ and Eu³⁺ concentrations. Scale bars are 20 nm. [(Tb, Eu) = a: (15%, 0%), b: (15%, 0.5%), c: (15%, 1%), d: (15%, 2%), e: (15%, 5%), f: (15%, 10%), and g: (0%, 5%)] Insets show HR-TEM images and scale bars represent 5 nm.

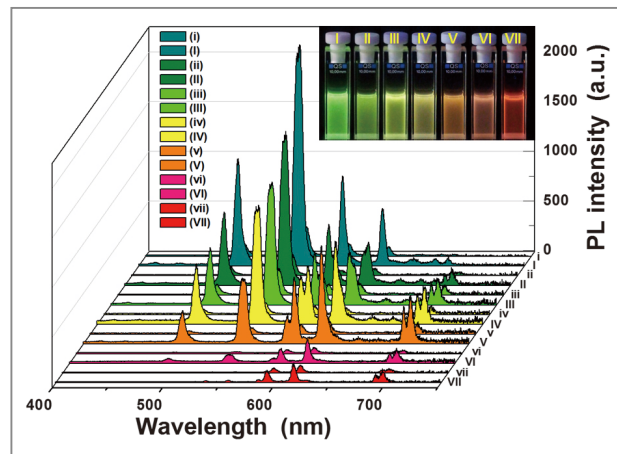


Figure 7. PL spectra of β -Na(Y,Gd)F₄:Ce,Tb,Eu and β -Na(Y,Gd)F₄:Ce,Tb,Eu/ β -NaYF₄ nanophosphors under the excitation of 254 nm UV light. Inset shows luminescence image of sub-10 nm β -Na(Y,Gd)F₄:Ce,Tb,Eu/ β -NaYF₄ with varying Tb³⁺ and Eu³⁺ concentrations. [(Tb, Eu) = i and I: (15%, 0%), ii and II: (15%, 0.5%), iii and III: (15%, 1%), iv and IV: (15%, 2%), v and V: (15%, 5%), vi and VI: (15%, 10%), and vii and VII: (0%, 5%)]. Lowercase letters indicate core nanophosphors and uppercase letters indicate core/shell nanophosphors.

respectively, and subscripts *s* and *ref* mean nanophosphor sample and reference dye, respectively. Although the shape of the PL spectrum of the rhodamine 6G is different from those of the β -Na(Y,Gd)F₄:Ce,Tb,Eu and β -Na(Y,Gd)F₄:Ce,Tb,Eu/ β -NaYF₄ nanophosphors, it can be used as a reference sample because of its broad emission covering the emission peaks from the core and core/shell nanophosphors [14-15]. To avoid a self-quenching effect, absorbance values were maintained in the range of 0.05 – 0.25 [16]. By comparing the QY of rhodamine 6G in ethanol solution, the QYs of β -Na(Y,Gd)F₄:Ce,Tb,Eu and β -Na(Y,Gd)F₄:Ce,Tb,Eu/ β -NaYF₄ nanophosphors were calculated to be 1.1 – 6.9% and 6.7 – 44.4%, respectively, depending on Tb³⁺ and Eu³⁺ concentrations.

Core/shell nanophosphor-PDMS composites

The ultra-small size and high brightness of our developed core/shell nanophosphors make them

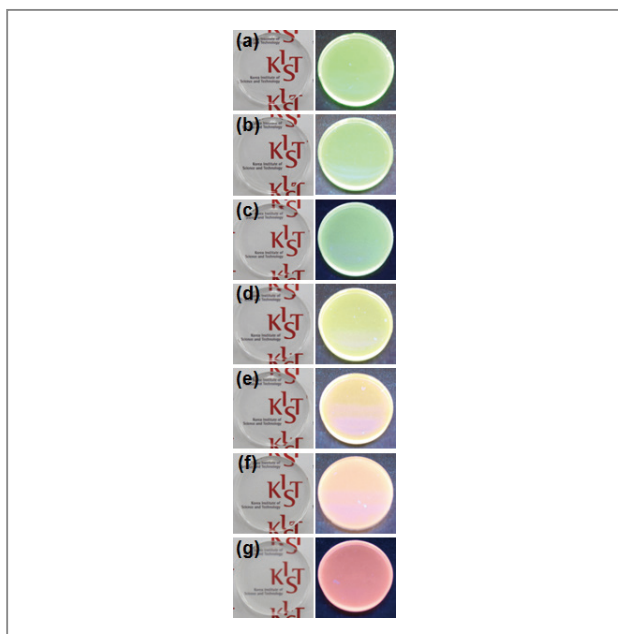


Figure 8. Digital camera images of β -Na(Y,Gd) F_4 :Ce,Tb,Eu/ β -NaYF $_4$ nanophosphor-PDMS composites under room light (top panel) and UV lamp (bottom panel). [(Tb $^{3+}$, Eu $^{3+}$) = a: (15%, 0%), b: (15%, 0.5%), c: (15%, 1%), d: (15%, 2%), e: (15%, 5%), f: (15%, 10%), and g: (0%, 5%).

promising materials for transparent display applications. To investigate the feasibility of their application to transparent three dimensional (3D) volumetric displays, ultra-small β -Na(Y,Gd) F_4 :Ce,Tb,Eu/ β -NaYF $_4$ nanophosphors were incorporated into PDMS polymer. As shown in **Figure 8**, the prepared core/shell nanophosphor-PDMS composites are highly transparent. The ultra-small size of the phosphors minimized light scattering, and the high brightness of the core/shell nanophosphors enabled small quantities of the nanophosphors to be mixed with PDMS to attain the brightness needed for the application. Like the multicolor-emitting β -Na(Y,Gd) F_4 :Ce,Tb,Eu/ β -NaYF $_4$ nanophosphor solutions, the core/shell nanophosphor-PDMS composites also showed multicolor emission from green to red under single wavelength excitation. As seen in the photographs in **Figure 8**, luminescence of the core/shell nanophosphor-PDMS composites were highly uniform, indicating that the core/shell nanophosphors were well dispersed and very uniformly distributed in the composites.

Conclusion

Bright multicolor-tuning was realized by co-doping Ce, Tb, Eu into β -Na(Y,Gd) F_4 nanocrystals. Through absorption of excitation energy by Ce $^{3+}$ ions and energy transfer from Ce $^{3+}$ to Tb $^{3+}$ and Eu $^{3+}$ via Gd $^{3+}$, β -Na(Y,Gd) F_4 :Ce,Tb,Eu nanophosphors showed multicolor emission from green to red under single wavelength excitation. They emitted green, yellowish-green, yellow, orange, scarlet, and red light with varying Tb $^{3+}$ and Eu $^{3+}$ concentrations. By simply adjusting reaction temperature, multicolor-tunable ultra-small β -Na(Y,Gd) F_4 :Ce,Tb,Eu nanophosphors with a sub-6 nm size were successfully synthesized. However, significantly increased surface area to volume ratio of the ultra-small β -Na(Y,Gd) F_4 :Ce,Tb,Eu nanophosphors resulted in significantly decreased PL intensities. Inorganic β -NaYF $_4$ shells on β -Na(Y,Gd) F_4 :Ce,Tb,Eu cores enhanced PL intensities of the ultra-small nanophosphor cores. Thanks to their ultra-small size and high brightness, highly transparent β -Na(Y,Gd) F_4 :Ce,Tb,Eu/ β -NaYF $_4$ -PDMS composites were prepared which also displayed multicolor emission from green to red light under single wavelength excitation.

Note

This article and its images are drawn from “Highly bright multicolor tunable ultra-small β -Na(Y,Gd) F_4 :Ce,Tb,Eu/ β -NaYF $_4$ core/shell nanocrystals” in *Nanoscale*, vol. 5 (19), pp. 9255-9263.

References

- [1] Feldmann C, Jüstel T, Ronda CR, Schmidt PJ. *Adv. Funct. Mater.* 2003; 13 (7): 511-516.
- [2] Sotiriou GA, Franco D, Poulikakos D, Ferrari A. *Acs Nano* 2012; 6 (5): 3888-3897.

- [3] van der Ende BM, Aarts L, Meijerink A. *Adv. Mater.* 2009; 21 (30): 3073-3077.
- [4] Wu S, Han G, Milliron DJ, Aloni S, Altoe V, Talapin DV, Cohen BE, Schuck PJ. *Proc. Natl. Acad. Sci. U.S.A.* 2009; 106 (27): 10917-10921.
- [5] Wang F, Xue X, Liu X. *Angew. Chem. Int. Ed.* 2008; 47 (5): 906-909.
- [6] Dabbousi BO, Rodriguez-Viejo J, Mikulec FV, Heine JR, Mattoussi H, Ober R, Jensen KF, Bawendi MG. *J. Phys. Chem. B* 1997; 101 (46): 9463-9475.
- [7] Blasse G, Grabmaier BC, *Luminescent Materials*. Springer: Berlin, 1994.
- [8] Zhang F, Shi Q, Zhang Y, Shi Y, Ding K, Zhao D, Stucky GD. *Adv. Mater.* 2011; 23 (33): 3775-3779.
- [9] Podhorodecki A, Banski M, Misiewicz J, Afzaal M, O'Brien P, Cha D, Wang XB. *J. Mater. Chem.* 2012; 22 (12): 5356-5361.
- [10] Caldiño U, Álvarez E, Speghini A, Bettinelli M. *J. Lumin.* 2013; 135 (0): 216-220.
- [11] Ptacek P, Schäfer H, Kömpe K, Haase M. *Adv. Funct. Mater.* 2007; 17 (18): 3843-3848.
- [12] Dexter DL. *J. Chem. Phys.* 1953; 21 (5): 836-850.
- [13] Han H, Di Francesco G, Maye MM. *J. Phys. Chem. C* 2010; 114 (45): 19270-19277.
- [14] Kömpe K, Borchert H, Storz J, Lobo A, Adam S, Möller T, Haase M. *Angew. Chem. Int. Ed.* 2003; 42 (44): 5513-5516.
- [15] Bühler G, Feldmann C. *Angew. Chem. Int. Ed.* 2006; 45 (29): 4864-4867.
- [16] Manna L, Scher EC, Li L-S, Alivisatos AP. *J. Am. Chem. Soc.* 2002; 124 (24): 7136-7145.



[Feature Articles]

Using Nanoionics in Artificial Neuron Devices



Doo Seok Jeong

Electronic Materials Research Center
dsjeong@kist.re.kr

Introduction

In general, ionics refers to the study of electrolytes, in which the movement of ions triggers electrochemical reactions. Even narrowing the scope of ionics to include only solid-state ionic materials, the applications associated with ionic processes are still very versatile, mostly involving energy-oriented applications such as solid-state fuel cells, rechargeable batteries, and gas sensors. Recent research in nanoelectronics has clearly demonstrated possible uses of solid-state ionic materials in nanoelectronic devices, in particular, nonvolatile memories. For instance, resistive random access memory (RRAM) and electrochemical metallization (ECM) cells are prototypical types of ionic material-employing emerging nanoelectronic devices [1-3]. Utilizing ionic in addition to electronic behaviors enables a greater degree of versatility, so that new functionalities can be realized.

As the name “nanoelectronic” implies, the physical dimensions of the ionic materials in use are reduced to a few tens of nanometers. From a conventional point of view, such small dimensions lead to “unusual” ionic behaviors that must be distinguished from mainstream ionics. Thus, study of such small-dimension ionic materials is referred to as nanoionics. Note that the ionic materials used in nanoelectronics cover not only electrolytes but also mixed ionic-electronic conductors (MIEC), in which both ionic and electronic carriers co-exist [1]. In MIECs, ionic and electronic behaviors influence each other; they can control each other to some extent, thereby

introducing new functionalities such as analogue-type memory effect.

Nowadays, biologically-inspired analog-type computing systems, so-called “neuromorphic” systems, are being investigated in terms of new physical concepts. Neuromorphic systems refer to electronic systems that can process and store information in similar ways to mammalian brains. Realization of such systems requires artificial neural networks that are complex networks composed of artificial neuron and synapse devices. Indeed, neurons and synapses are basic building blocks of the mammalian brain. In particular, artificial neuron devices can play important roles in signalling, generation and calculation [4]. Attempts to realize artificial neuron devices have been made over the last few decades using conventional technology, such as complementary metal-oxide-semiconductor (CMOS) technology. However, given that this conventional technology is rife with problems, such as high production costs, limits of scale, and circuit complexity, a new approach to the development of artificial neuron devices has recently been suggested based on the use of functional materials rather than circuit design [4]. Recently, several functional materials, including MIECs, amorphous chalcogenides and ECM materials, have been investigated in capacitor-type two-terminal artificial synapse devices [4].

This study focuses on TiO_2 MIEC, which is a prototypical material for RRAM applications, and attempts to understand its MIEC behaviour. In addition, the feasibility of using MIEC behaviour in artificial neuron devices is demonstrated.

Research details

A schematic diagram of our fabricated Pt/MIEC/Pt junction sample is illustrated in the top left inset of Figure 1. Since the fabricated cells are capacitor-shaped and believed to involve no redox reaction in the chosen voltage range, they are non-faradaic capacitors. Consecutive

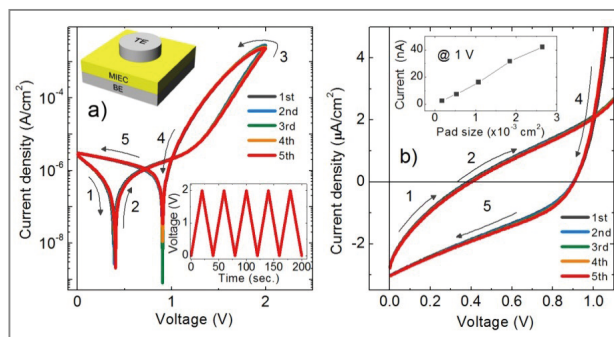


Figure 1. (a) Consecutive J-V loops, except the first-cycle loop, of the Pt/ TiO_2 /Pt capacitor under the applied voltage cycles shown in the bottom right inset. (b) J-V curves re-plotted on a linear scale. The inset denotes current values of the capacitors with five different pad-sizes at 1V.

current density – voltage (J – V) loops of the Pt/ TiO_2 /Pt capacitor, are plotted in Figure 1(a), measured by applying triangle-shaped voltage pulses at a voltage sweep rate of 0.1 V/s. The applied voltage pulses are shown in the bottom right inset of Figure 1(a). The J-V loops represent reproducible “clockwise” (CW) hysteresis with reverse current flow (current flow in the opposite direction to the applied voltage) as can be more clearly seen in Figure 1(b). However, in the high voltage region, the J-V loci exhibit “counterclockwise” (CCW) hysteresis. Thus, the J-V loops show both CW and CCW hysteresis behaviors, crossing each other at a specific voltage (ca. 1 V).

For a quantitative understanding of the J-V hysteresis behavior, the numerical calculation of J-V behaviour for a one-dimensional electrode/MIEC/electrode non-faradaic capacitor was performed. In a non-faradaic capacitor, the interface between the MIEC and the electrode forms a blocking contact for oxygen vacancies so that their quantity can be maintained within the capacitor. Time-dependent dc ionic conduction was calculated using the drift-diffusion equation and Fick’s second law with blocking contact boundary conditions. For dc electronic conduction, the drift-diffusion of electrons, i.e., band conduction, was taken as their conduction mechanism. The band offset at the interface, varying on the electric field assigned to the Helmholtz layer, was employed as

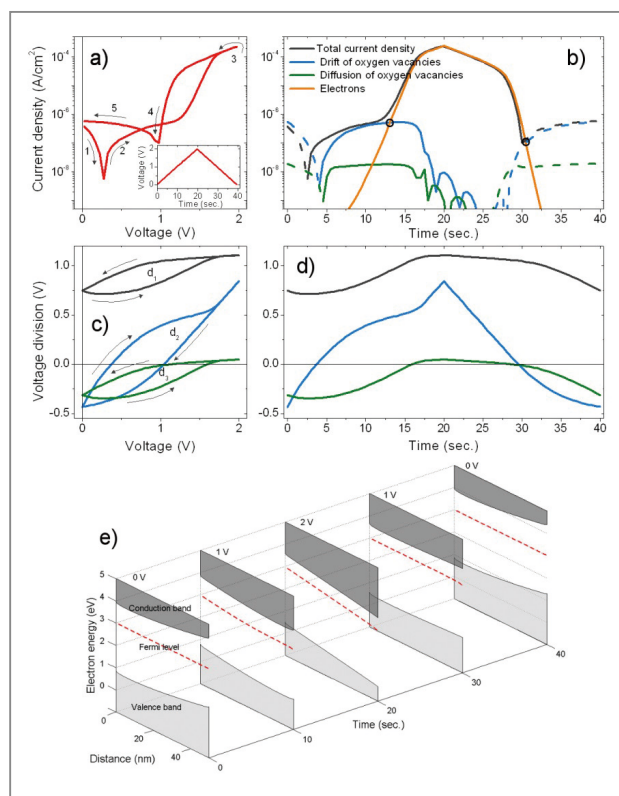


Figure 2. (a) Calculated J-V loop under the voltage-time profile shown in the inset. (b) At the center of TiO_2 in the model system, the contribution of each component, e.g., drift and diffusion of oxygen vacancies, and dc electronic conduction, to the total current density is plotted. The solid and dashed lines denote positive and negative current density, respectively. The circles indicate transitions between ionic and electronic conduction. The voltages assigned to the left Helmholtz layer (cathode), the MIEC, and the right Helmholtz layer (anode) are plotted, respectively, with respect to (c) the applied voltage and (d) time. (e) The calculated electron band profiles with time are shown.

the boundary conditions. A quasi-static approximation was employed to simplify this calculation in a time domain. Considering the large diffusion coefficient difference between electron and oxygen vacancy, the use of this approximation is reasonable. Finally, total current, including the aforementioned dc current and displacement current, was evaluated as a function of time and voltage.

The calculated J-V hysteresis loop at a voltage sweep rate of 0.1 V/s is plotted in Figure 2(a). The parameters used for this calculation are listed in Table 1, which, in fact, gave the best fitting results. The J-V loop was taken from consecutive J-V loops, except the first-cycle loop,

and thus the initial conditions, such as distributions of oxygen vacancies, electrons, and galvanic potential in the MIEC, were not in equilibrium. However, the initial conditions of the first-cycle loop calculation were always in equilibrium so that the calculated loop started from zero current. The calculated J-V loop is found to be in good agreement with the experimental J-V loops shown in Figure 1(a), exhibiting CW and CCW hysteresis behaviors and crossing at approximately 1 V. The calculated current density is attributed to four major contributions: drift and diffusion of oxygen vacancies, displacement current, and dc electronic conduction. The first three contributions are position-dependent. The center point of the model system (at a distance of 25 nm from the left (right) interface), where the contribution of displacement current is at a minimum, was taken for the results shown in Figure 2(b), so that the dc ionic conduction behaviour can be clearly shown. The contributions of dc ionic and electronic conduction are separately plotted in Figure 2(b) as a function of time, so that their contributions to the total current at given times can be seen.

In Figure 2(b), it is observed that the CCW hysteresis in the high voltage region ($> \sim 1\text{V}$, which corresponds to $\sim 12 - 30\text{ s}$) is attributed to dc electronic conduction rather than ionic current, whereas the CW hysteresis in the low V region is mainly due to ionic current. Therefore, the experimental CCW hysteresis is most likely of dc electronic current, and thus the hysteresis implies “resistance” hysteresis. In contrast, the CW hysteresis in the low voltage region does not signify hysteretic resistance because the current in that case is not of dc electronic conduction. In the low voltage region, the contribution of dc electronic current is negligible, as can be seen in Figure 2(b).

The electric conduction behaviour of the $\text{Pt/TiO}_2/\text{Pt}$ capacitor was further investigated by applying square-shaped voltage pulses. The width of voltage pulses varied from sub-ms to 100 ms. By utilizing a voltage divider, the response current was converted into response voltage, i.e., output voltage V_{out} . In this manner, the output

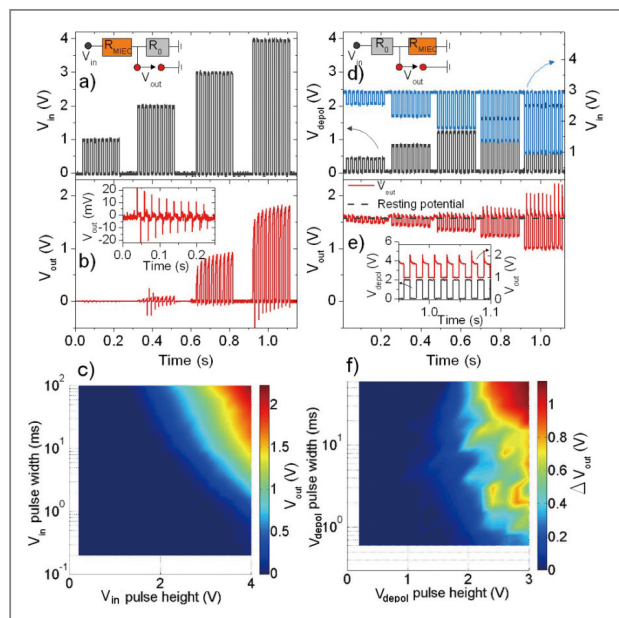


Figure 3. (a) Square-shaped voltage pulses applied to the circuit depicted in the inset for observing polarization-induced voltage-spike firing. (b) Resulting V_{out} pulses. An enlarged V_{out} pattern in the time period 0 – 0.25 s is plotted in the inset. (c) A V_{out} map against V_{pol} (V_{in}) pulse height and width. (d) V_{depol} pulses and the net V_{in} pattern, applied to the circuit shown in the inset, for depolarization-induced voltage-spike firing. (e) Resulting V_{out} pulses. The V_{depol} and V_{out} profiles in the time period 0.95 – 1.1 s are plotted in the inset. (f) A map of ΔV_{out} , against V_{depol} pulse height and width.

voltage responding to the input voltage V_{in} pulses was evaluated. Two different schemes of voltage application were employed: i) polarization voltage V_{pol} pulses with a background dc voltage of zero, i.e., $V_{in}=V_{pol}$, and ii) depolarization voltage V_{depol} pulses superimposed on a background dc V_{pol} , i.e., $V_{in}=V_{pol}-V_{depol}$. In the former case, the used circuit diagram is shown in the inset of Figure 3(a). A voltage divider R_0 (1 kohms) was connected in series to the Pt/TiO₂/Pt capacitor R_{MIEC} . Figures 3(a) and (b) show the square-shaped input voltage pulses, four different heights (1, 2, 3, and 4 V) and a 10 ms pulse width, and the output voltage pulses, respectively. The abrupt increase in the output voltage with the input voltage is shown in Figure 3(b), suggesting that voltage spikes are generated, i.e., voltage spike firing, relying on the magnitude of external stimulation. Figure 3(c) shows

output voltage with respect to input voltage pulse height (0.2 – 4 V) and width (0.2 – 100 ms). In the figure, it is apparent that increasing the input voltage pulse width leads to a decrease in the height required for a particular output voltage. This implies that the voltage spike firing is a function of at least two independent variables, i.e., voltage and time. Thus, the aforementioned magnitude of external stimulation should include the quantities of these two variables. In fact, it was found that input voltage pulses of a 4 V height and a 100 ms resulted in the largest output voltage spike.

In the latter case, i.e., application of V_{depol} pulses superimposed on a background dc V_{pol} , the employed circuit diagram is depicted in the inset of Figure 3(d). In the circuit, a voltage divider (also 1 kohms) was ahead of the capacitor. A dc V_{pol} of 3 V was applied to the circuit and V_{depol} pulses of different heights (0.4, 0.8, 1.2, 1.6, and 2.0 V) and a 10 ms width were superimposed on the V_{pol} . The V_{depol} pulses and consequent V_{in} pattern, i.e., $V_{pol}-V_{depol}$, are plotted in Figure 3(d). At a 3 V dc V_{pol} , the V_{out} was approximately 1.6 V, implying that the capacitor's resistance becomes comparable to that of the voltage divider (1 kohms) at the given V_{in} . In this study, this output voltage is termed as “resting potential.”

The present study is an example showing how nanoionic materials can be utilized in artificial neuron devices. This new approach to the realization of artificial brain devices potentially opens up alternate avenues for achieving this ambitious goal. From a materials perspective, it is imperative to build a better understanding of nanoionic material properties so that these materials can best be applied in artificial brain devices. The present theoretical and experimental work marks one step toward the achievement of this goal.

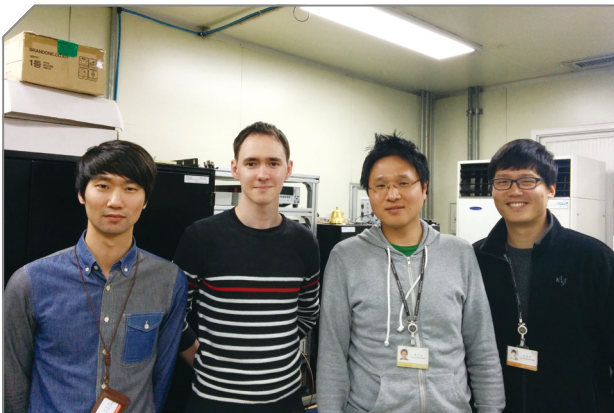
Note

This article and images were drawn from “Elastic resistance change and action potential generation of non-

faradaic Pt/TiO₂/Pt capacitors” in *Nanoscale*, Vol. 5, pp. 6363-6371.

References

- [1] Jeong DS, Thomas R, Katiyar RS, Scott JF, Kohlstedt H, Petraru A, Hwang CS. *Reports on Progress in Physics* 2012; 75: 076502.
- [2] Lu W, Jeong DS, Kozicki MN, Waser R. *MRS Bulletin* 2012; 37: 124-130.
- [3] Waser R, Dittmann R, Staikov G, Szot K. *Adv. Mater.* 2009; 21: 2632-2663.
- [4] Jeong DS, Kim I, Ziegler M, Kohlstedt H. *RSC Advances* 2013; 3: 3169-3183.



Neuromorphic System Laboratory /
Electronic Materials Research Center

[Technical Review]

Solution-Processed High Band-Gap CuInGaS_2 Thin Film for Solar Cell Applications



Se Jin Park

Clean Energy Research Center
sejin@kist.re.kr



Byoung Koun Min

Clean Energy Research Center
bkmin@kist.re.kr

Introduction

Photovoltaic (PV) devices have been spotlighted as ultimate energy generation technology because they can convert freely available sunlight to electricity. Unfortunately, their relatively low energy conversion efficiency (compared to fossil fuel) and expensive module costs have hampered the widespread use of PV devices as an energy source. Considering these limitations, many materials, both organic and inorganic, have been suggested for low-cost, high-efficiency solar cells. Among them, $\text{CuIn}_x\text{Ga}_{1-x}\text{S}_y\text{Se}_{1-y}$ (CIGSSe) is one of the most promising candidates because of its high absorption coefficient, tunable band-gap and stable structure. Because of these favorable characteristics, CIGSSe can facilitate the production of a highly efficient solar cell (~20%) with a thin (~2 μm) absorber film, which is much more cost-efficient than a silicon film which requires a thickness of ~100 μm when used as an absorber layer [1, 2]. In addition, the ability to tune band-gap from 1.0 eV to 2.4 eV by controlling the composition of the material is potentially useful for applications involving tandem solar cell architecture, a structure which can surpass the efficiency of a single junction solar cell [3].

In general, CIGSSe thin films have been fabricated by vacuum processes such as co-evaporation and sputtering techniques. Although these processes result in high-efficiency solar cells, they are still not ideal for commercial application due to high costs associated with maintenance

of vacuum equipment, a significant loss of resource materials, and technical restrictions in large-scale production. In order to fabricate CIGSSe thin film more effectively, solution-based printing methods have been developed in recent years [4, 5].

Solution-based CIGSSe thin film preparation is generally conducted via (1) ink (or paste) preparation, (2) coating, and (3) heat treatment. Ink preparation can be roughly categorized in two ways: a nanoparticles method using synthesized CIGSSe, or a CIG oxide nanoparticles and precursor solution method consisting of metal nitrates, chlorides, acetates, or binary compounds (e.g., Cu_2S , In_2Se_3 , and Ga_2Se_3) directly dissolved in an organic solvent [6-11]. Some organic binders and/or additives are commonly added to create a suitable viscosity of the nanoparticle or precursor solution [12, 13]. These organic materials offer important advantages in terms of easier handling and maintenance of the solution; on the other hand, they may also be a problem by acting as impurities. Their carbon residue is a particular issue because it prevents grain growth and increases series resistance which decreases the efficiency of the solar cell [14]. The porous and/or nonuniform morphology, frequently formed in the heat-treatment step for grain growth and alloy formation, can also have negative effects on solar cell performance [15].

In this study, we suggest a precursor solution-based method for the preparation of high band-gap CuInGaS_2 (CIGS) thin film with a two-step heat treatment. When considering the optimum band-gap for maximum theoretical efficiency which is about 1.4 eV and in the top cell of tandem configuration, a high band-gap CIGS is required [16, 17]. Additionally, the higher voltage that can be achieved with high band-gap is desirable in solar cell modules because the series resistances that deteriorate performance can be reduced [3]. Therefore, we fabricated high band-gap film by substitution of In and Se with Ga and S, respectively.

Our CIGS film showed a densely packed morphology which was achieved by two-step heat treatment. The first

step involved an oxidation process to make a mixed oxide layer of Cu, In, and Ga with the elimination of carbon residue, and the second was a sulfurization process to form the CIGS alloy. Although the film showed a rough surface due to the Ga deficient composition, the device having the film resulted in high power efficiency and high open circuit voltage (V_{oc}) due to the high band-gap of the absorber layer. Furthermore, our approach to the development of solution-based CIGS has more potential for commercialization than other solution processes because most procedures, including paste preparation and film deposition, are conducted in open air not in restricted conditions (e.g., in a glove box).

Research details

The process of CIGS thin film fabrication is illustrated in Figure 1. To make CIGS film with a high band-gap, the elemental substitution of In and Se with Ga and S was considered in a precursor solution-synthesis step and a heat-treatment step. A paste with a composition ratio of 1:0.7:0.3 (Cu/In/Ga) was spin-casted onto a substrate. To achieve $\sim 1.2 \mu\text{m}$ thickness, the coating and drying step was repeated six times. The film was then annealed at 300°C under ambient conditions. This temperature was chosen to remove carbon residues from the organic solvent and/or binder material on the basis of our thermal gravimetric analysis as well as to minimize possible oxidation of the Mo layer of the glass substrate.

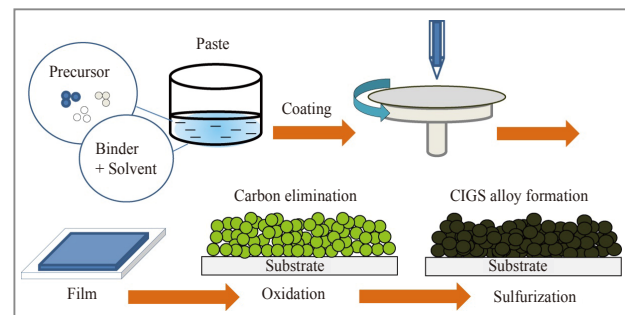


Figure 1. Schematic illustration of the CIGS thin film fabrication process.

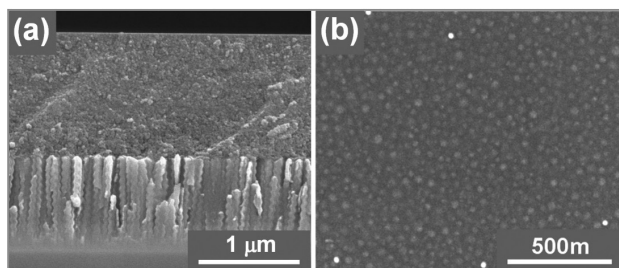


Figure 2. SEM images of Cu, In, and Ga mixed oxide films (a) cross-sectional and (b) top view.

Notably, the amount of carbon residue was measured to be around the accuracy limit (~ 3 at.%) of our electron probe micro analyzer (EPMA) analysis. The formation of only amorphous states of the mixed oxide was confirmed by X-ray diffraction (XRD), where no apparent peaks appeared. The film also showed a densely packed film morphology, as seen in Figure 2.

To synthesize the CIGS alloy film, the mixed oxide film consisting of Cu, In and Ga was reacted with dilute H_2S gas ($\text{H}_2\text{S}(1\%)/\text{N}_2$) at 500°C . As oxygen in the film was completely substituted with S, the film crystallinity and morphology changed significantly. The XRD pattern showed a peak at 28.0° 2θ , with weak peaks at 32.5° , 46.6° , and 55.3° 2θ (Figure 3a). The most intense peak, at 28.0° 2θ , indicates a polycrystalline CIGS alloy with a (112) orientation. The other prominent peaks correspond to the (204)/(220) and (116)/(312) phases. The presence of these peaks clearly indicates the polycrystalline chalcopyrite structure of CIGS, which is in agreement with a JCPDS #27-0159 as well as other reported values [18].

The morphology of CIGS was also investigated by scanning electron microscopy (SEM). As can be seen in Figure 3, a densely packed morphology with very low porosity was maintained with particle growth from 10nm to 70nm even after sulfurization. Interestingly, however, the large crystallites on the surface appeared in the top view of the SEM image (Figure 3d). The composition of some areas showing different morphology was analyzed by SEM energy-dispersive X-ray spectroscopy (EDX). The bulk area marked by 1 and 2 in Figure 3 showed a

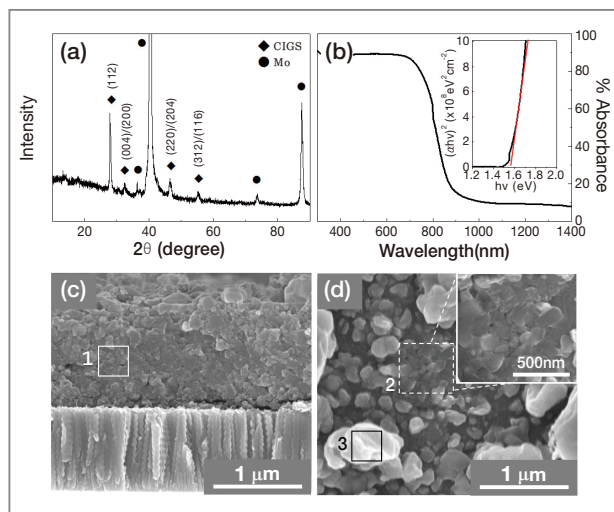


Figure 3. XRD patterns (a) and absorbance (b), and typical cross-sectional (c) and top-view (d) SEM images of the CIGS thin film obtained after sulfurization. The inset of (b) is a plot of $(ahv)^2$ versus hv for evaluating the band-gap. The boxes (marked by 1, 2, and 3) in (c) and (d) indicate the areas where EDX analyses were carried out, and the inset in (d) is an enlarged SEM image corresponding to area 2.

similar stoichiometric composition ratio 1:0.7:0.3:2 to the intended ratio. However, large crystallites showed a relative In-rich, Ga-poor atomic ratio (Table 1). To elucidate the nature of the large crystallites, additional analysis was performed by Auger electron spectroscopy (AES) and EPMA. The composition distribution with respect to the film depth was investigated by Auger depth profiling. Compared to the SEM image, the bulk region of 500nm to 1500nm showed a uniform distribution of Cu, In, and S concentrations toward the Mo back contact (Figure 4a). However, a significantly lower Ga content was found concomitantly with a higher In content at the upper part of the film up to a film depth of ~ 500 nm, implying that the large crystallites can possibly be attributed to the formation of a Ga-poor (or In-rich) phase which is well matched to the above SEM EDX results. Consistently, mapping analysis of EPMA for an area where large crystallites exist clearly showed the Ga-poor and In-rich composition feature, as can be seen in Figure 4b. Notably, these crystallites are not binary compounds such as CuS_2 because they remain even after the potassium cyanide

Table 1. Composition ratio of the local area of the CIGS film obtained by EDX and EPMA

Analytical method	Area	Atomic ratio			
		Cu	In	Ga	S
EDX	1	1.00	0.75 ± 0.03	0.31 ± 0.05	2.17 ± 0.20
EDX	2	1.00	0.75 ± 0.04	0.29 ± 0.03	2.07 ± 0.10
EDX	3	1.00	0.99 ± 0.05	0.07 ± 0.02	2.13 ± 0.10
EPMA		1.00	0.78 ± 0.05	0.18 ± 0.02	1.91 ± 0.05

* The atomic ratios were obtained by normalizing each atomic concentration with respect to Cu

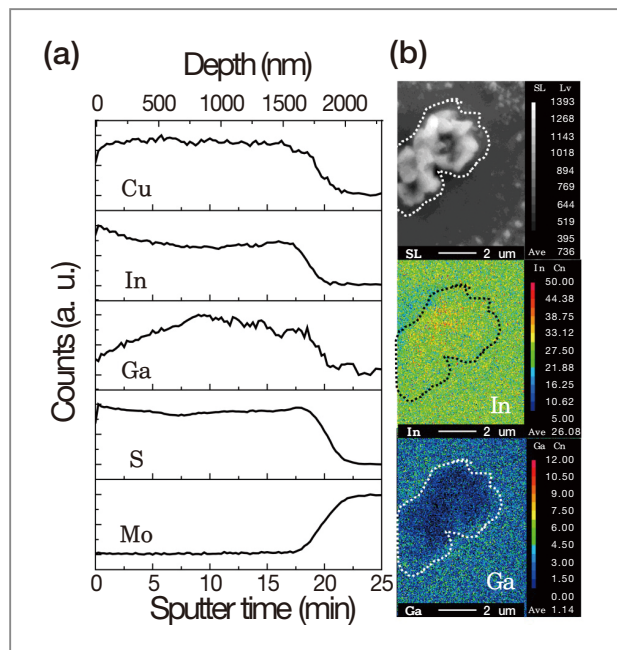


Figure 4. (a) The composition profile with respect to the CIGS film depth obtained by Auger depth profiling. (b) EPMA mapping of the surface area where a large crystalline exists on the CIGS film.

leaching treatment.

The optical property was investigated using ultraviolet-visible (UV-Vis) absorption spectroscopy. As can be seen in [Figure 3b](#), absorption was evident below 900nm. The band-gap can be estimated from the relation of $(\alpha hv)^m$ vs. hv where α is the absorption coefficient, hv is photon energy and $m=2$ (this constant can only be applied for direct band-gap material) [19]. The absorption coefficient was calculated by the following equation.

$$\alpha = \frac{1}{d} \ln \left\{ \frac{(1-R)^2}{2T} + \sqrt{\left[\frac{(1-R)^2}{2T} \right]^2 + R^2} \right\}$$

Here, T is transmittance, R is reflectance, and d is sample thickness. The estimated direct optical band-gap of the film is found to be 1.57 ± 0.02 eV as shown in the inset of [Figure 3b](#). Because the Se was replaced by S, with a much bigger unit cell lattice, the band-gap showed a higher value than CIGSSe film in general (~ 1.1 eV) [20].

Finally, a solar cell device was constructed using the CIGS film. The conventional structure Mo/CIGS/CdS/i-ZnO/n-ZnO/Ni/Al and general deposition method was applied to fabricate the device, except for the CIGS layer. The current density-voltage (J - V) characteristics of the devices ([Figure 5a](#)) revealed the highest efficiency of 8.28% with an open circuit voltage (V_{oc}), short circuit current density (J_{sc}), and fill factor of 787 mV 17.0 mA/cm², and 61.9%, respectively. The incident photon conversion efficiency (IPCE) data ([Figure 5b](#)) showed that the photocurrent was generated below a 840nm wavelength, a result which is well matched with the absorbance spectra of the CIGS film shown in [Figure 3b](#), implying that the photovoltaic response arises from the CIGS film. The band-gap can also be calculated from the IPCE data such that the absorption coefficient follows the relation of $\alpha = -\ln(1 - IPCE)$ [21]. The band-gap of 1.53 ± 0.02 eV obtained from the IPCE data is consistent with the results from the absorbance data as well as the photoluminescence data (1.55 eV).

Despite its rough surface morphology, the device

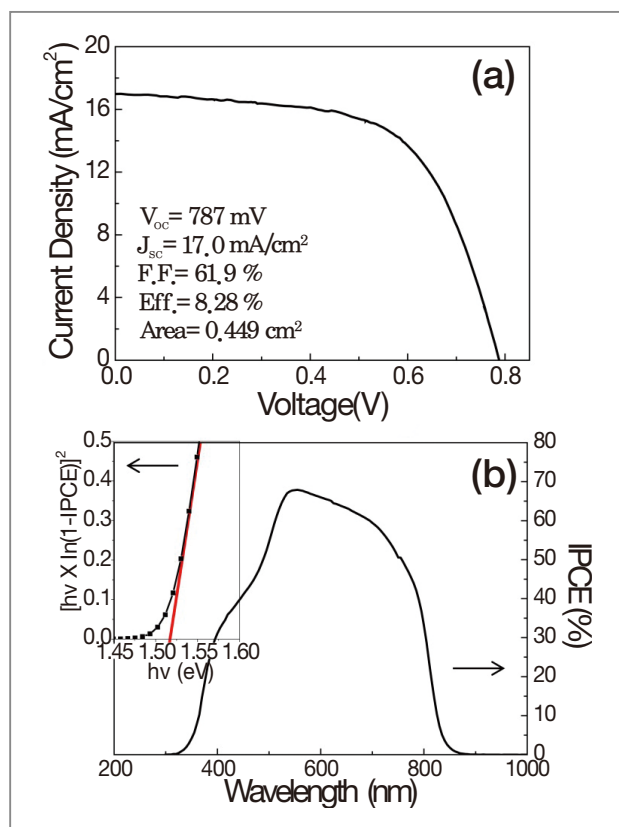


Figure 5. (a) The current density-voltage characteristics. (b) IPCE spectrum of the CIGS solar cell device. The inset in (b) is a plot of $(\alpha hv)^2$ versus $h\nu$ for evaluating the band-gap using IPCE data.

showed high efficiency with the high band-gap CIGS film. We inferred that this efficiency resulted from an extremely low degree of porosity of the CIGS absorber

film. To verify this, porous CIGS film with a smoother surface morphology was prepared by almost the same fabrication procedure, except the organic binder material used in the paste preparation was ethyl cellulose instead of polyvinyl acetate (PVA). Although we do not know the detailed incorporation mechanism of binders in thin film synthesis, we could observe significantly different surface morphologies of the mixed oxide as well as the sulfurized films as compared to films synthesized by paste made with PVA (Figure 6). The solar cell device with the porous CIGS film showed less than 2% solar cell efficiency with very low V_{oc} , implying the presence of shunt paths originated from the high porosity of the film. On the basis of our observations, we were able to conclude that the porosity of the film is a more important factor than surface roughness in photovoltaic performance.

We also compared the solar cell performance of our CIGS thin film with other representative CIGSSe thin film solar cell records listed in Table 2. The highest solar cell efficiency (20.3%) with a V_{oc} of 740 mV was attained using a CIGSSe film that was made by the co-evaporation method; its band-gap was 1.14 eV [2]. Meanwhile, the CIGSSe thin film solar cells with a high band-gap (>1.5 eV) generally show much lower efficiency than those with low band-gap. For example, only sulfurized film (CIGS) exhibited the highest efficiency of 12.9% even though a vacuum-based deposition method (e.g., sputtering) was applied to CIGS film preparation [22]. Furthermore,

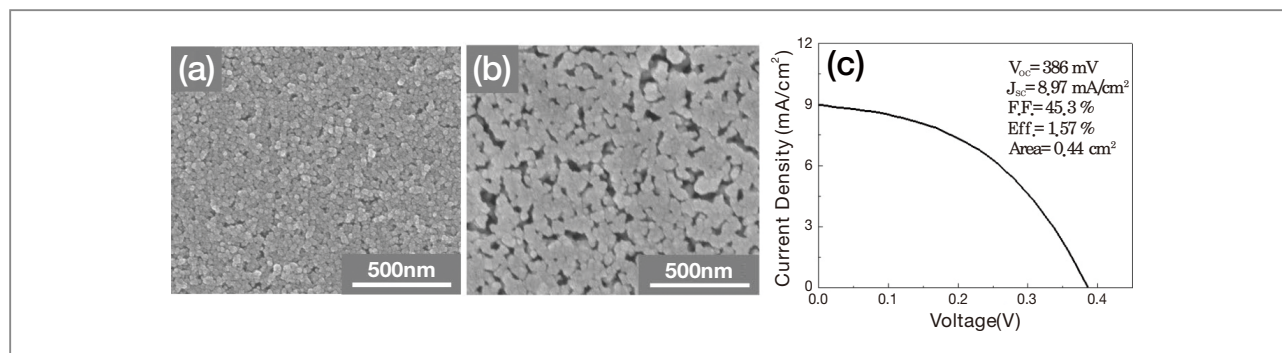


Figure 6. (a) Top-view SEM image of the mixed oxide film prepared with paste using ethyl cellulose as a binder material. (b) Top-view image after sulfurization. (c) The current density-voltage characteristics of the solar cell device fabricated with the CIGS film shown in (b).

Table 2. List of preparation method, band-gap of absorber layer, V_{oc} , and efficiency of representative CIGSSe thin film solar cells

Process	Deposition method	Absorber layer	Band-gap (eV)	V_{oc} (mV)	Eff. (%)	Ref.
Vacuum process	Co-evaporation	CIGSe ₂	1.14	740	20.3	2
	Sputtering	CIGS ₂	1.53	835	12.9	22
	Evaporation	CIGS ₂	1.53	776	12.3	23
Solution process	Nanoparticles	CIGSSe ₂	1.2	630	12.0	7
	Nanoparticles	CIGSe ₂	-	520	13.6	9
	Nanoparticles	CISE ₂	1.0	440	8.2	24
	Precursor solution	CIGSSe ₂	1.16	623	15.2	8
	Precursor solution	CIGSe ₂	1.13	525	8.01	25
	Precursor solution	CIGSe ₂	1.05	419	7.3	26
	Precursor solution	CIS ₂	-	320	2.15	27
	Precursor solution[*]	CIGS ₂	1.55	787	8.28	-

* Result of this study

based on our literature survey, there are few examples of solution-processed high band-gap (>1.5 eV) CIGS solar cells with efficiency comparable to that of low band-gap CIGSe solar cells, as can be seen in the data in Table 2. Our result is the first demonstration of a highly efficient and low-cost solution-processed high band-gap (>1.5 eV) CIGS thin film solar cell.

One major problem inherent in solution-processed CIGSSe solar cells is the low V_{oc} . In general, a V_{oc} drop arises from the recombination processes in solar cells. As can be seen in Table 2, the gap of V_{oc} between the solution-processed and the vacuum-processed CIGSSe thin film solar cells is very large (mostly over 200 mV) even though the same device configuration and deposition methods for each layer were applied, except for the preparation of the CIGSSe absorber layer. However, our device showed a V_{oc} of 787 mV, which is even higher than the best one made by the evaporation method (776 mV) [23], and 48~92 mV lower than the world record for a vacuum-based CIGS solar cell with a similar band-gap CIGS absorber (1.53 eV) [18, 22]. The relatively high V_{oc} of our solar cell device may result from diminishing the recombination processes due to a very densely packed morphology (preventing short-circuiting and therefore minimizing leak current) as well as a very low carbon

contamination (minimizing recombination centers from impurities) of the CIGS thin film.

Note

This article and its images are drawn from "Solution processed high-band-gap CuInGaS₂ thin film for solar cell applications" in *Prog. Photovolt: Res. Appl.* 2014 Vol. 22(1), pp. 122~128.

References

- [1] Hegedus S. *Prog Photovoltaics* 2006; 14: 393-411.
- [2] Jackson P, Hariskos D, Lotter E, Paetel S, Wuerz R, Menner R, Wischmann W, Powalla M. *Prog Photovoltaics* 2011; 19: 894-897.
- [3] Siebentritt S. *Thin Solid Films* 2002; 403: 1-8.
- [4] Hibberd CJ, Chassaing E, Liu W, Mitzi DB, Lincot D, Tiwari AN. *Prog Photovoltaics* 2010; 18: 434-452.
- [5] Habas SE, Platt HAS, van Hest M, Ginley DS. *Chem Rev.* 2010; 110: 6571-6594.
- [6] Akhavan VA, Goodfellow BW, Panthani MG, Reid DK, Hellesbusch DJ, Adachi T, Korgel BA. *Energ Environ Sci.* 2010;

- 3: 1600-1606.
- [7] Guo Q, Ford GM, Agrawal R, Hillhouse HW. *Prog Photovoltaics* 2013; 21: 64-71.
- [8] Todorov TK, Gunawan O, Gokmen T, Mitzi DB. *Prog Photovoltaics* 2013; 21: 82-87.
- [9] Kapur VK, Bansal A, Le P, Asensio Ol. *Thin Solid Films* 2003; 431-432: 53-57.
- [10] Akhavan VA, Goodfellow BW, Panthani MG, Steinhagen C, Harvey TB, Stolle CJ, Korgel BA. *J Solid State Chem.* 2012; 189: 2-12.
- [11] Lee JH, Chang J, Cha JH, Lee Y, Han JE, Jung DY, Choi EC, Hong B. *Eur J Inorg Chem.* 2011: 647-651.
- [12] Ahn S, Kim K, Cho A, Gwak J, Yun JH, Shin K, Ahn S, Yoon K. *Acs Appl Mater Inter.* 2012; 4: 1530-1536.
- [13] Todorov T, Mitzi DB. *Eur J Inorg Chem.* 2010: 17-28.
- [14] Ahn S, Kim C, Yun JH, Gwak J, Jeong S, Ryu B-H, Yoon K. *J Phys Chem C.* 2010; 114: 8108-8113.
- [15] Uhl AR, Romanyuk YE, Tiwari AN. *Thin Solid Films* 2011; 519: 7259-7263.
- [16] Shah A, Torres P, Tscharnner R, Wyrsh N, Keppner H. *Science* 1999; 285: 692-698.
- [17] Young DL, Abushama J, Noufi R, Xiaonan L, Keane J, Gesert TA, Ward JS, Contreras M, Symko-Davies M, Coutts TJ. *Photovoltaic Specialists Conference, 2002. Conference Record of the Twenty-Ninth IEEE, 19-24 May 2002.* 2002; 608-611.
- [18] Merdes S, Mainz R, Klaer J, Meeder A, Rodriguez-Alvarez H, Schock HW, Lux-Steiner MC, Klenk R. *Sol Energy Mat Sol C.* 2011; 95: 864-869.
- [19] Woo K, Kim Y, Moon J. *Energ Environ Sci.* 2012; 5: 5340-5345.
- [20] Kemell M, Ritala M, Leskela M. *Crit Rev Solid State* 2005; 30: 1-31.
- [21] Hegedus SS, Shafarman WN. *Prog Photovoltaics* 2004; 12: 155-176.
- [22] Merdes S, Abou-Ras D, Mainz R, Klenk R, Lux-Steiner MC, Meeder A, Schock HW, Klaer J. *Prog Photovoltaics* 2013; 21: 88-93.
- [23] Kaigawa R, Neisser A, Klenk R, Lux-Steiner MC. *Thin Solid Films* 2002; 415: 266-271.
- [24] Wang W, Han S-Y, Sung S-J, Kim D-H, Chang C-H. *Phys Chem Chem Phys.* 2012; 14: 11154-11159.
- [25] Jeong S, Lee B-S, Ahn S, Yoon K, Seo Y-H, Choi Y, Ryu B-H. *Energ Environ Sci.* 2012; 5: 7539-7542.
- [26] Uhl AR, Fella C, Chirila A, Kaelin MR, Karvonen L, Weidenkaff A, Borca CN, Grolimund D, Romanyuk YE, Tiwari AN. *Prog Photovoltaics* 2012; 20: 526-533.
- [27] Weil BD, Connor ST, Cui Y. *J Am Chem Soc.* 2010; 132: 6642-6643.



Min's Solar Fuel Group / Clean Energy Research Center

[Feature Articles]

A Bioaerosol Detection Chip Using Inertial Impaction and Mini-fluorescent Microscopy

**Joon Sang Kang**

Center for
Environment,
Health and Welfare
Research
022698@kist.re.kr

**Jae Hee Jung**

Center for
Environment,
Health and Welfare
Research
jaehee@kist.re.kr

**Gwi-Nam Bae**

Center for
Environment,
Health and Welfare
Research
gnbae@kist.re.kr

Introduction

Airborne microorganisms, known as bioaerosols, including viruses, bacteria, and fungal spores, are major components of atmospheric aerosols. Their size distribution ranges from 20 nm to 100 μm . Generally, small bioaerosols (e.g., viruses and bacteria) are suspended in the atmosphere for a long time due to their low settling velocities, leading to an increased possibility of inhaling them into the respiratory system. Thus, it is important to be able to detect pathogenic bioaerosols rapidly and effectively.

To detect atmospheric bioaerosols, it is necessary to identify bioaerosols from two perspectives, size and biological characteristics. Different bioaerosols have different size distributions. For example, *Staphylococcus epidermidis* (*S. epidermidis*; bacterial group) and influenza A H1N1 (viral group) have size distributions of 0.5–2 μm and 0.07–0.5 μm , respectively. Also, non-biological particles, suspended together with bioaerosols in the atmosphere, can have similar size distributions as biological particles.

To detect airborne microorganisms directly, we demonstrated the real-time detection of airborne microorganisms in the air stream. Our system was composed of three major components: an inertial impaction system, a cartridge-type impaction plate, and a mini-fluorescent microscope. An inertial impaction technique was used to separate airborne particles in terms of their aerodynamic diameter. A disposable cartridge-type impaction plate was designed to provide fluorescent staining of the airborne microbes. To

minimize system dimensions – for portability and cost-efficiency – the mini-fluorescent microscope, remodeled from a commercially available webcam, was utilized.

The system showed reasonable performance with both biological and non-biological particles. The cutoff diameter at each impaction stage was 2.24, 0.91, and 0.49 μm , respectively. The fluorescent images for the different experimental conditions showed that the airborne microorganism was stained directly by SYBR green I at the impaction zone. The cost-efficient mini-fluorescent microscope showed excellent resolution for microorganism imaging and detection. A disposable cartridge-type impaction plate was used to prevent saturation of the fluorescent signal and to provide real-time fluorescent staining of the airborne microbes. The fluorescent intensity of the microorganism and PSL particles allowed us to identify microbes from non-biological particles. The proposed device could be used as an early warning system for pathogenic bioaerosols in real time using fluorescence acting on the bioaerosol components, before analyzing the exact properties of the bioaerosol at the DNA level using qualified instruments.

Design of the proposed system

A schematic diagram of the proposed airborne microbe detection chip, which was composed of a main inertial impaction component, a cartridge-type impaction plate, and mini-fluorescent microscope, is shown in Figure 1a. A cutoff diameter that yields a 50% collection efficiency at each impaction stage can be calculated from:

$$d_{50} = \sqrt{\frac{18\mu D_h \text{stk}_{50}}{\rho_p C_c U}}, \quad (1)$$

where μ is the air viscosity, D_h is the hydraulic diameter, ρ_p is the particle density, C_c is the Cunningham slip correction factor, U is the air velocity at the inlet, and stk_{50} denotes the Stokes number that corresponds to 50% particle collection efficiency. Figure 1d shows the main inertial impaction component with three stages,

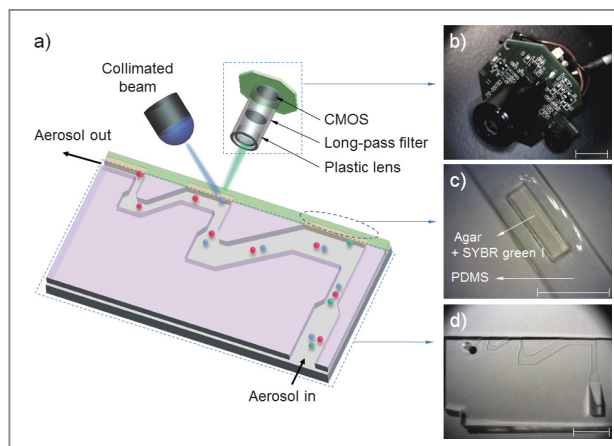


Figure 1. (a) Schematic diagram of the present airborne microbe detection chip. (b) Mini-fluorescent microscope. (c) Disposable cartridge-type PDMS impaction plate with an impaction zone. (d) Microchannel with three impaction stages (all scale bars indicate 1 cm).

fabricated using a conventional soft-lithography process. The sample flow rate and channel height were set to 0.12 L/min and 160 μm , respectively. d_{50} at each stage was 2.02 μm (first stage), 0.88 μm (second stage), and 0.54 μm (third stage), because the target bioaerosol element, *S. epidermidis*, has a size distribution from 0.5 to 2 μm . Relatively large bioaerosols are removed at the first stage, and the target bioaerosols are collapsed and detected at the second and third stages. By adjusting the design parameters, bioaerosols with specific diameters can be collapsed and detected. The channel width at each stage was 1287 μm (first stage), 472 μm (second stage), and 263 μm (third stage).

A photograph of the mini-fluorescent microscope is shown in Figure 1b. It consisted of three major parts: a plastic lens ($\times 20$), a long-pass filter, and a complementary metal-oxide semiconductor (CMOS) module. The long-pass filter was placed between the plastic lens and the CMOS module. The CMOS module and plastic lens were obtained from a commercially available webcam. The webcam lens was used to demagnify an object; magnification of the object was accomplished by reversing the lens. Because the total magnification of the microscopy system could be adjusted by varying the

distance between the plastic lens (objective lens) and CMOS module, we designed the plastic lens to move back and forth along a screw inside the lens housing. Collimated blue light (470 nm) was exerted from the top of the impaction plate, and the mini-fluorescent microscope was located perpendicular to the light source and in front of the particle deposition plate.

A cartridge-type impaction plate with an impaction zone is shown in Figure 1c. We used SYBR green I to distinguish between biological and non-biological particles on the impaction zone. SYBR green I nucleic acid stain increases the fluorescent signal that is induced when it is bound to the double-stranded DNA of a microorganism. The peak excitation and emission wavelength of SYBR green I are 495 nm and 525 nm, respectively. A PDMS mold with a well (dimensions: width \times height \times depth = $3 \times 10 \times 0.6 \text{ mm}^3$) in the center region was fabricated using a soft-lithography process, to be filled with agar (impaction zone). Distilled water with 3 wt% agar powder was autoclaved for 1 h, and SYBR green I was mixed with the autoclaved agar at 0.05% v/v. The mixture was poured into the PDMS mold before starting gelation. The semi-solidified impaction region allowed the reagent molecules to move freely into the DNA when a microorganism was inserted into the agar. It was designed to be disposable for convenient long-term usage. The microchannel and cartridge-type impaction plate, shown in Figures 1c and 1d, were packed in a stainless steel housing for mechanical sealing.

Test equipment of the proposed system

Filtered compressed air, at a flow rate of 1 L/min, entered the collision nebulizer which was used for the aerosolization of particles/bioaerosols. Two different particles were used for the test. Polystyrene latex (PSL) particles with diameters of 0.173, 0.222, 0.265, 0.305, 0.426, 0.482, 0.523, 0.598, 0.652, 0.72, 0.806, 0.913,

1.00, 1.11, 1.53, 2.1, 2.50, 3.00, and 4.00 μm were used for calibration, and *S. epidermidis* was used as an actual target bioaerosol. A diffusion dryer was added after the nebulizer to remove moisture from the aerosol stream. The aerosol stream, at a flow rate of 0.12 L/min, entered a ^{210}Po neutralizer to remove the electrical charge of the particles. Excess flow was vented to the atmosphere. Particles and bioaerosols with diameters smaller and larger than 0.55 μm were measured using a scanning mobility particle sizer and an aerodynamic particle sizer, respectively.

Particle collection efficiency

The collection efficiency curves of PSL particles at each impaction stage are shown in Figure 2. To measure the collection efficiency at each stage, three different devices with single stages were fabricated, having designed cutoff points of 2.02 μm , 0.88 μm , and 0.54 μm (as shown in the inset of Figure 2). The collection efficiency of a given particle size was calculated using the following equation:

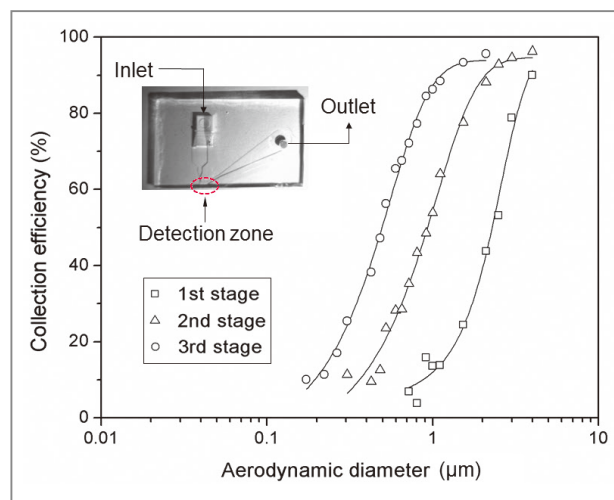


Figure 2. Collection efficiency of PSL particles at each impaction stage. Inset shows the device for measuring the collection efficiency at each impaction zone.

$$E(\%) = \left(1 - \frac{N_2}{N_1}\right) \times 100 \quad (2)$$

where N_1 and N_2 are the particle number concentrations at the inlet and outlet, respectively. The measured cutoff diameter at each stage was 2.24 μm (first stage), 0.91 μm (second stage), and 0.49 μm (third stage). The measured cutoff diameter values were slightly different from those designed based on the numerical analysis, but within 11%. The differences between the theoretical values and experimental results were attributed to particle loss because some of the particles were deposited on other regions of the microchannel instead of the impaction zone. Some of the particles with larger diameters ($d_p > 2 \mu\text{m}$) settled at the bottom of the channel due to gravitational force or stuck in the particle acceleration region, while the loss of some smaller particles was caused by diffusional deposition. In the case of solid particles, some of the deposited particles bounced from the impaction zone, leading to distortion of the collection efficiency curve. To prevent this phenomenon, an agar plate, instead of a PDMS plate, was used as an impaction zone, because the agar plate could hold a large amount of humidity, reducing the particle bounce effect. Furthermore, although particles with large inertia bounce more frequently at the impaction zone, they are also more likely to become embedded deeply in the agar plate.

The collection efficiency curve of the aerosolized *S. epidermidis* at each impaction stage is shown in Figure 3. The measured size distribution of the *S. epidermidis* is shown in the inset of Figure 3. The peak size and geometric standard deviation of *S. epidermidis* were 0.84 μm and 1.33, respectively. The collection efficiency curve of *S. epidermidis* showed similar characteristics to that of the PSL particles. The cutoff diameter of *S. epidermidis* at the second stage was 0.9 μm , similar to that of the PSL particles (0.91 μm). The measured collection efficiencies of the peak size (0.84 μm) at each impaction stage were 9% (first stage), 44% (second stage), and 77% (third stage), while the collection efficiencies of the PSL particles with a diameter of 0.84 μm

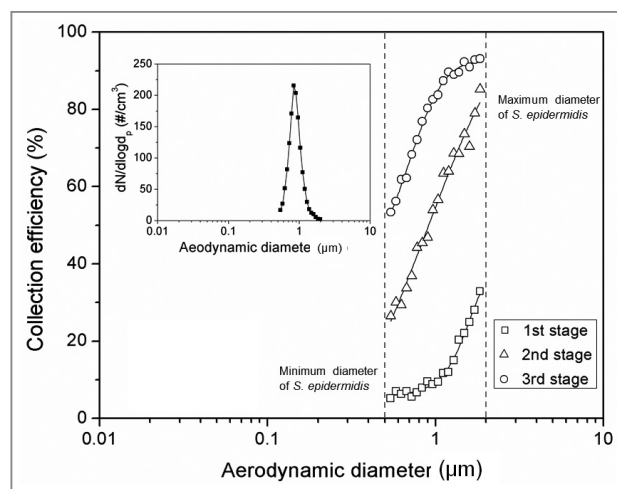


Figure 3. Collection efficiency of *S. epidermidis* at each impaction stage. Inset shows the size distribution of the aerosolized *S. epidermidis*.

at each impaction stage were 10% (first stage), 45% (second stage), and 81% (third stage), respectively.

Fluorescent image and intensity

Fluorescent images of *S. epidermidis* and PSL particles at the impaction zone are shown in Figure 4. The images were obtained from a device with three impaction stages (Figure 1d). The magnification of the images was 200 \times , and the working distance of the microscope was 3 mm. The images show that the collected *S. epidermidis* could be stained directly on the impaction plate in real time, without a permeabilization process. The mini-fluorescent microscope provided appropriate resolution for stained *S. epidermidis* imaging and detection. When microorganisms were collapsed at the impaction zone, they either landed smoothly or were embedded deeply, depending on their inertia. Of these two collection processes, the fluorescent staining of the bioaerosol was mainly the result of the latter, since SYBR green I molecules do not move freely in landed bioaerosol particles.

Figures 4a, 4b, and 4c show fluorescent images of the

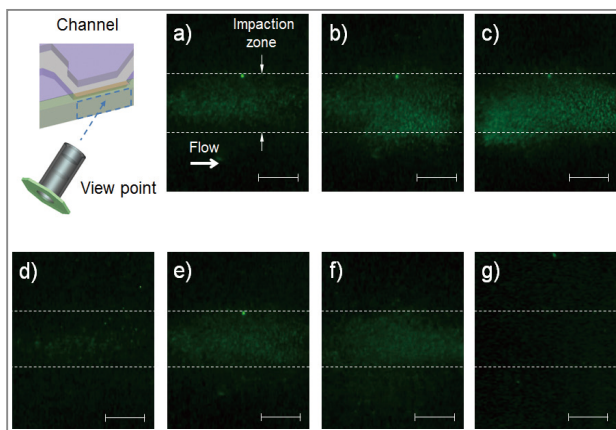


Figure 4. Fluorescent images at different sampling times and impaction stages. The schematic diagram indicates the viewpoint of the mini-fluorescent microscope; (a), (b), and (c) show photos at the second impaction zone with sampling times of 20 s, 40 s, and 60 s, respectively; and (d), (e), and (f) show photos at the first, second, and third stages, respectively, with a sampling time of 30 s. (g) Image of PSL particles (diameter: 1 μm) at the second impaction zone with sampling time of 30 s (all scale bars indicate 100 μm).

second impaction zone with respective sampling times of 20, 40, and 60 s. As the sampling time increased, more particles attached to the impaction zone, leading to an increase in fluorescent intensity. Some of the particles shown in Figure 4c deviated from the impaction zone (bottom wall region of the microchannel). Since the agar plate was in a deformable semi-solid state, it exhibited concave deformation caused by the pressure of the airflow. Figures 4d, 4e, and 4f show fluorescent images of the first, second, and third impaction zones, respectively, with a sampling time of 30 s. Because the collection efficiencies of the particles differed at each of the impaction zones in terms of aerodynamic particle diameter, the fluorescent intensities also differed at each stage. The fluorescent intensity at the first stage was quite low compared with the intensities at the second and third stages. Figure 4g shows an image of the PSL particles at the second impaction zone with a 30 s sampling time. The non-biological particles (which do not contain DNA) exhibited a negligible green fluorescent signal compared with microorganisms on the impaction zone, since double

stranded DNA-bound dye has a fluorescent intensity 1000 times greater than that of plain dye.

The fluorescent intensity at the second stage with varying sampling times is shown in Figure 5. The green fluorescent intensity was calculated from an in-house image-processing code programmed using MATLAB. Because the agar plate initially showed a low level of green signal, the initial fluorescent intensity was subtracted from the fluorescent intensity at later certain sampling times.

Generally, the fluorescent intensity increased with sampling time. However, although the number of microorganisms on the impaction zone increased linearly with sampling time, the fluorescent intensity did not show a linear relationship. Instead, the slope became more gradual with longer sampling times. This tendency was attributed primarily to the partial staining of the deposited microorganisms by SYBR green I because of the mountain-shaped deposition pattern, so that some of them did not make contact with the SYBR green I-containing agar, as well as a bleaching effect of the stain.

To address this problem, a cartridge-type impaction plate was used. From our calculations, we could detect

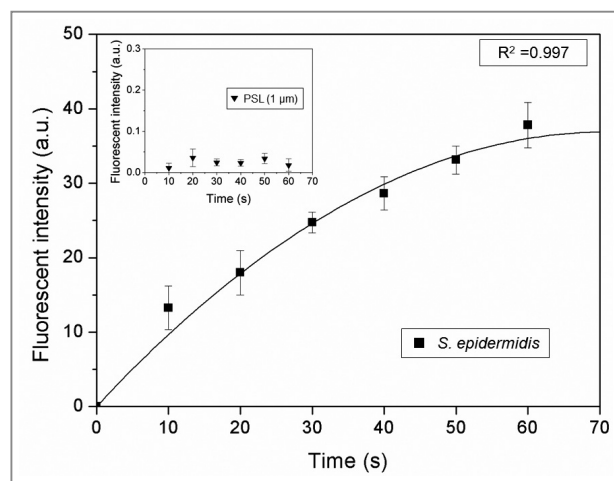


Figure 5. Fluorescent intensity of *S. epidermidis* at the detection zone as a function of sampling time. Inset shows the fluorescent intensity of the PSL particles with a diameter of 1 μm . The scale of the fluorescent intensity on each graph is the same.

biological particles in the standard atmosphere over about 2 h because the number concentration used in the present test was about 100 times higher than that of standard atmospheric conditions. The inset in **Figure 5** shows the fluorescent intensity of the PSL particles with a diameter of 1 μm at various sampling times. The level of fluorescent intensity (arbitrary units) in the inset was the same as that shown in the main part of **Figure 5**. The fluorescent intensity of the PSL particles was extremely low compared with that of the bioaerosols, indicating that the proposed system could identify biological particles from non-biological particles.

Note

This article and images are reprinted and reused from “Real-time detection of an airborne microorganism using inertial impaction and mini-fluorescent microscopy” in *Lab on a Chip*, Vol. 14, pp.244–251.

References

- [1] Douwel J, Thorne P, Pearce N, Heederik D. *Ann. Occup. Hyg.* 2003; 47: 187–200.
- [2] Blachere FM, Lindsley WG, Pearce TA, Anderson SE, Fisher M, Khakoo R, Meade BJ, Lander O, Davis S, Thewlis RE, Celik I, Chen BT, Beezhold DH. *Clin. Infect. Dis.* 2009; 48: 438–440.
- [3] Pak SS, Liu BYH, Rubow KL. *Aerosol Sci. Tech.* 1992; 16: 141–150.
- [4] Kang JS, Lee KS, Lee KH, Sung HJ, Kim SS. *Aerosol Sci. Technol.* 2012; 46: 966–972.
- [5] Wilhelm J, Pingoud A. *ChemBioChem.* 2003; 4: 1120–1128.



Center for Environment, Health, and Welfare Research

[Feature Articles]

Removal of Metal from Acid Mine Drainage Using a Hybrid System with a Pipe-Inserted Microalgae Reactor



Young Tae Park

Environmental Remediation
Laboratory
pyt1017@kist.re.kr



Jaeyoung Choi

Environmental Remediation
Laboratory
jchoi@kist.re.kr

Introduction

Acid mine drainage (AMD) causes environmental pollution that affects many countries with past or current mining industries. AMD normally contains high concentrations of heavy metals (As, Cd, Pb, Fe, etc.), aluminum oxides, and sulfuric acid [1]. In general, the contaminated water in a nearby mining site is characterized by a red or red-brown color due to the precipitation of Fe (see [Figure 1](#)). Pollution from these sources may have a detrimental effect on aquatic ecosystems and humans. The AMD treatment systems are classified as active or passive systems and depend on precipitation as the primary method for metal removal from AMD [2]. The most widespread active treatment process uses chemical-neutralizing agents such as limestone, lime, sodium hydroxide, sodium carbonate, and magnesia [3]. These alkaline materials are added to AMD to raise the pH, which accelerates the chemical oxidation of metals, resulting in hydroxide and carbonate precipitates.

Recently, microalgae have been intensively studied for the treatment of wastewater with biosorption and the production of biodiesel. Many researchers have reported that various species of microalgae can be cultured by nutrient-rich wastewater sources, and these cultures have produced high lipid yields [4]. It has further been found that microalgae have a metal removal ability due to metal uptake (bioaccumulation) from wastewater streams [5]. Microalgae have more potential for biodiesel production than conventional oil crops, due to their high photosynthesis efficiency and lipid content [6].

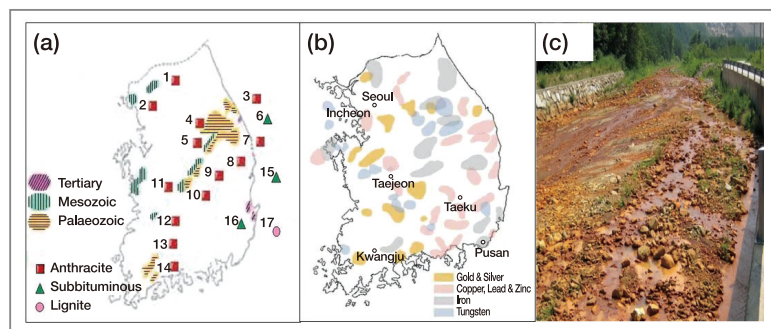


Figure 1. The distribution of abandoned mine sites in South Korea. (a) Distribution of coal mines. (b) Distribution of metal mines. (c) Acid mine drainage in a coal mine.

Clearly, iron is an important factor in microalgae growth and metabolic activities.

This research investigates the combination of an active treatment system using $\text{Ca}(\text{OH})_2$ and $\text{Mg}(\text{OH})_2$ and a biodiesel production system (known as a pipe-inserted microalgae reactor or “PIMR”) using microalgae. Iron was the major metal targeted for removal using both the active treatment and biodiesel production systems. The effects of chemical dosage and reaction time in the active treatment system were studied, as were the growth and lipid production of microalgae using pretreated AMD including iron. The function of residual iron was investigated to explain the enhanced growth rate and lipid production of microalgae in pretreated AMD using the active treatment system. In addition, a continuous PIMR system for iron removal was tested.

Experiments

The microalgae studied were isolated from a heavy metal-rich environment in an abandoned coal mine in South Korea. *Nephroselmis* sp. KGE 8 was selected for this study because of its tolerance to heavy metals; however, its adaptability to these metals was not considered.

The PIMR was constructed from transparent tempered glass with 30 acrylic pipes inserted at regular intervals (Figure 2). Light was sourced from sunlight as well as LED sticks.

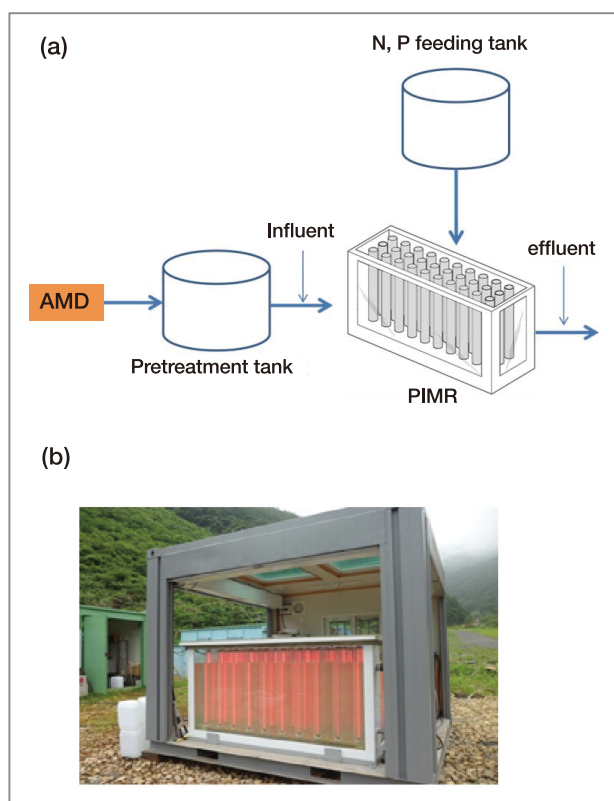


Figure 2. Schematic diagram of the pipe-inserted microalgae reactor (a) and a photo of the PIMR (b).

Active treatment systems are the standard method used in the AMD treatment industry. The process of an active system consists of three steps: aeration, neutralization and precipitation. By controlling pH to a typical set-point of 7, metals are precipitated. For determining the comparative effectiveness of alkalinity to

reduce iron in the AMD in our study, 0.3 - 0.4 mg L⁻¹ of Ca(OH)₂ and Mg(OH)₂ were spiked to the system at 60 and 90 min.

Results and discussion

Before treatment with the PIMR, the AMD was pretreated in a neutralizing plant. The composition of pretreated AMD depends on the input of calcium hydroxide and magnesium hydroxide as well as reaction time. Following pretreatment, final metal concentrations ranged from 4.64 ± 0.5 - 20.51 ± 9.8 mg L⁻¹ for iron and 3.9 ± 0.7 - 5.4 ± 0.5 mg L⁻¹ for manganese. Microalgae cultivation was then performed in the PIMR to examine the effect of initial concentrations of iron in the pretreated AMD. Cell growth and biomass productivity over time relative to the type of pretreatment influent are shown in Figure 3. When the concentration of iron ranged from 4.14 mg L⁻¹ - 10.92 mg L⁻¹ in the first and second pretreatment effluents, the cells of *Nephroselmis* sp. KGE 8 exhibited optimal growth and obtained a higher cell density. For cell concentration in the first and second type of pretreatment influent, optical density (OD) and dry cell weight (DCW) were 3.95 - 3.96 and 1.54 g L⁻¹, respectively (Figure 3a). In the control tanks, where microalgae were incubated in BBM (bold basal medium), the respective measurements were lower, i.e., OD was 3.54 and DCW was 1.38 g L⁻¹. These results indicate that iron is an essential trace metal which affects microalgae growth. Moreover, the medium used for pretreatment of AMD contained insoluble and soluble iron, both of which could be used by microalgae in their growth process. The slowest growth rate was found in the fourth pretreatment influent where the cell concentration was OD of 2.7 and DCW of 1.05 g L⁻¹. Biomass productivity (P) for the second type of pretreatment effluent increased with increasing Fe concentration until it reached 10.92 mg L⁻¹. The maximum biomass productivity (P) was 0.0602 g L⁻¹ day⁻¹ (Figure 3b). These results indicate that Fe in AMD can promote

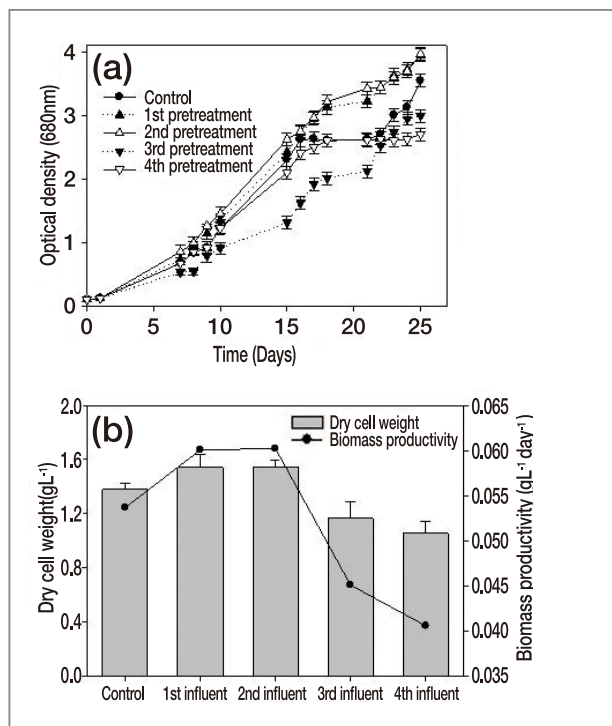


Figure 3. Biomass concentration over time for *Nephroselmis* sp. KGE 8 in each pretreatment phase of wastewater. (a) Optical density. (b) Dry cell weight and biomass productivity after 25 days.

biomass productivity. However, for the second and fourth types of pretreatment influents, higher Fe concentrations may inhibit microalgae growth. The onset of the stationary phase of microalgae in the fourth pretreatment occurred earlier, thus shortening the intervals for microalgae growth.

In a lab-scale test to confirm the effects of iron concentration, the growth of *Nephroselmis* sp. KGE 8 had a higher biomass yield (OD of 4.52) in BBM to which 10 mg L⁻¹ iron had been added (Figure 4). Initially, increasing the dose of Fe up to 10 mg L⁻¹ had increased the microbial growth, which indicated that iron acts as an essential nutrient for growth, because the maximum OD at 680 nm observed was 4.42 - 4.52 at a 10 mg L⁻¹ iron concentration. However, at amounts greater than 20 mg L⁻¹ of Fe, microbial growth decreased, and at amounts greater than 70 mg L⁻¹, microalgae growth was insufficient for experimental purposes. Based on these findings, a concentration of 10 mg L⁻¹ was employed as the optimum

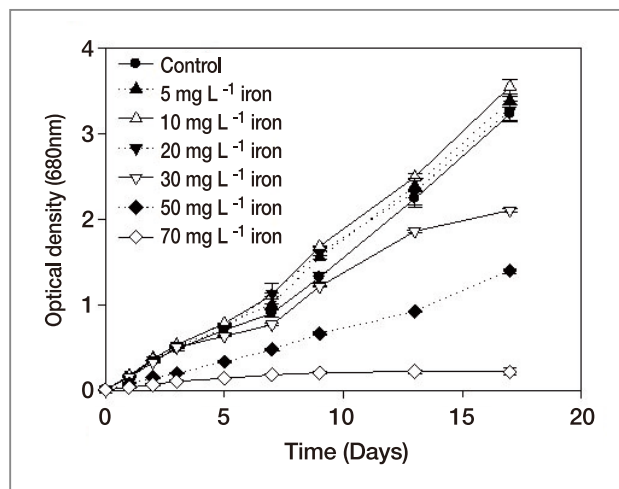


Figure 4. Effect of iron concentrations on *Nephroselmis sp. KGE 8* viability.

iron loading dose for microalgae growth in the PIMR since concentrations of over 20 mg L⁻¹ iron seemed to reduce the growth rate. The effects on microalgae growth are evident in a comparison of pretreatment phases. Growth in the fourth pretreatment influents was higher than in the third pretreatment influents during the first 20 days because the iron concentration of the cultures in the fourth pretreatment (20.51 ± 9.8 mg L⁻¹) was lower than in the third pretreatment (24.21 ± 2.7 mg L⁻¹).

When the microalgae was grown in the PIMR over 25 days, the extractable lipid content (% dry weight biomass), determined by the Bligh and Dyer method, was 38.8 % in the culture with the second pretreatment influent (Figure 5). The effect of iron on the lipid contents was investigated to find out if iron could increase lipid accumulation. The results indicate that lipid accumulation pathways were probably modified by a high concentration of iron. Even though the concentration of iron was similar in BBM added 10 mg L⁻¹ iron and second pretreatment, lipid contents of microalgae in second pretreatment was higher than in BBM added 10 mg L⁻¹. It seems that the second pretreatment contained a higher concentration of various minerals in the BBM, and these minerals could influence lipid accumulation.

Figure 6a shows the variation in total Fe concentration

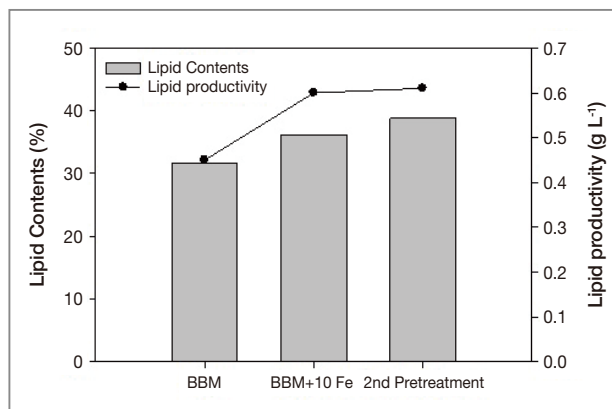


Figure 5. The measurement of lipid contents and productivity of microalgae in different media.

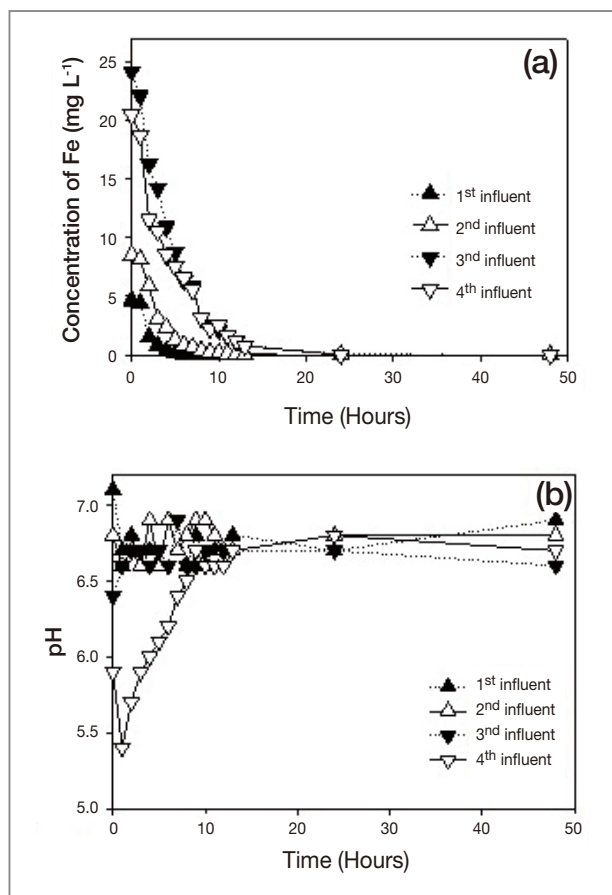


Figure 6. Variation of influent ($t=0$) and sample in the PIMR: (a) concentration of total iron, (b) pH.

in the effluent. Fe could be removed through various processes that included: (i) absorption of microalgae for cell growth; (ii) biosorption of metal ions on microalgae; and (iii) precipitation of metals inside the biological reactor. A direct relationship was observed between the initial Fe concentration and the amount of Fe taken up; the higher the initial Fe concentration, the larger the amount of Fe taken up. The maximum Fe loading capacity of *Nephroselmis* sp. KGE 8 was found to be 24.21 mg g⁻¹ in the third pretreatment wastewater (Figure 6a). However, the pH in the PIMR ranged from 5.4 - 7.1 (Figure 6b), allowing precipitation, and several different iron species (solid iron, colloid iron, aqueous iron) as well as bound iron at the microalgae surface could be taken up by the microalgae. Therefore, it is apparent that the PIMR system can remove both the insoluble Fe that remains in suspension and the Fe precipitates in a sludge system.

Conclusion

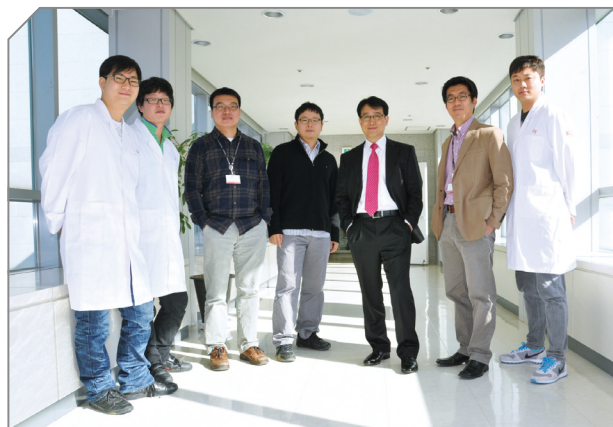
In this study, a PIMR with an active treatment system was developed and employed for microalgae cultivation. The *Nephroselmis* sp. KGE 8 in the PIMR showed a strong propensity to grow with pretreated AMD. The second of four pretreatment effluents, was found to have the optimal conditions for maximizing microalgae growth. 10 mg L⁻¹ iron BBMD was determined to have potential for use in microalgae culture because of the distribution of biomass increase. Further investigation revealed that changes in iron concentration can induce lipid accumulation.

Note

This article and images are drawn from "Removal of metal from acid mine drainage using a hybrid system including a pipes inserted microalgae reactor" in *Bioresour. Technol.*, Vol. 150, pp. 242-248.

References

- [1] Cheng, H., Hu, Y., Luo, J., Xu, B., Zhao, J. *J. Hazard. Mater.* 2009; 165: 13-26.
- [2] Das, B.K., Roy, A., Koschorreck, M., Mandal, S.M., Wendt-Potthoff, K., Bhattacharya, J. *Water Res.* 2009; 43: 883-894.
- [3] Van Hille, R.P., Boshoff, G.A., Rose, R.D., Duncan, J.R., *Resour. Conserv. Recy.* 1999; 27: 157-167.
- [4] Prathiam D M, Venkata S G., Venkata M S. *Renew. Energ.* 2011; 43: 276-283.
- [5] Boke O H, Seda T Z. *Fresen Environ Bull.* 2010; 19: 2981-2986.
- [6] Li X, Hu Y, Zhang Y. *Bioresour. Technol.* 2011; 102: 3098-3102.



Environmental Remediation Laboratory

[Feature Articles]

Novel Design of a Molybdenum Back Contact for High-Efficiency CIGS Solar Cells: Decoupling its Surface from the Bulk



Jeung Hyun Jeong

Photo-electronic Hybrids Research
Center
jhjeong@kist.re.kr

Introduction

Cu(In,Ga)Se₂ (CIGS) thin film solar cells have attracted much interest as a renewable energy source because they could provide the basis for developing low-cost and high-efficiency commercial-grade modules. Recently, CIGS cell efficiency at a laboratory scale has achieved 20.8%, which is superior to that of market-dominating multi-crystalline silicon (Si) solar cells [1, 2]. CIGS solar cells have a simple and unique cell structure consisting of substrate\Mo back contact\CIGS absorber\CdS buffer\ZnO\transparent conducting oxide (TCO) (see [Figure 1\(a\)](#)). Pursuing increased efficiency, the CIGS research community has been trying various approaches such as using flexible substrates (metal, polymer), replacing the buffer and window layers, employing a transparent back contact, replacing the absorber with a wider band gap or earth-abundant materials, etc. At the same time, various synthesis methods aimed at reducing costs and improving performance have also been investigated.

Despite the remarkably high efficiency that CIGS researchers have achieved, they are still struggling to advance toward large-area commercial modules with a level of efficiency comparable to that obtained in the laboratory. The most critical problem is a lack of understanding of the physics underlying the functioning of the CIGS solar cell. Since many of their achievements were obtained through trial and error, many researchers find it hard to discern which avenues for further research are most likely

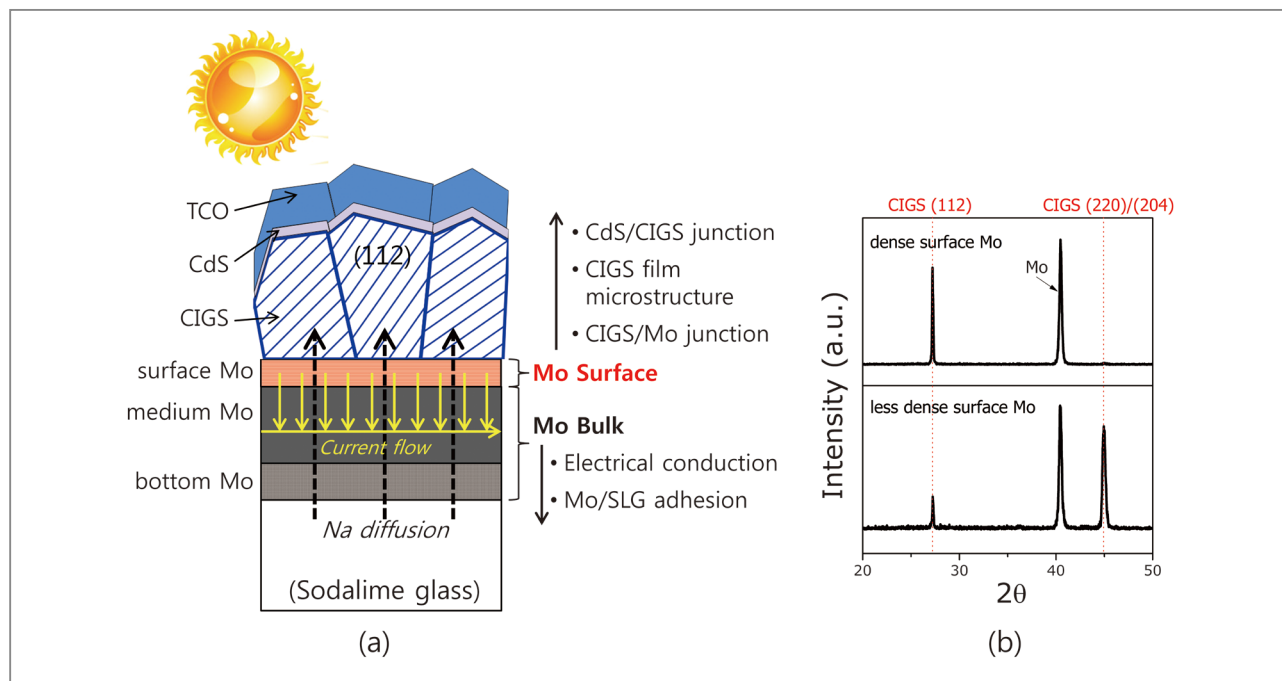


Figure 1. (a) The design concept of the back contact structure for enhancing the performances of CIGS solar cells, and (b) the resulting modification of CIGS films in terms of grain orientation.

to pay off. Our team, in pursuit of a leading position in CIGS photovoltaics (PV) research, has aimed at a deeper understanding of the device physics of the CIGS solar cell in relationship to the properties of the cell's constituent materials, to enable a more knowledge-based approach to CIGS R&D. The work introduced here is part of this approach.

Molybdenum (Mo) thin films are used as back contact materials for $\text{Cu}(\text{In,Ga})\text{Se}_2$ (CIGS) thin film solar cells to take advantage of their good electrical conductivity, ohmic contact with CIGS, and high-temperature stability [3,4]. Mo films are highly tunable, permitting optimization of the back contact electrode to yield a low resistivity and good adhesion properties. Sputtered Mo thin films display a variety of microstructures and densities, depending on the deposition pressure, substrate bias, and temperature [5,6]. The various Mo microstructures could influence the preferred orientation (texture) of a CIGS thin film, the Na diffusivity from a sodalime glass (SLG) substrate, the MoSe_2 reactivity, and eventually the CdS/CIGS junction,

as illustrated in Figure 1 [7-9]. The Mo microstructure might even substantially affect the photovoltaic conversion efficiency, although this is not easy to demonstrate. An optimum balance between (112) and (220)/(204) orientations, along with optimizing the Na concentration, can improve the diode quality of CIGS/CdS junctions, thereby increasing the open-circuit voltage (V_{OC}) and fill factor (FF) [10,11]. Therefore, the Mo properties must be optimized to enhance the efficiency of CIGS thin film solar cells. Unfortunately, the influence of the Mo properties on the various factors related to cell efficiency has not yet been fully understood.

Highly tunable Mo films as back contacts for CIGS solar cells

Mo films were deposited by direct-current (dc) sputtering, and the sputtering pressure and power were controlled to change the Mo microstructure and

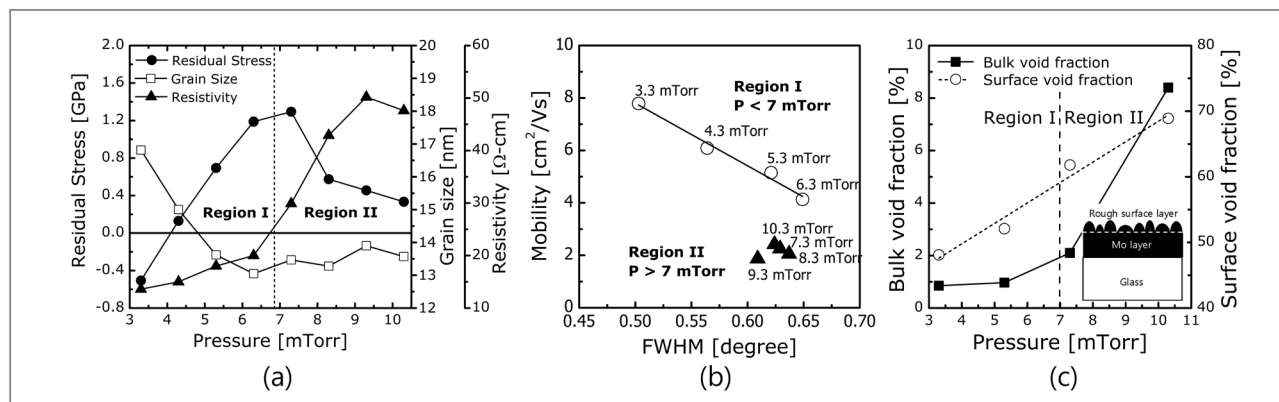


Figure 2. (a) The variation in residual stress, grain size, and electrical resistivity of Mo films, (b) carrier mobility vs. FWHM, and (c) void fractions of the Mo layer and rough surface layer, as a function of the working pressure [8].

properties. As shown in Figure 2(a), the variations in the residual stress, grain size, and electrical resistivity with pressure are significant, and apparently these variations alter in character between 6.3 and 7.3 mTorr. We divided the working pressure regime into a low pressure regime, region I (below 7 mTorr; the value can be varied depending on the sputter power and deposition chambers), and a high pressure regime, region II (above 7 mTorr), as indicated by a dashed line in Figure 2(a). In region I (relatively low working pressures), the residual stress changes from compressive to tensile and tends to increase gradually with increasing pressure. The grain size (calculated from the full width at half maximum (FWHM) of x-ray diffraction (XRD)) decreases with pressure and the electrical resistivity increases. However, in region II (considerably higher working pressures), the residual stress decreases with increasing pressure, which implies the triggering of a stress relaxation event. At the same time, the grain size becomes saturated and the resistivity starts to increase abruptly.

The above results show that the residual stress, grain size, and electrical resistivity are closely related and that there is a significant microstructural change in Mo thin films around 7 mTorr. Evidence for this conclusion is even more pronounced in Figure 2(b), which shows the relationship between the carrier mobility and the FWHM

(which is related inversely to the grain size). There is an inverse linear relationship between the mobility and the FWHM in region I, which means that the grain size decreases gradually with increasing pressure. However, the relationship deviates markedly from linearity in region II. In general, a decrease in the grain size in thin films means an increased number of grain boundaries (GBs), which charge carriers have to cross during electrical transport, so carrier mobility is decreased. The data in region I follow this general rule exactly. However, the abrupt deviation from linearity in region II of the relationship between mobility and FWHM implies that the nature of the grain boundaries has changed and that there are higher energy barriers to charge transport in region II. We believe that this significant microstructural change is related to void formation along grain boundaries in the high pressure regime.

Figure 2(c) shows the quantitative results of the variable angle spectroscopic ellipsometry (VASE) analysis for the void fractions. The void fractions in the rough surface layers are sufficiently large to account for the surface roughness and increase almost linearly with the working pressure. The void fraction in the Mo layer is pressure dependent. The void fraction in the Mo layer is negligible for region I and increases substantially for region II. It is worth emphasizing that we were able to derive

the microstructural parameters of the Mo films by using optical analysis tools such as VASE and multilayer optical modeling.

Influence of Mo microstructures on CIGS film properties

On the basis of the understanding of the relation between Mo microstructure and properties, we investigated the impact of varying the Mo microstructure on the key properties of CIGS films such as CIGS grain orientation and Na diffusivity. CIGS films were deposited for this study by a three-stage co-evaporation process. Figures 3(a) and (b) showed that the preferred orientation of CIGS thin films was strongly affected by the microstructures of the Mo back contacts on which CIGS films are grown [12]. A lower density in the Mo back contact (deposited in region II) tended to produce CIGS films with a higher degree of (220)/(204) orientations, attributed to the higher reactivity of the less-dense Mo toward Se, thereby forming a thicker MoSe₂ layer [12]. During the three-stage process, the (In,Ga)₂Se₃ phase (IGS) was deposited prior to conversion to a full CIGS film, and its preferred orientation eventually determined the orientations of the CIGS phases. For example, the (006)-oriented IGS grains produced (112)-oriented CIGS phases, whereas (300)-oriented grains produced (220)/(204) CIGS [7]. Transmission Electron Microscopy (TEM) observations showed that the presence of the MoSe₂ phase on the back contact tended to drive the IGS films into the (300) preferred orientation. Tentatively, it was concluded that the different reactivities of Mo toward Se during the 1st stage of heating (300–400°C), as a result of the different Mo microstructures, contributed primarily to determining the preferred orientations in the CIGS films. Figures 3(c) and (d) confirmed such different reactivity of Mo-Se depending on the Mo microstructure. More porous Mo reacted with Se forming thicker and more random MoSe₂.

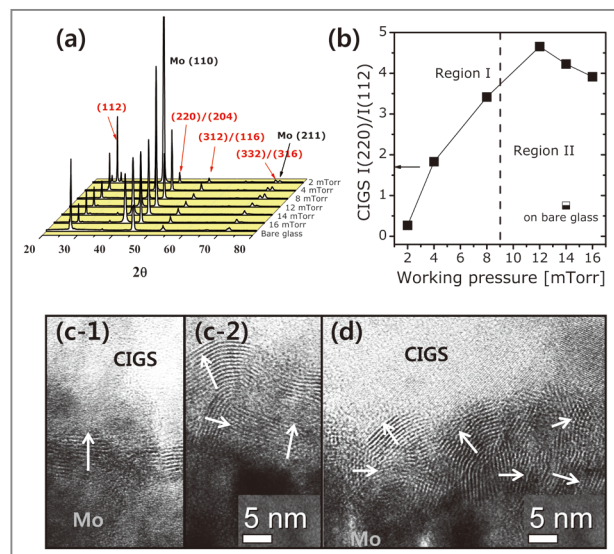


Figure 3. The effect of Mo microstructure on (a) the CIGS texture and (b) the ratio of two primary orientation peaks $I(220:204)/I(112)$. The TEM images around CIGS/Mo (c) with highly dense Mo and (d) with porous Mo.

Figure 4(a) shows that the Na concentrations in the CIGS and Mo layers were sensitive to the deposition pressure, indicating a strong correlation between Na diffusion and the microstructures (i.e., their densities) of the Mo layers, because the Mo surface became rougher and the bulk material became more porous with increasing working pressure [8]. The extent of Na accumulation at the CIGS/Mo interface increased with increasing deposition pressure, namely with decreasing Mo layer densities. Figure 4(b) shows the variations in the Na concentrations across the three regions as a function of the Mo deposition pressure. The Na concentration in the CIGS and CIGS/Mo interface regions underwent a linear increase as the deposition pressure increased. The Na concentration in the Mo bulk increased nonlinearly. These results indicated that Na diffusion into the CIGS was sensitive to the Mo bulk density, although the surface characteristics of the Mo layers played a more significant role.

At this point, the mechanism by which the surface characteristics of a Mo back contact layer affected the Na

ion diffusion behavior within the CIGS/Mo/SLG system was unclear. It was expected, however, that a higher Mo surface porosity (or density) and roughness could enhance the reactivity of the Mo toward ambient gas (e.g., oxygen) and Se during CIGS deposition. An increase in the Na accumulation with increasing deposition pressures (which lowered the Mo surface density) suggested that Na may accumulate more extensively in Na-containing Mo oxide and/or thicker Na-containing MoSe₂ layers.

The roles of these interfacial layers in Na diffusion were investigated by intentionally oxidizing or selenizing the Mo back contact layers prior to CIGS deposition. As shown in Figure 4(c), the oxidized samples displayed a higher Na content in the CIGS and a higher Na accumulation at the CIGS/oxidized Mo interface region than in the unoxidized samples. In contrast with the Na profiles of the oxidized samples, the selenized samples displayed a lower Na content in the CIGS, and consequently, a lower Na accumulation at the CIGS/selenized Mo interface region

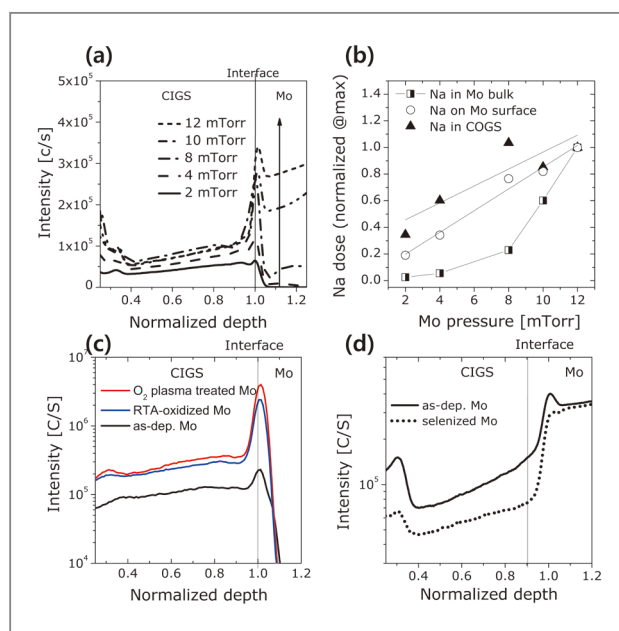


Figure 4. The effect of Mo microstructure on (a) secondary ion mass spectrometry (SIMS) Na depth profiles and (b) the Na concentrations in the CIGS, the CIGS/Mo interface, and the Mo bulk. The effect (c) of surface oxidation and (d) of surface selenization on the Na distribution in CIGS.

(see Figure 4(d)). The oxygen adsorbed onto the Mo back contact layer surface may attract Na ions from the SLG to form a Na-containing Mo oxide (e.g., Na₂MoO₄) [13]. Considering that oxygen preferentially adsorbs onto porous and rough surfaces rather than dense and smooth surfaces [9], Na ions are expected to accumulate at a CIGS/porous Mo interface region more extensively than at a CIGS/dense Mo interface region.

Decoupling the function of Mo surface from back contacts

Figure 5(a) shows the XRD patterns of CIGS films as a function of the Mo top-layer thickness in the double-layer Mo series. The double-layered Mo contacts consisted of porous top Mo layers deposited (at 12 mTorr) onto dense bottom Mo layers (deposited at 2 mTorr). Also shown are the intensities of the (112) and (220)/(204) orientations, quantified based on the Lotgering factors, in Figure 5(b). The fraction of the top-layer thickness relative to the total thickness (R) was varied over 0, 0.1, 0.5, and 1.0. A comparison of the extremes (R=0 and 1) revealed that CIGS films deposited on more porous Mo (R=1) showed stronger (220)/(204) orientations, whereas films deposited on denser Mo (R=0) showed stronger (112) orientations. This result agrees with previous results showing a correlation between the CIGS texture and the Mo density: a strong (112) orientation was observed on highly dense Mo, whereas a strong (220)/(204) orientation was observed on porous Mo [12]. Interestingly, the replacement of very thin surface (50 nm) in the Mo layer from denser (R=0) to more porous (R=0.1) yielded a significant increase in the (220)/(204) orientation, reaching a level almost on a par with the film prepared on high-porosity Mo (R=1). The results demonstrated that control over the surface density of the Mo back contacts was critical for determining the preferred orientation of the CIGS films, and the underlying properties of the back contact did not need to be varied.

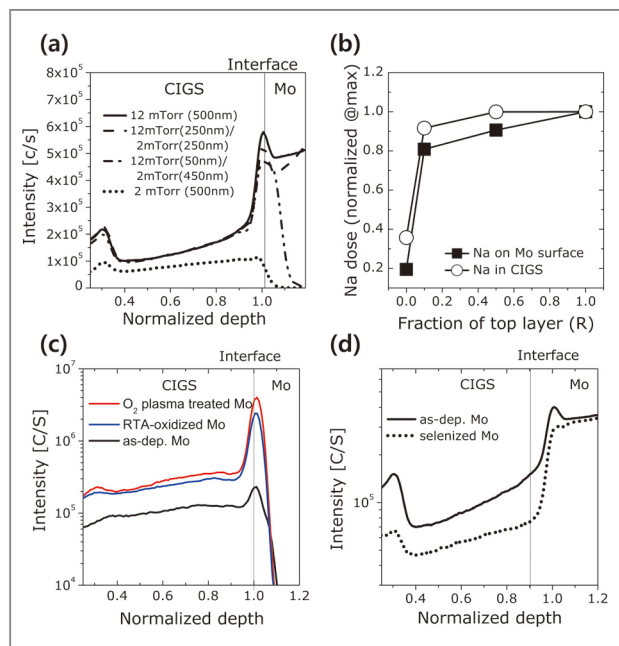


Figure 5. The preferred orientation of the CIGS films as a function of the thickness of the top Mo layer; (a) x-ray diffraction patterns and (b) Lotgering factors of (112) and (220)/(204). (c) The Na depth profiles as a function of the thickness of the top Mo layer, and (d) the resulting Na concentrations in the CIGS and at the Mo surface.

The same double-layer structures as above were used to investigate the effects of the surface characteristics and bulk density of a Mo layer on the diffusion of Na ions into the CIGS. The Na depth profiles in Figure 5(c) and the integrated Na doses in Figure 5(d) demonstrated that the Na concentration in the CIGS increased significantly upon deposition of a 50 nm-thick porous Mo layer, coming close to that in the CIGS coated on the porous single Mo layer (deposited at 12 mTorr). This result indicated that the extent of Na diffusion from the SLG into the CIGS depended more strongly on the surface characteristics of the Mo back contact layer (the surface density and roughness) than on the Mo bulk. There was also observed Na accumulation in the CIGS/Mo interface region, as shown in Figure 5(d). The Na concentration in the interface region was strongly correlated with that in the CIGS, in support of the results in Figure 4(b).

Novel design of back contacts optimized for CIGS solar cells

Based on the findings as described above, a novel Mo back contact structure (called a “trilayer”) was proposed to provide the dual functions of controlling the CIGS preferred orientation and Na diffusion as well as guaranteeing good electrical contact at high temperature. A microstructure (density)-variable surface layer (SL) was added to the conventional bilayer structure to convey high conductivity and adhesive properties. Optimization of this bilayer has been described elsewhere [14]. As shown in Figure 6(a), the SL was very thin (<10% of the back contact thickness) to avoid degradation in the back contact electrode resistance due to variations in the SL properties (deposited at pressures of 2–16 mTorr). All trilayered back contacts showed good electrical conductance, similar to that of a bilayer Mo alone, regardless of the properties of the Mo surface layers (deposited at different pressures). Figure 6(b) shows the preferred orientations of the CIGS films in terms of the Lotgering factors of each orientation as a function of the Mo surface layer deposition pressure: (220)/(204) intensities are indicated as solid lines and (112) ones as dashed lines. The CIGS orientation on SLG substrates was successfully controlled by varying the surface properties of Mo back contacts. As the SL deposition pressure was increased (resulting in a reduction in density), the (220)/(204) orientation became much more favorable, whereas the (112) orientation was much less favorable.

As shown in Figure 6(b), the suppression of Na diffusion from the SLG by the presence of a SiO_x film significantly changed the preferred orientation of the CIGS film below a deposition pressure of 8 mTorr by shifting the preference toward (220)/(204) and disfavoring the (112) orientation. In order to account for the Na-related change of CIGS orientation vs. Mo surface properties, the effect of Na doping as well as Mo density needs to be further addressed. In the CIGS films deposited on

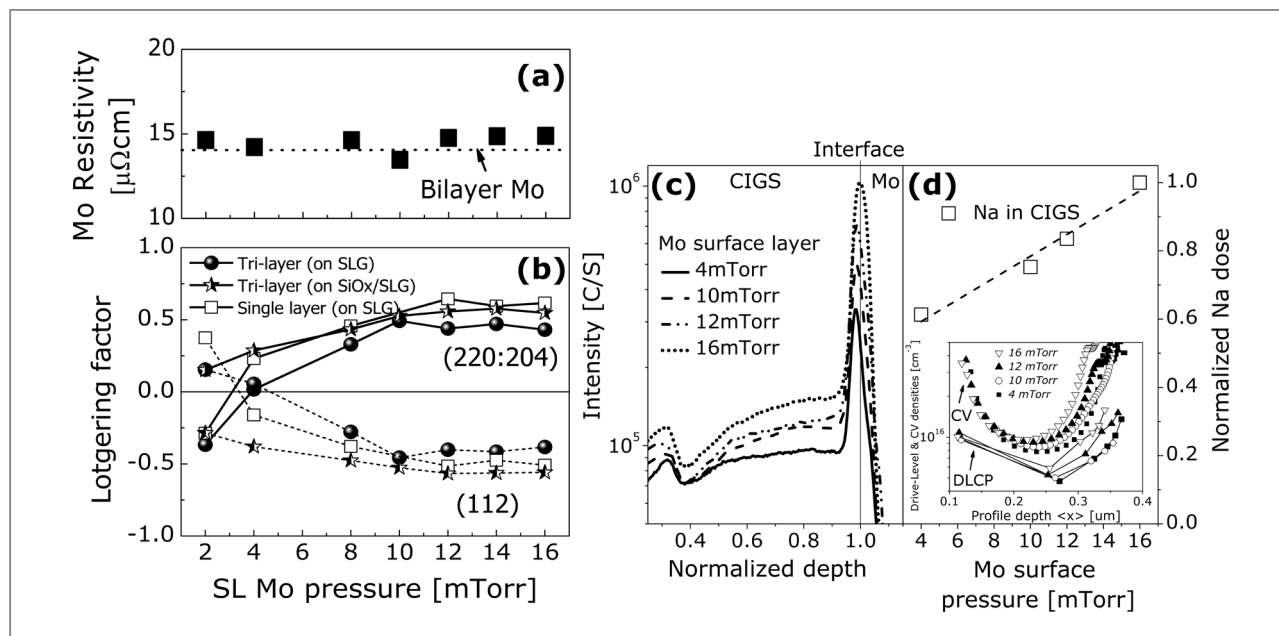


Figure 6. Influence of surface Mo properties in trilayer Mo structure on (a) the electrical resistance of the Mo trilayer back contacts, (b) the preferred orientation of the CIGS films, expressed as the Lotgering factor, (c) the Na depth profiles of CIGS films, and (d) the Na concentrations in the CIGS absorber. The profiles of the free-carrier density in the CIGS measured by capacitance-voltage and drive-level capacitance profiling (DLCP) are shown in an inset.

SiOx/SLG (Na-reduced case), the CIGS orientations were more random around the lower pressure of Mo surface layer, and (220)/(204) orientation became stronger toward higher pressure. The results suggest that highly dense Mo (deposited at low pressure) does not strongly force CIGS films to grow with any specific orientation. Knowingly, the presence of Na during CIGS deposition tended to enhance the development of (112)-oriented grains.[15] Such a Na interaction in Na-doped CIGS films shifted the CIGS orientation from close-to-random to stronger (112) orientation on a low-pressure Mo surface layer. However, such a Na doping effect was negligible in a high-pressure Mo surface layer. The results suggest that the ability of the porous Mo surface to force the (220)/(204) oriented growth of CIGS is much stronger than the Na doping effect favoring the (112) orientation.

Figure 6(c) shows the Na depth profiles of the CIGS/Mo trilayer as a function of the deposition pressure during preparation of the surface layer (varied from 4 to

16 mTorr). The Na concentration in the CIGS absorber layer was characterized using the technique presented in Figure 4(b), and the results are shown in Figure 6(d). The Na concentration in the CIGS (Na doping) increased as the deposition pressure increased. This result proves that Na concentration in the CIGS absorber can be controlled by surface manipulation of the Mo back contact, and that the Mo back contact trilayers can represent an important processing tool for the fabrication of CIGS solar cells. The Na ion concentration in the CIGS influenced the properties of the absorber layer, as demonstrated in capacitance-voltage ($C-V$) measurements of AZO/*i*-ZnO/CdS/CIGS/Mo trilayer devices using an impedance analyzer. The inset of Figure 6(d) shows the profiles of the free-carrier density in the CIGS as a function of the deposition pressure during preparation of the Mo surface layer. The free carrier density in the CIGS increased as the deposition pressure increased (i.e., as the Na ion concentration in the CIGS increased). The Na ions effectively passivated defects in

the CIGS. The Na ion concentration, controlled through the surface properties, provides a means for optimizing the V_{OC} (and FF), which are closely related to the free carrier density.

The photovoltaic conversion efficiencies of CIGS solar cells fabricated on the trilayer Mo/SLG are shown in Figure 7 as a function of the Mo surface layer deposition pressure. Figure 7 also shows the related solar parameters, such as the open circuit voltage (V_{OC}), short circuit current (J_{SC}), fill factor (FF), shunt conductance (G_{sh}), series resistance (R_s), diode ideality factor (A), and saturation current (J_0). The cell efficiencies were considerably improved by increasing the deposition pressure of the Mo surface layer. The contributions of the V_{OC} and FF to the improved efficiency were particularly substantial.

In general, a reduction in A and J_0 indicates that the diode recombination current is reduced via either quasi-bulk or space charge region (SCR) in CIGS, resulting from the suppression of the population of recombination centers or reduced SCR width. Such an improved p-n junction could increase FF and V_{OC} . Interestingly, the series resistance (R_s) decreased significantly with increasing deposition pressure of the Mo surface layer. Its contribution to the improved FF in this case was more substantial than expected from the improved p-n junction. Since the increasing pressure of the Mo surface layer resulted in the enhancement of (220)/204 grain orientation, these findings suggested that the CdS/CIGS junction properties were most likely influenced by the preferred orientation of the CIGS films. However, because the Na concentration slightly increased at the same time (as a result, the carrier density slightly increased), the effect of carrier density on cell efficiency needs to be addressed in the interpretation. We will next discuss how the different CIGS grain orientations could influence the CdS/CIGS junction properties.

The formation of CdS/CIGS junctions during the chemical bath deposition (CBD) process is not fully understood. It has been suggested that Cd and S

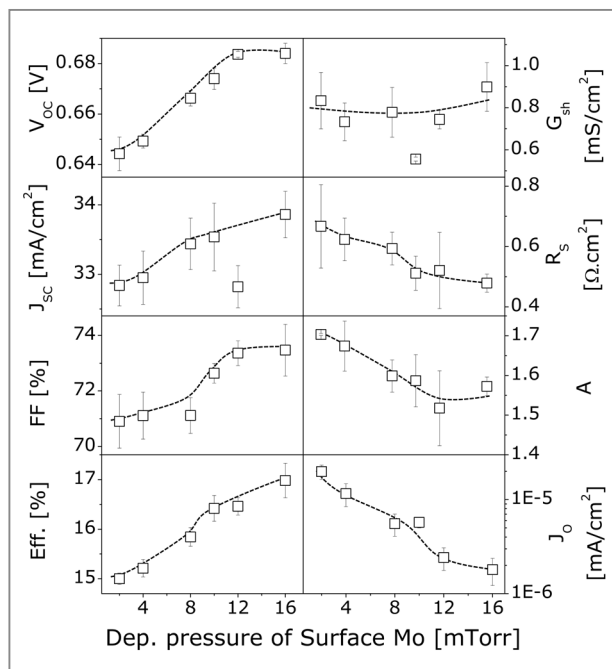


Figure 7. Solar performance parameters of the CIGS solar cells (on sodalime glass) employing trilayer back contacts as a function of surface Mo layer properties.

ions can modify the electronic characteristics of CIGS surfaces via surface etching and ion diffusion during CdS deposition [16, 17]. Such Cd diffusion could yield n-type inversion behavior at the CIGS surface via Cd-Cu exchange, which would yield better p-n junctions [17]. Some have reported that Cd diffusion is more favorable on (220)/(204)-oriented CIGS films because (220)/(204) surfaces provide a more open structure compared to the (112) surfaces [18, 19]. Our findings indicate that the electronic nature of the CdS/CIGS junctions can vary with the CIGS orientation: a higher degree of n-type inversion is obtained for surfaces with a higher degree of (220)/(204) orientation. Such variations in the CdS/CIGS junction properties could explain the reduced recombination rate in CIGS films with a higher degree of (220)/(204)-oriented grains. The alteration in the CdS/CIGS junction could also explain the reduction in the series resistances with increasing (220)/(204) orientation (see Figure 7).

Conclusion

This study demonstrated that the key microstructural factors of CIGS solar cells such as CIGS grain orientation and Na concentration can be controlled by tuning the Mo surface densities alone. On the basis of this finding, a trilayer Mo back contact was suggested as a novel structure for high-efficiency CIGS solar cells. Exact understanding of the role of Mo back contact in CIGS PV enabled the novel design of Mo back contact, resulting in substantial improvement in most functions without any functional sacrifice. The suggested novel Mo back contacts could provide versatile solutions to the diverse problems that the CIGS solar cell industry has encountered or will encounter in its efforts to achieve higher-efficiency solar cells. Our team will continue its efforts to fully understand the physics of CIGS photovoltaics and to achieve a leading position in the CIGS community.

Note

This article and images are drawn from “Control of the preferred orientations of Cu(In,Ga)Se₂ films and the photovoltaic conversion efficiency using a surface-functionalized molybdenum back contact” in *Prog. Photovolt.: Res. Appl.* 22, 69, “Electrical properties of CIGS/Mo junctions as a function of MoSe₂ orientation and Na doping” in *Prog. Photovolt.: Res. Appl.* 22, 90, “Effect of a Mo back contact on Na diffusion in CIGS thin film solar cells”, in *Prog. Photovolt.: Res. Appl.* 21, 58, and “Optical analysis of the microstructure of a Mo back contact for Cu(In,Ga)Se₂ solar cells and its effects on Mo film properties and Na diffusivity” in *Sol. Energy Mater. Sol. Cells* 95, 2959.

References

- [1] Press release at ZSW, “ZSW produces world record solar cell,” Oct. 2013.
- [2] Chirilă A, Reinhard P, Pianezzi F, Bloesch P, Uhl AR, Fella C, Kranz L, Keller D, Gretener C, Hagendorfer H, Jaeger D, Erni R, Nishiwaki S, Buecheler S, Tiwari AN. *Nature Mater.* 2013; 12:1107–1111.
- [3] Orgassa K, Schock H-W, Werner J. *Thin Solid Films* 2003; 431: 387–391.
- [4] Shafarman W, Phillips J. *25th Photovoltaic Specialists Conference 1996*; pp. 917–919.
- [5] Scofield JH, Albin DS, Duda A, Ballard B, Predecki P. *Thin Solid Films* 1995; 260: 26–31.
- [6] Khatri H, Marsillac S. *J Phys: Condens Matter* 2008; 20, 055206.
- [7] Egaas B, Contreras MA, Kinga D, Swartzlandera A, Dullweber T. *Thin Solid Films* 2000; 361: 167–171.
- [8] Jeong JH, Baik YJ, Yoon JH, Cho S, Kim WM, Park JK, Lee TS, Seong TY. *Sol Energy Mater Sol Cells* 2011; 95: 2959–2964.
- [9] Wada T, Kohara N, Negami T, Nishitani M. *Jpn J Appl Phys.* 1996; 35: 1253–1256.
- [10] Contreras MA, Jones K, Gedvilas L, Matson R. *16th European Photovoltaic Solar Energy Conference and Exhibition*, Glasgow, UK, 2000, pp.1-4.
- [11] Wei SH, Zhang SB, Zunger A. *J Appl Phys.* 1999; 85: 7214–7218.
- [12] Jeong JH, Yoon JH, Baik YJ, Yoon KH, Kim JK, Kim WM, Park JK, Lee TS, Seong TY. *35th IEEE Photovoltaic Specialists Conference (PVSC)*, Philadelphia, USA, 2010; pp. 002443–002447.
- [13] Kronik L, Cahen D, Schock HW. *Adv Mater.* 1998; 10: 31–36.
- [14] Yoon JH, Baik YJ, Yoon KH, Kim WM, Park JK, Seong TY, Jeong JH. *J Phys D: Appl Phys.* 2011; 44: 425302.
- [15] Granath K, Bodegard M, Stolt L. *Sol Energy Mater Solar Cells* 2000; 60: 279–293.

- [16] Kessler J, Velthaus KO, Ruckh M, Laichinger R, Schock H-W, Lincot D, Ortega R, Vedel J. *Proc. the Sixth Int. Photovoltaic Science and Engineering Conference (PVSEC-6)* 1992, pp. 1005–1010.
- [17] Nakada T, Kunioka A. *Appl Phys Lett.* 1999; 74: 2444–2446.
- [18] Chaisitsak S, Yamada A, Konagai M. *Jpn J Appl Phys.* 2002; 41: 507–513.
- [19] Contreras MA, Egaas B, Ramanathan K, Hiltner J, Swartzlander A, Hasoon F, Noufi R. *Prog Photovolt: Res Appl.* 1999; 7: 311–316.



Chalcogenide Photovoltaics Team /
Photo-Electronic Hybrids Research Center

Think modular: a simple apoferritin-based platform for the multifaceted detection of pancreatic cancer

ACS Nano

2013; 7: 8167-8174.

Mintai P. Hwang, Jong-Wook Lee, Kyung Eun Lee, Kwan Hyi Lee*
kwanhyi@kist.re.kr

The generation of nanosized probes often requires time-intensive and application-specific optimization processes that involve conjugating a nanoconstruct to a targeting moiety. Herein, we genetically modify apoferritin and generate a universal interface system composed of protein G and 6X His-tag. The resulting construct, conferred with modularity and high targeting efficiency, is applied toward two distinct applications in the detection of a pancreatic cancer biomarker and used to demonstrate its potential in the facile exchange of nanoprobe components.

PI3K–GSK3 signalling regulates mammalian axonregeneration by inducing the expression of Smad1

Nature Communications

2013; 4: 2690.

Saijilafu¹, Eun-Mi Hur*, Chang-Mei Liu, Zhongxian Jiao, Wen-Lin Xu & Feng-Quan Zhou
ehur@kist.re.kr

In contrast to neurons in the central nervous system, mature neurons in the mammalian peripheral nervous system (PNS) can regenerate axons after injury, in part, by enhancing intrinsic growth competence. However, the signalling pathways that enhance the growth potential and induce spontaneous axon regeneration remain poorly understood. Here we reveal that phosphatidylinositol 3-kinase (PI3K) signalling is activated in response to peripheral axotomy and that PI3K pathway is required for sensory axon regeneration. Moreover, we show that glycogen synthase kinase 3 (GSK3), rather than the mammalian target of rapamycin, mediates PI3K-dependent augmentation of the growth potential in the PNS. Furthermore, we show that the PI3K–GSK3 signal is conveyed by the induction of a transcription factor Smad1 and that acute depletion of Smad1 in adult mice prevents axon regeneration *in vivo*. Together, these results suggest PI3K–GSK3–Smad1 signalling as a central module for promoting sensory axon regeneration in the mammalian nervous system.

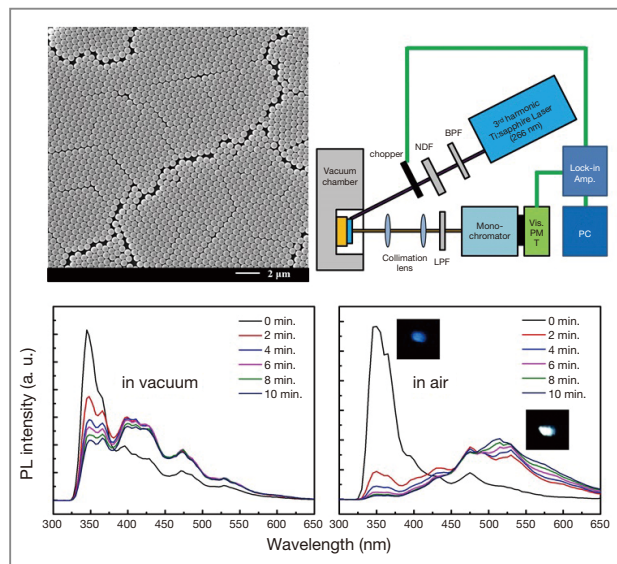
White light emission from polystyrene under pulsed ultraviolet laser irradiation

Scientific Reports

2013; 3: 3253.

Eunbyeom Kim, Jihoon Kyhm, Jung Hyuk Kim, Gi Yong Lee, Doo-Hyun Ko, Il Ki Han, and Hyungduk Ko*
kohd94@kist.re.kr

This paper reports for the first time the luminescent property of polystyrene (PS) produced by pulsed ultraviolet (UV) laser irradiation. We have discovered that, in air, UV-irradiated PS nanospheres emit bright white light with a dominant peak at 510 nm, while in a vacuum they emit in the near-blue region. From a comparison of PS nanospheres irradiated in vacuum and air, we suggest that white luminescence is due to the formation by photochemical oxidation of carbonyl groups on the surface of PS. Our results potentially offer a new route and strategy for white light sources.



The text and graphs of this report were reprinted and reused from *Sci. Rep.* 3, 3253 (2013) to be used only in KIST.

Gate-controlled spin-orbit Interaction in InAs high-electron mobility transistor layers epitaxially transferred onto Si substrates

ACS Nano

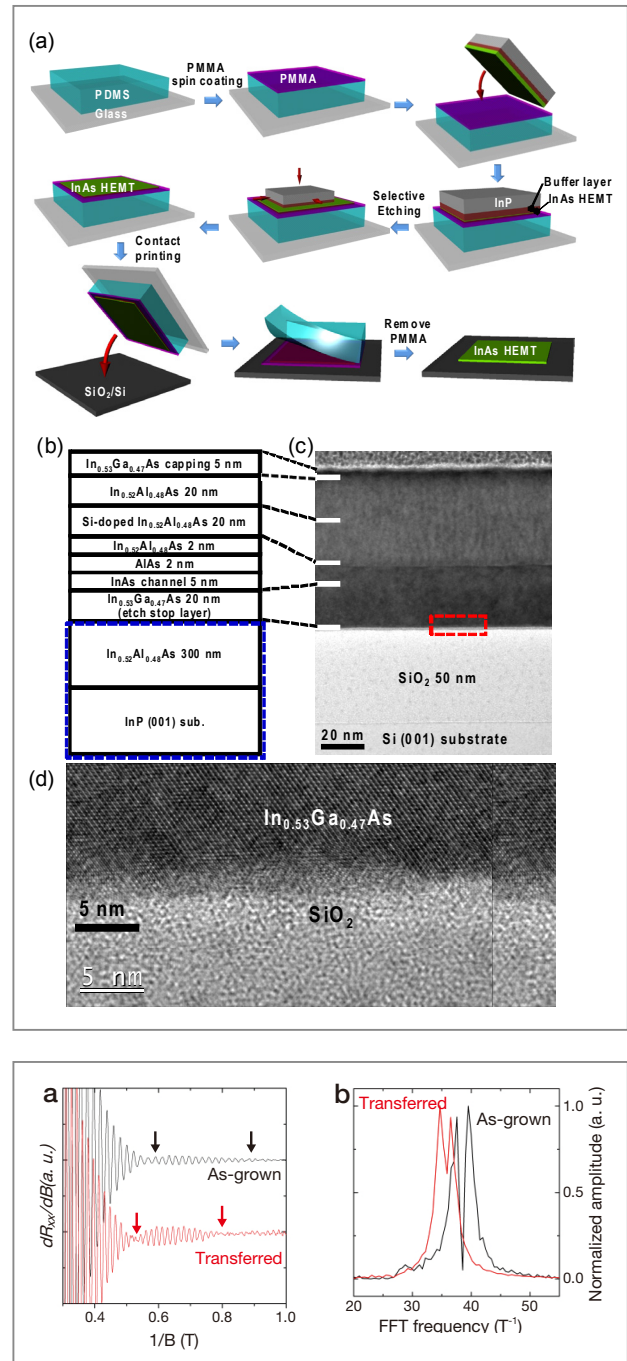
2013; 7: 9106-9114.

Kyung-Ho Kim, Doo-Seung Um, Hochan Lee, Seongdong Lim, Joonyeon Chang, Hyun Cheol Koo, Min-Wook Oh, Hyunhyub Ko, and Hyung-jun Kim*
mbeqd@kist.re.kr

Spintronics utilizes the spin degree of freedom of electrons as well as charge, thus enabling a wide range of applications from logic to storage devices. The Rashba spin-orbit interaction (SOI) is particularly important in spintronic devices, such as the spin field-effect transistor (spin-FET). Recently, III-V compound semiconductors (CSs), such as InGaAs, InAs, and InSb, which have a significantly larger g -factor, high electron mobility, and strong SOI, have attracted much attention as channel materials in spin-FETs. One of the challenges in the development of spin-FETs is the heterogeneous integration of devices onto Si substrates, allowing III-V CS spintronics to be incorporated into existing Si semiconductor technology. Similarly, technologies have been developed for the growth of magnetic tunnel junctions (MTJs) on Si substrates. Furthermore, MTJ-based memory can then be integrated with Si complementary metal-oxide-semiconductor (CMOS) logic circuit in order to realize future universal large-scale integration (LSI) circuits.

We demonstrate gate-controlled spin-orbit interaction (SOI) in InAs high electron mobility transistor (HEMT) structures transferred epitaxially onto Si substrates. Successful epitaxial transfer of the multilayered structure after separation from an original substrate ensures that the InAs HEMT maintains a robust bonding interface and crystalline quality with a high electron mobility of 46,200

cm^2/Vs at 77 K. Furthermore, Shubnikov-de Haas (SdH) oscillation analysis reveals that a Rashba SOI parameter (α) can be manipulated using a gate electric field for the purpose of spin field-effect transistor operation. An important finding is that the α value increases by about 30% in the InAs HEMT structure that has been transferred when compared to the as-grown structure. First-principles calculations indicate that the main causes of the large improvement in α are the bonding of the InAs HEMT active layers to a SiO_2 insulating layer with a large band gap and the strain relaxation of the InAs channel layer during epitaxial transfer. The experimental results presented in this study offer a technological platform for the integration of III-V heterostructures onto Si substrates, permitting the spintronic devices to merge with standard Si circuitry and technology.



Effect of V_2O_5 loading of V_2O_5/TiO_2 catalysts prepared via CVC and impregnation methods on NO_x removal

Applied catalysis B, Environmental

2013; 140-141: 708-715.

Woojoon Cha, Sungmin Chin, Eunseuk Park, Seong-Taek Yun, Jongsoo Jurng*
jongsoo@kist.re.kr

In this study, $V_2O_5/CVC-TiO_2$ materials with different concentrations of V_2O_5 were prepared via chemical vapor condensation (CVC) and impregnation. The catalytic activities of these materials were tested and the physicochemical characteristics were analyzed using XRD, BET, FT-IR spectroscopy, XPS, HR-TEM, EDX mapping, H_2 -TPR, and NH_3 -TPD. The NO_x removal efficiency of the $V_2O_5/CVC-TiO_2$ catalysts was higher than that of the $V_2O_5/P25-TiO_2$ catalysts and increased with increasing V_2O_5 concentration. At $200^\circ C$, the highest NO_x conversion was observed using 7 and 10 wt% $V_2O_5/CVC-TiO_2$ catalysts. The NO_x conversion curve reached a plateau corresponding to the maximum conversion when the V_2O_5 content was greater than 7 wt%. The $V_2O_5/CVC-TiO_2$ catalyst comprised mainly anatase-phase TiO_2 and well-dispersed V_2O_5 . A greater concentration of V (well-balanced V_{4+}/V_{5+}) species existed on the $V_2O_5/CVC-TiO_2$ catalyst surface. H_2 -TPR and NH_3 -TPD testing confirmed that the $V_2O_5/CVC-TiO_2$ catalyst is highly reducible and has many acidic sites.

Kinetic enhancement in photocatalytic oxidation of organic compounds by WO_3 in the presence of Fenton-like reagent

Applied catalysis B, Environmental

2013; 138-139: 311-317.

Hongshin Lee, Jihyun Choi, Seokheon Lee*, Seong-Taek Yun, Changha Lee, Jaesang Lee
seocklee@kist.re.kr

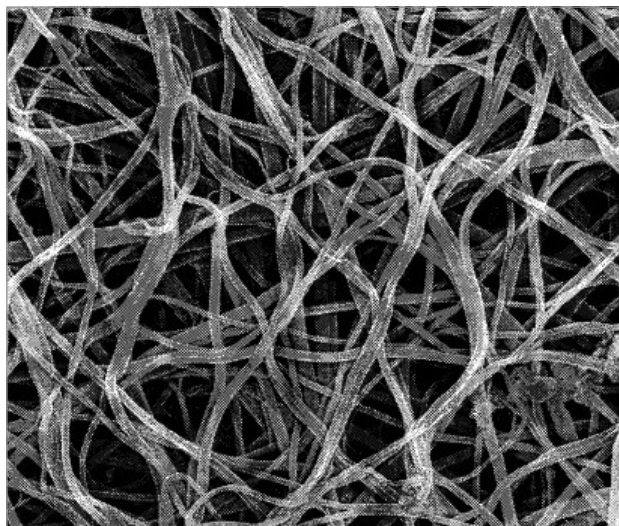
WO_3 -mediated photocatalytic oxidation is achievable in the presence of electron acceptors as an alternative to O_2 or co-catalysts enabling O_2 reduction pathway. This study suggests the combination with Fenton-like reagent ($Fe(III)/H_2O_2$) as a strategy to improve the photocatalytic activity of WO_3 . Under neutral pH condition where $Fe(III)$ is present as iron oxide precipitate, photocatalytic degradation of 4-chlorophenol (4-CP) proceeded 3-fold faster in the $WO_3/Fe(III)/H_2O_2$ system relative to the WO_3/H_2O_2 system, while no noticeable oxidation occurred in the systems of $Fe(III)/H_2O_2$, WO_3 , and $WO_3/Fe(III)$. Such efficacy increase at circumneutral pH was observed in photocatalytic oxidation of diverse organics including phenol, bisphenol A, acetaminophen, and carbamazepine. Compatible with the pH dependence of photocatalytic activity of the $WO_3/Fe(III)/H_2O_2$ system, hydroxylation of benzoic acid and coumarin as indirect indication for OH radical production was drastically retarded with increasing pH. The pH effect indicates that OH radical as primary oxidant may be responsible for the kinetic enhancement in the $WO_3/Fe(III)/H_2O_2$ system. In that platinum deposits or Nafion layers as physical barriers possibly inhibit surface $Fe(III)$ precipitation, use of platinized or Nafion-coated WO_3 caused the negligible photocatalytic improvement in the ternary system. Effective oxidative degradation in the presence of the UV cut-off filter corroborated visible light activation of the $WO_3/Fe(III)/H_2O_2$ system.

Method of fabricating carbon material, carbon material prepared by the method, cell material and apparatus using the same

US 8486584 (2013.07.16)

Heung Yong Ha / hyha@kist.re.kr

Disclosed is a method for fabricating a carbon material, by which carbon fibers or carbon tubes, particularly branched carbon fibers or carbon tubes, are obtained via a so-called self-growing process without using external carbon sources. The carbon material obtained by this method has a large specific surface area and further includes a metal catalyst, and thus may be used in cell materials for a fuel cell or secondary battery, hydrogen storage devices, capacitors, solar cells, display panel or the like.



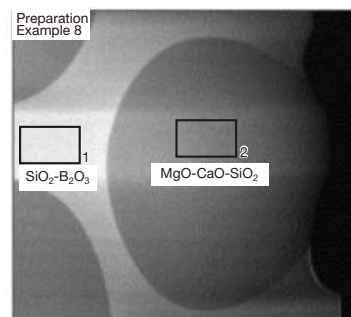
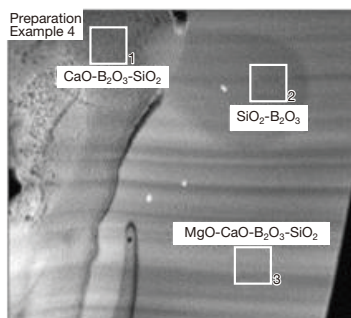
Low temperature co-fired ceramics with low dielectric loss for millimeter-wave application

US 8507393 (2013.08.13)

Jae Gwan Park / jgpark@kist.re.kr

Provided is a dielectric ceramic composition comprising: 40-70 wt % of a borosilicate-based glass frit comprising 50-80 mol % of SiO_2 , 15-20 mol % of B_2O_3 , 0.1-5 mol % of one or more alkali metal oxide selected from Li_2O and Na_2O , and 0.1-30 mol % of one or more alkaline earth metal oxide selected from MgO , CaO , SrO and ZnO ; and 30-60 wt % of a ceramic filler represented by Chemical Formula 1: $(\text{Zn}_{1-x}\text{Mg}_x)_2\text{SiO}_4$ (1) wherein $0 \leq x \leq 1$.

The disclosed low temperature co-fired ceramic (LTCC) composition is sinterable at low temperature, with a relative density of at least 95% in the temperature range of 800-900°C, is capable of minimizing electric loss, with a dielectric constant of 4-7 and a very low dielectric loss, and is applicable from a low-frequency band to a millimeter-wave band of 60 GHz or more.

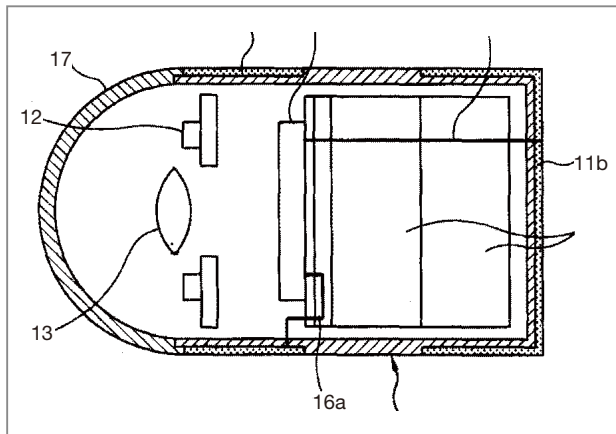


Method and system for data communication using a body

US 8559900 (2013.10.15)

Tae-Song Kim / tskim@kist.re.kr

Disclosed is a portable device for data communication using a body as a conductor to transmit data to a receiver. The portable device includes a data receiving unit to receive data, a controller unit to control processing of data to be transmitted, a current limiting circuit to limit a current of a signal corresponding to the data to be transmitted to a predetermined value, and transmitting electrodes connected to the current limiting circuit and to contact the body to transmit the signal having the current of predetermined value to the receiver.



Method for preparing graphene ribbons

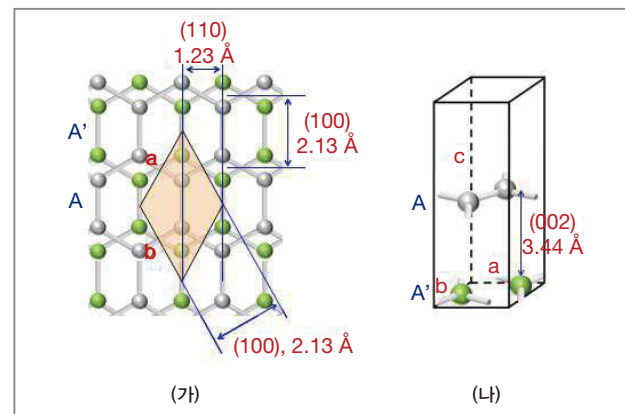
US 8597607 (2013.12.03)

Jae-Kap Lee / jklee@kist.re.kr

The object of the present invention is to provide a route for mass production of graphene ribbons, thus opening up industrial applications utilizing large scale amounts, i.e., tons per year, of this innovative carbon material.

To achieve these and other advantages and in accordance with the purpose of the present invention, as embodied and broadly described herein, there is provided a method for preparing graphene ribbons, comprising crumbling the graphitic materials composed of long graphene helices (several micrometers in length) into short graphene ribbons (up to about 50 nm in length). The graphene ribbon-based materials are stacked in AA arrangements in which the interlayer bond force is weaker than that of an AB structure. This development provides a route for large-scale production of graphene ribbons, thus opening up large-scale industrial applications, i.e., tons per year, of this innovative carbon.

The foregoing and other objects, features, aspects and advantages of the present invention will become more apparent from the following detailed description of the present invention when taken in conjunction with the accompanying drawings.



Zinc air fuel cell with enhanced cell performance

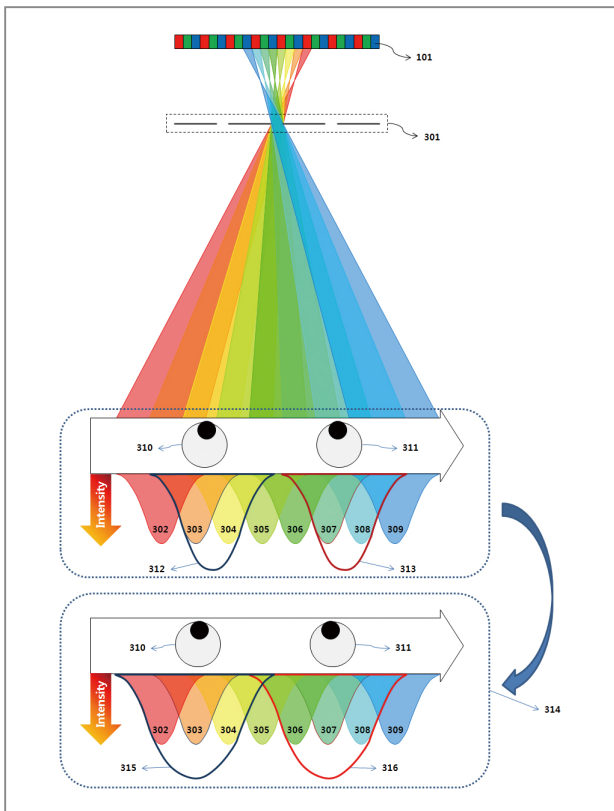
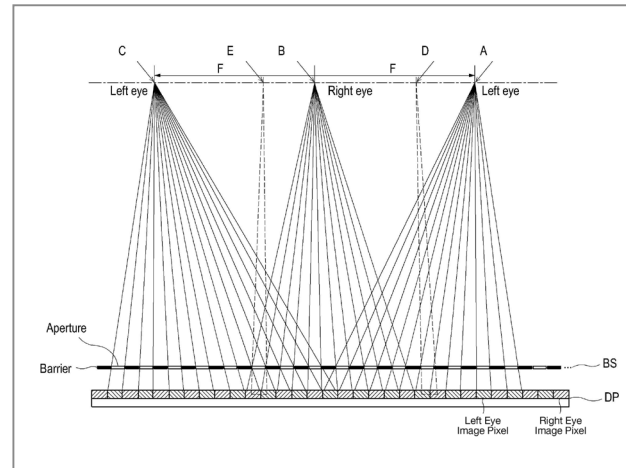
Device for three-dimensional image display using viewing zone enlargement

US 8610711 (2013.12.17)

Sung Kyu Kim / kkk@kist.re.kr

The present invention relates to an autostereoscopic image display device capable of observing a natural three-dimensional image without crosstalk or pseudo-stereoscopic zone between optimal viewpoints and without using special glasses. The three-dimensional image display device of the present invention includes: a display panel configured to display image information of at least two viewpoints; an optical substrate that is separately disposed from the display panel at a predetermined distance, the optical substrate being configured to form at least one intermediate viewing zone between left and right viewing zones included in base viewing zones corresponding to two viewpoints, which

are observed when the position of an observer moves horizontally; and a control unit configured to provide the image information corresponding to the respective viewpoints at the base viewing zones and remove image information from at least one intermediate viewing zone.

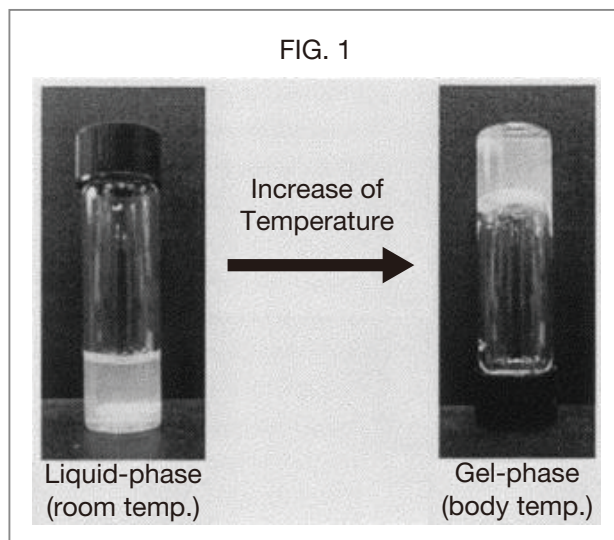


Poly(organophosphazene) containing degradation controllable ionic group, preparation method thereof and use thereof

US 2014-0031289 (2014.01.30)

Soo-Chang Song / scsong@kist.re.kr

The present invention relates to a thermosensitive phosphazene-based polymer having a degradation controllable ionic group, a use thereof, and a use thereof as a material for delivering bioactive substances. The phosphazene-based polymer has the thermosensitivity of showing the temperature-dependent sol-gel phase transition. Thus, it forms a gel phase at body temperature when it is injected into the body to make it easy to control the release of bioactive substances such as drugs, and has the functional groups capable of making chemical bonds such as ionic bond, covalent bond, coordinate bond, etc., with drugs and thus is excellent in bearing the drugs. Since it can control the degradation rate depending on the kind of ionic group, it can selectively control the release time depending on the characteristics of drugs. Furthermore, it has an excellent biocompatibility and thus is very useful as a material for delivery of bioactive substances such as drugs, etc.



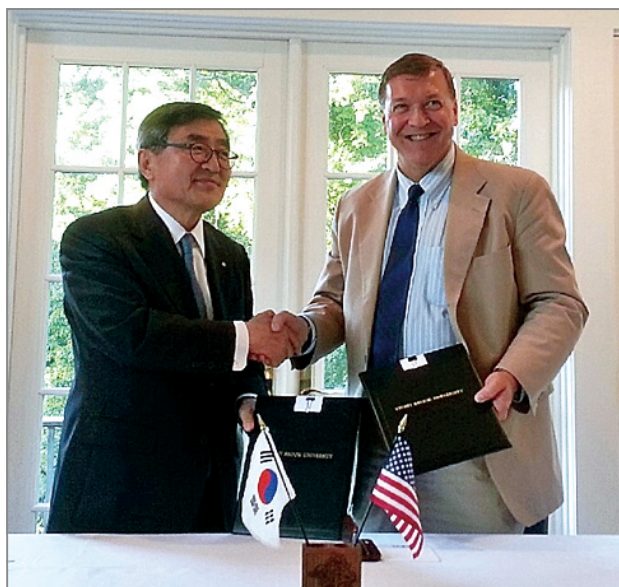
KIST and SBU Join Hands to Accelerate Research in Brain Disorders

June 4, 2013

KIST and Stony Brook University (Stony Brook, New York) agreed to cooperate in the areas of life and health sciences by signing a Memorandum of Understanding at Stony Brook University on June 4, 2013.

The objective of this agreement is to combine the expertise of KIST and SBU in neurology to create a synergistic effect. More specific cooperation measures are slated to follow, such as long-term joint research projects in life and health sciences (including neurology) and the establishment of a lab, operated by KIST, on the SBU campus. KIST and SBU also plan to launch cooperative projects in various areas, such as training, education, exchange of information and personnel, and commercialization of technologies.

Professor Dennis W. Choi of the Department of Neurology at Stony Brook University School of Medicine has been appointed as the director of the KIST Brain Science Institute and will hold concurrent offices at KIST and SBU, thereby ensuring stronger ties between the two institutions. Professor Choi is a globally renowned authority in the field of clinical translational research. While



a Ph.D. student at Harvard Medical School, he discovered the physiological mechanism of action of benzodiazepine drugs and received an award from the National Foundation for Brain Research and the 1998 Christopher Reeve Research Medal.

One of four state universities in New York, Stony Brook has produced three Nobel Laureates since its establishment in 1957 and includes various academic departments, such as applied science, medical science, pharmacology, business, social science, education, and the arts. The SBU School of Medicine specializes in diseases of the brain and will work closely with the KIST Brain Science Institute on the mechanism, diagnosis, treatment, and basic research associated with Alzheimer's disease.

Cooperation Between KIST and Harvard Medical School in Cancer Biology

July 3, 2013

KIST and the Dana-Farber Cancer Institute (DFCI), a major affiliate of Harvard Medical School, signed a Memorandum of Understanding that allows joint research in cancer biology. The formal signing took place on the KIST campus on July 3, 2013. The agreement lays the



groundwork for future joint cancer research projects and the establishment of a lab, operated by KIST, at the Dana–Farber Cancer Institute. In addition, KIST and DFCI agreed to build a close relationship in various research areas through exchange of information and personnel.

Established in 1947, the Dana–Farber Cancer Institute is one of 40 comprehensive cancer centers in the U.S. designated by the National Cancer Institute. DFCI provides cancer treatment and conducts clinical trials based on its advances in cancer research. The institute employs about 580 researchers specializing in fields such as oncology, molecular imaging, and immunology. A principle goal of DFCI is to disseminate information related to innovative cancer treatments as well as outcomes from its scientific research in cancer to the world.

Chairman of the Vietnamese National Assembly and Delegation Visit KIST

July 22, 2013

Nguyễn Sinh Hùng, chairman of the National Assembly of Vietnam, and a Vietnamese delegation of 14 members visited KIST on July 22, 2013. The delegation included the chairman of the Commission for External Relations, secretary of the Office of the National Assembly, several important members of the National Assembly, the minister of Planning and Investment, and the Vietnamese ambassador to South Korea. Dr. Kil-

Choo Moon, president of KIST, provided an overview of KIST research to the delegation and discussed ways to gradually increase cooperation between KIST and Vietnam, including the launch of a KIST-modeled research institute in Vietnam, known as V-KIST.

During his visit to Korea in March 2012, Prime Minister Nguyễn Tấn Dũng of Vietnam had requested the Korean government's assistance in establishing V-KIST. The launch of of this institute is now underway as a part of KOICA's official development assistance program.

The V-KIST project is modeled on the establishment of KIST, which received considerable support from the U.S. in its early years and subsequently made substantial contributions to South Korea's economic development. Accordingly, the focus of V-KIST is to strengthen Vietnam's scientific and technological capacity in order to contribute to Vietnam's economic development. President Moon commented, "Vietnam's capacity for research will greatly improve through V-KIST and it represents a major turning point for Vietnam's science and technology. The prime minister's visit will also encourage more cooperation and the V-KIST project will become an exemplary case for other ODA projects to follow."

Currently, 16 Vietnamese students are enrolled in KIST's IRDA program (the International R&D Academy) and 32 Vietnamese alumni have earned master or doctoral degrees at KIST.



Encouraging Ethiopia's Development through S&T Cooperation

October 1, 2013

Ethiopia has been a longtime ally of Korea, even sending Royal Guards during the Korean War. To support scientific, technological and economic development in Ethiopia, KIST signed a Memorandum of Understanding on October 1, 2013, with Adama Science and Technology University, the first organization in Ethiopia to offer degree programs for teachers of technology. KIST and ASTU agreed to cooperate in the areas of personnel exchange (including researchers, teachers, and students), joint research and other areas of mutual interest.

Professors from ASTU visited KIST in April of this year to discuss and gather recommendations on the economic development plans of Ethiopia. In addition, visiting researchers from ASTU have participated in a KIST research project on sewage treatment technology since September. This arrangement is part of the ongoing collaboration between KIST and ASTU.

After signing the agreement, KIST donated funds from its "Science Sharing Fund" to ASTU, which is to be used for boosting and fostering S&T talent in Ethiopia.



KIST Celebrates Its 48th Anniversary

February 10, 2014

Marking the 48th anniversary of its founding, KIST celebrated on February 10 at a ceremony attended by 500 staff and guests including Keon Kim, president of the Korea Research Council of Fundamental Science & Technology, and Sang-mok Lee, first vice minister of Science, ICT and Future Planning.

Byung Gwon Lee, acting president of KIST, said in his remarks, "48 years of burning the midnight oil has paid off in developing KIST as well as Korea," and he gave thanks for the efforts of all researchers and scientists in the field of technology. Dr. Lee stressed three important points. First, science and technology must become the foundation for a creative economy through convergence research. Second, more effort should be expended to ensure the future of Hongrung Complex as a source for a creative economy. Third, with the establishment of V-KIST, pending collaborative partnership with Switzerland, and many more international endeavors, KIST must play the role of a global leader by becoming a creative S&T mecca.



Dr. Byung Gwon Lee Sworn in as the 23rd President of KIST

March 13, 2014

The inauguration ceremony for the 23rd President of KIST was held at KIST on March 13, 2014.

KIST was the first comprehensive research institute in Korea, and over the past 50 years it has excelled in science and technology research, driving the economic growth of the nation. As part of welcoming the new president, KIST unveiled a renewed direction based on extensive research expertise accumulated since its early days and its robust human network and infrastructure as a leading national research institute.

In his comments, Dr. Byung Gwon Lee, the new president of KIST, stated that making a concerted effort to resolve current social issues should be a top priority for the institute. He reiterated KIST's commitment to addressing social issues and securing future resources to tackle the problems of the nation, including aging of the population and potential shortages of energy and food resources. Also, as regards national initiatives to

establish a creative economy, the new president added, "KIST will make every effort to ensure that basic and core research achievements are directly linked to enhancing the capabilities of SMEs and encouraging technology-based business start-ups." President Lee also referred to the upcoming 50th anniversary of KIST by stating that KIST's next 50 years would be marked by a renewed spirit of challenge based on the lessons learned from its first 50 years.

As a researcher who has been with the institute for more than 30 years, President Lee promised to maintain an open door policy so that all staff members would feel free to communicate their ideas and concerns.

President Lee graduated from Seoul National University in 1980 with a major in Chemical Engineering and in 1989 earned his Ph.D. in Chemical Engineering in the U.S. at the University of Akron. He joined KIST in 2004 as head of the Environment/Energy Division and served as vice president from 2012 until his current appointment as president.



Academic Programs of KIST

KIST-Academia Collaborative Education Program (1991~)



IRDA (2001~)



UST (2004~)



KIST-Academia Collaborative Education Program

KIST-Academia Collaborative Education Programs, the master's and PhD programs at KIST, were started in **1991** in collaboration with local universities in Korea. The aim of the programs was to nurture key talent who would then lead the development of technology applicable to high-tech industries. Thus far, over 2,000 students have earned master's or PhD degrees.

The curriculum requires students to complete their course work at a university and conduct research projects and complete their theses at KIST, all under the supervision of highly-qualified advisors and professors.

Through these programs, students gain hands-on research experience by participating in high-level projects conducted at KIST. When these graduates enter industries, they not only transfer technological expertise, but also strengthen a firm's capacity for research.

Universities in Collaboration

- Korea University, Yonsei University, Hanyang University, Kyunghee University, Sogang University, Ewha Womans University, Kwangwoon University, University of Seoul, Gangneung-Wonju National University, Chonbuk University, Jeonju University, Kunsan University, Ajou University and Chosun University



International R&D Academy (IRDA)

The International R&D Academy (IRDA) was launched in September **2001** to build international manpower in the field of science and technology through providing both master's and PhD programs at KIST.

The main goal of the IRDA is to strengthen research capacity by tapping into pools of potential talent in countries from all around the world and to establish a comprehensive educational program at the national level to encourage the training of technology professionals among international students from a wide range of countries. With its extensive alumni network, the IRDA is also expected to contribute significantly to Korea's ongoing ODA projects as well as future projects by building ties between Korea and the science and technology professionals in developing countries.

Operation Policy

- Foster research-oriented professionals by allowing for direct participation in research projects.
 - Utilize KIST infrastructures to the fullest through lab experiments and practice.
- Operate educational programs to foster the S&T manpower of developing countries on the national level.
 - Encourage joint participation of academia-industry research: allow credit exchange, hands-on experience in actual industrial working fields.

KU-KIST (2013~)



Programs

- Programs: master's program, PhD program, and combined master's/PhD program
- Degree: UST degree or dual degree from major universities
- Teaching method: tutorial system (professor/student ratio: 1:1 ~ 1:3)
- Full Scholarship: tuition, registration cost and monthly stipend

University of Science and Technology (UST)

The University of Science and Technology is an educational institution for graduate students founded through the joint efforts of 30 government-sponsored research institutions involved in science and technology. Its goal is to train talented professionals in science and engineering fields who will then be capable of developing the fields most important in the 21st century, such as convergence technology. A rich educational experience and excellent research opportunities, combined with the top-notch facilities and equipment of public and national research institutes, are offered by UST.

At UST, programs are offered which are too complex for ordinary universities, such as new technology convergence, in full-time master's and PhD programs. One of the advantages of the UST programs is that it allows students to join ongoing research projects at KIST as well as work side-by-side with professionals in industrial fields, thus enabling deeper insights into major coursework.

Since its inception in March 2004, UST has evolved significantly, particularly by diversifying its curriculum and programs in response to its goal of becoming a global educational leader and the best national research university in Asia.

Majors

- A total of 81 majors are offered through UST: (24 in the sciences and 57 in engineering fields)
- Majors at KIST: Biological Chemistry, Biomedical Engineering, Clean Energy and Chemical Engineering, Energy and Environmental Engineering, HCI and Robotics, Nanomaterial Science and Engineering, Neuroscience

KU-KIST Graduate School of Converging Science and Technology

The Korea Institute of Science and Technology (KIST) and Korea University (KU) established the KU-KIST Graduate School of Converging Science and Technology for the first time in Korea based on "dual appointment system between universities and research institutions" to foster world-class convergence science and technology experts who can meet the current social demands.

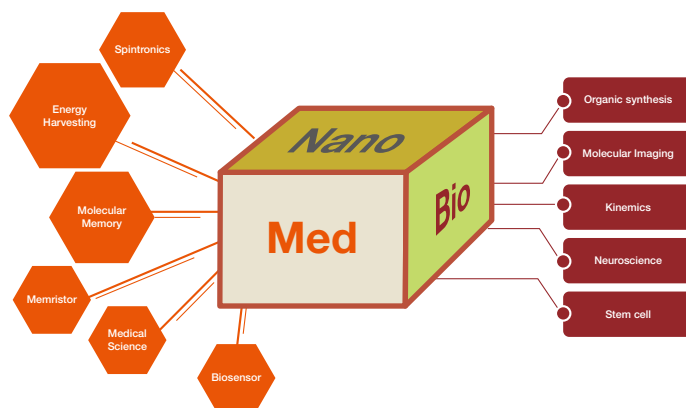
The KU-KIST Graduate School of Converging Science and Technology is a professional graduate school established to foster the world's best experts in IT-nanoscience (IT-NS) and bio-med by integrating BT, IT, and NT with cutting-edge medical technology and to carry out integrated education and research between Korea University (KU) and the Korea Institute of Science and Technology (KIST).

Research Environment

- A graduate school fostered by the best professors and researchers of Korea University and the Korea Institute of Science and Technology leading the IT-NS and bio-med fields.
- We provide monthly stipends and full scholarships to all students.
- We provide diverse educational and research opportunities to students, such as joint research with distinguished universities and companies in Korea and abroad, overseas dispatch, and internships.
- We actively make use of the advanced research infrastructure of the Korea Institute of Science and Technology to guide the research of students for them to draw more advanced research achievements during their studies for a degree.

Education and Research Fields

Energy harvesting, molecular memory, information delivery, spintronics, grapheme, and memristor (artificial brain) using nanoscience and biotechnology-medical science as well as convergence science and technology for molecular videos, artificial organs, kinomics, biosensors, stem cells, nerve science, and nanomedicine and pharmaceuticals using organosynthetic knowledge.



V-KIST: A National Research Institute Modeled After KIST to be Established in Vietnam

A Discussion with Dr. Kil-Choo Moon, former KIST president

From recipient to donor

Founded almost 50 years ago at a time when the Korean economy was devastated, KIST benefitted enormously from aid provided by the United States and went on to be an instrumental force in developing Korea's impressive economy. Given its success, Korea has been able to transform itself from a recipient country to a donor country that encourages model programs in developing countries.

Korea joined the OECD (Organization for Economic Cooperation and Development) in 1996 and became a member of OECD's Development Assistance Committee in 2010. Providing aid and support to establish V-KIST puts Korea very much in the international spotlight for promoting a model for the development of science and technology with this ODA (Official Development Assistance) program. As described by Dr. Moon,

Batelle Memorial Institute played a pivotal role when the late President Park Chung Hee asked the then U.S. president, Lyndon Johnson, to help build an industrial research institute in Korea 50 years ago. At the time, Batelle Memorial Institute had been operating for 36 years; however, it was not financially well off. Nevertheless, Batelle gave its full support in the establishment of KIST. The efforts of KIST in establishing V-KIST will not only create an exemplary cycle in S&T ODA, but also, it will significantly contribute in upgrading the national status of Korea as a donor country.

Dr. Moon planned and led the V-KIST project from the start. This project was selected as one of the top ten science & technology news events in 2013, as ranked by the Korea Federation of Science and Technology Societies. Expressing his gratitude at receiving this accolade, Dr. Moon said,

Support for launching V-KIST demonstrates the level of maturity in our society. I feel a heavy sense of responsibility on my shoulders.

V-KIST to drive future growth and train qualified scientists and engineers

The target completion date for V-KIST is September 9, 2017. V-KIST will be built as a comprehensive research institute similar to KIST; however, its specific research areas will only be determined after a thorough analysis of the industrial and economic status of Vietnam and discussions with Vietnamese officials.



Dr. Moon contends that V-KIST will explore various options for driving Vietnam's industrial growth, thereby enabling the country to select the most economically promising avenues for R&D. He went on to say,

Although there are many research institutes in Vietnam, they lack appropriate facilities, treat researchers poorly, and are not conducting research that is in sync with industries, a situation which is commonly found in most socialist countries. KIST will share its management knowhow and provide advisory services to V-KIST.

Why Vietnam?

In 2011, the Vietnamese government made the promotion of science and technology a priority as part of a socio-economic development strategy designed

to propel Vietnam into advanced industrialization by the year 2020. Accordingly, Vietnam turned to Korea since Korea had demonstrated such unprecedented growth in its economic and industrial development. Instead of the almost 200 years it takes for most countries to become economically advanced, it had taken only 50 years for Korea, an example which has great appeal to developing countries. Prime Minister Nguyen Tan Dung of Vietnam visited KIST in March 2012 and expressed his wishes to build a research institute resembling KIST in Vietnam. KIST replied positively and promised to examine his request further.

On October 29, 2012, a Memorandum of Understanding was signed between KIST and Vietnam which established the basis for cooperation through the establishment of V-KIST. This was followed by a joint declaration at the Korea-Vietnam summit talks in September 2013 announcing the opening of a research institute in Vietnam and the transfer of KIST management expertise to help spur economic growth in Vietnam through science and technology.



KIST is one of the must-see destinations included on the itineraries of leaders of developing countries when they visit Korea. A frequently asked question by many leaders of developing countries is, “Why was Vietnam chosen as a recipient country to establish the KIST model?” To answer this question, Dr. Moon emphasized that the

success of a research institute lies in its operation, not establishment. In other words, it would be meaningless to have a research institute when there are no industries or a foundation to implement the outcomes of research.

The commitment of political leaders and an industrial foundation are vital for the successful operation of a research institute. Leaders of Vietnam are strongly committed to science and technology and the country has a fairly strong industrial foundation on which to leverage R&D outcomes.

Dr. Moon went on to say that the characteristics of the Vietnamese people, who generally have hard-working and achievement-oriented spirits, as well as the cultural closeness between Korea and Vietnam, will hopefully make V-KIST a successful case model.

Vietnam has been enjoying steady growth in trade in recent years. In Southeast Asia, Vietnam is the second largest export market right behind Singapore, and trade volume has soared by more than 40 times over the last 21 years. Such conditions are expected to enhance the synergistic effect between Korea and Vietnam as the KIST model of S&T research is implemented. According to Dr. Moon,

From a Korean perspective, this ODA is a one-way transfer from Korea to Vietnam; however, with KIST's participation in management, many opportunities for joint research, personnel exchange, etc., will arise which, of course, represent additional benefits for Korea.

In fact, the exchange of manpower and joint research is already happening. Through the International R&D Academy (IRDA), KIST provides support to talented Vietnamese students in pursuing their research careers at KIST. As Dr. Moon points out,

There are around 100 outstanding foreign students in the program at KIST, out of which Vietnamese students make up a large proportion. So far, 40 foreign students have graduated from KIST, many of whom are still actively engaged in research activities as deans, professors and researchers.

Dr. Moon also stated that he looked forward to working together with foreign graduates of KIST in opening V-KIST and furthering mutual exchange.

Extending support based on successful ODA cases

KIST plans to inject US\$35 million over the next four years in the V-KIST project with the support of the Korea International Cooperation Agency (KOICA). There are plans to build three research buildings, including a main building, residential building and annex facility. KIST will also provide major research equipment to carry out preliminary research and develop programs to enhance human resource capacity through short- to long-term training, master's and PhD programs. Advisory services to build and operate V-KIST will also be provided by KIST.

Renowned scientists who witnessed the early development of KIST and external experts will serve as management advisors. Dr. Moon emphasized that the founding members of KIST will pass down their experiences in establishing a successful research institute and the external experts will set the direction of Vietnam's future in science and technology.

When KIST was founded, outstanding Korean scientists working overseas were the first professionals to be recruited and were an immediate source of highly-qualified engineering manpower. Dr. Moon hopes that V-KIST will be able to lure talented Vietnamese scientists now working overseas to return home and contribute to the economic growth of their home country.

KIST hopes that with the successful establishment and operation of V-KIST, the KIST model can be standardized and applied in other developing countries. As expressed by Dr. Moon,

The very act of passing down a successful model and opening a new institute requires a lot of work. I expect a new strain of ODA projects relating to science and technology will spread once we help build V-KIST successfully. KIST will play the central role in delivering this success.

As a member of the National Science & Technology Advisory Committee, Dr. Moon has met with President Park Geun-hye a number of times. President Park has encouraged him to continue his work on V-KIST. Just as KIST evolved from the firm commitment of the late president, Park Chung-Hee, and went on to drive Korea's growth, it is hoped that V-KIST, supported by the late president Park's daughter, the current president, Park Geun-hye, will drive Vietnam's economic growth and development.





Cover image :

Research on indoor farming-based medicinal plant cultivation and effect of various environmental factors.

- Indoor farming-based large-scale production and standardization of medicinal plant materials.
- Improvement of bioactive compounds in plant materials through the optimization of environmental factors during the cultivation period.
- Analysis of genotype (G), environment (E), and genotype X environment (GXE) effects for plant phenome research.
- Screening of valuable plant resources through high-throughput plant phenotyping.

Editorial Information

Editor-in-Chief
Tae Hoon Lim

Editorial Board Members
Hae-Young Koh
Hyun Kwang Seok
Il Ki Han
Joonyeon Chang
Youngsoon Um
Seok Won Hong
Jongjoo Kim
Seung Yun

Managing Editor
Sang-A Chang
sarachang@kist.re.kr
Editorial Office Telephone
+82-2-958-6039
Web Address
www.kist.re.kr/en

English Advisory Services
Anne Charlton
The Final Word Editing
Services
the_final_word@live.com

KIST Korea Institute of
Science and Technology

Hwarangno 14-gil 5, Seongbuk-gu, Seoul 136-791,
Republic of Korea
Tel +82-2-958-6039 www.kist.re.kr/en
E-mail sarachang@kist.re.kr



Using a Platform of Multiple Technologies to Build a New Future

